SCUOLA DI DOTTORATO
UNIVERSITÀ DEGLI STUDI DI MILANO-BICOCCA

Department of Physics

PhD program in Physics and Astronomy Cycle XXXVI

Curriculum in Applied Physics and Electronics

Heterostructured Scintillators: a Novel Approach to Achieve High Sensitivity and Fast Timing in TOF-PET

Surname: Pagano Name: Fiammetta

Registration number: 802677

Tutor: Prof. Marco Paganoni

Co-Tutor : Dr. Etiennette Auffray

Supervisor: Prof. Marco Pizzichemi

Coordinator: Prof. Stefano Ragazzi

ACADEMIC YEAR 2022/2023

Abstract

This Ph.D. thesis presents a comprehensive investigation of heterostructured scintillators, a novel detector technology for Time-of-Flight Positron Emission Tomography (TOF-PET) aimed at overcoming the trade-off between sensitivity and timing performance. They consist of two materials with complementary properties (i.e., high stopping power for 511 keV γ-rays and fast timing) assembled together in a stack of alternating layers and exploit the energy sharing mechanism: the γ-ray is most likely absorbed in the heavy material but the recoil photoelectron can escape from it and deposit its remaining energy in the fast material, improving the timing of the detector.

First, the fundamental properties and limitations of heterostructured scintillators are investigated using BGO&EJ232-based heterostructures. Monte Carlo simulations were performed to optimize the thicknesses of BGO and plastic layers so as to maximize the probability of energy sharing while keeping high stopping power. A method for events classification (energy deposition only in BGO, only in EJ232, or in both materials) based on pulse shape discrimination was developed and it served as the basis for all the experimental studies that followed. The development and experimental validation of analytic models describing scintillation kinetics, coincidence time resolution (CTR), and depth-of-interaction (DOI) contributions are provided. With the state-of-the-art photodetection technology (SiPM NUV-HD and NUV-MT by Broadcom) and electronics readout (high-frequency circuits), a CTR below 200 ps was achieved for $3\times3\times20\,\mathrm{mm}^3$ BGO&EJ232 heterostructures.

Next, the focus moves to the next generation of heterostructures, that aims to use nanocrystal scintillators instead of standard plastic scintillators because potentially faster and denser. An experimental setup to simultaneously measure the light output and time resolution of these materials under pulsed low energy (0-40 keV) X-ray excitation was developed and successfully applied to the study of lead halide perovskite ($CsPbBr_3$) nanocrystals. The combination of GAGG and $CsPbBr_3$ resulted promising both under X-ray and 511 keV excitation, with a ten- and twofold improvement, respectively, compared to bulk GAGG.

Overall, this thesis proved the high potential of heterostructure scintillators as a means to improve the timing performance while keeping reasonable sensitivity of detectors for TOF-PET.

Riassunto

Questa tesi di dottorato introduce una nuova tecnologia di rivelatori come potenziale soluzione al compromesso tra potere di frenamento e risoluzione temporale nella tomografia ad emissione di positroni (*positron emission tomography*, PET) con tempo di volo (*time-of-flight*, TOF): le eterostrutture di scintillatori (*heterostructured scintillators*). Questi scintillatori sono costituiti da due materiali con caratteristiche complementari (elevato potere di frenamento per raggi γ con energia 511 keV e cinetica di scintillazione veloce) che vengono combinati in maniera alternata così da sfruttare il meccanismo di condivisione dell'energia (*energy sharing*): il raggio γ viene assorbito dal materiale pesante, ma il fotoelettrone risultante può sfuggire da esso e depositare nel materiale veloce la sua energia residua, migliorando la risposta temporale del rivelatore.

Inizialmente, vengono esaminate le proprietà fondamentali e i limiti delle eterostrutture utilizzando come materiali il BGO e lo scintillatore plastico EJ232. Attraverso simulazioni Monte Carlo, si è ottimizzato lo spessore degli strati di BGO e plastica al fine di massimizzare la probabilità di condivisione dell'energia, mantenendo contemporaneamente un'alta efficienza di rivelazione. È stato sviluppato un metodo per la classificazione degli eventi (deposizione di energia solo in BGO, solo in EJ232, o in entrambi) basato sulla forma dell'impulso, che è servito da base per tutti gli studi sperimentali presentati in seguito. Inoltre, è stato sviluppato e sperimentalmente validato un modello analitico per descrivere la cinematica di scintillazione nelle eterostrutture. Ciò ha permesso di confermare l'applicabilità alle eterostrutture di modelli analitici, già consolidati per materiali monolitici, che descrivono la risoluzione di coincidenza temporale (*coincidence time resolution*, CTR) e il contributo dovuto alla diversa profondità di interazione (*depth of interaction*, DOI) del raggio gamma. Grazie all'utilizzo di tecnologia all'avanguardia di fotorivelazione (SiPM NUV-HD e NUV-MT sviluppati da Broadcom) e di elaborazione del segnale (circuiti elettronici ad alta frequenza), è stata raggiunta una CTR inferiore a 200 ps per eterostrutture con BGO ed EJ232 di dimensioni $3\times3\times20\,\mathrm{mm}^3$.

Successivamente, l'attenzione si sposta verso la prossima generazione di eterostrutture, che mira a sostituire scintillatori plastici convenzionali con scintillatori a nanocristalli, potenzialmente più veloci e con maggiore densità. È stato sviluppato un apparato sperimentale per misurare contemporaneamente la quantità di luce e la risoluzione temporale utilizzando come sorgende di eccitazione raggi-X pulsati a basse energie (0-40 keV) ed è stato applicato con successo allo studio dei nanocristalli di perovskite di alogenuro di piombo ($CsPbBr_3$). La combinazione di GAGG e $CsPbBr_3$ si è rivelata promettente sia sotto eccitazione a raggi X che a 511 keV, con un miglioramento rispettivamente di un fattore dieci e due, rispetto al GAGG monolitico.

Nel complesso, questa tesi ha dimostrato l'alto potenziale delle eterostrutture come mezzo per migliorare le prestazioni temporali mantenendo una sensibilità ragionevole dei rivelatori per la TOF-PET.

Contents

List of Figures

List of Tables

Part I

Introduction

Introduction

Context of the Research Project

Positron emission tomography (PET) is the most sensitive functional medical imaging technique, providing the picture of an organism's metabolic activity by measuring the activity of a radiotracer. Its most widespread application is in the field of oncology and neurodegenerative diseases but, because of its accuracy at the picomolar level, it is also increasingly used in cardiology, psychiatry, metabolic diseases, and *in-vivo* studies.

The physical principle on which PET relies is the β^+ decay of a radioactive biomarker and the following positron-electron annihilation into two back-to-back γ-rays with 511 keV energy each. The two photons are detected in coincidence outlining a line of response (LOR) along which the annihilation took place. As the number of counts is proportional to the amount of radiotracer, the collection of many LORs and their processing via reconstruction algorithms allows to get an image of the radiotracer distribution.

Compared with other imaging techniques, such as computed tomography (CT) and magnetic resonance imaging (MRI), the main disadvantages of PET are the lower spatial resolution of the final image and the higher dose delivered to the patient. Both aspects can be improved by including the information on the time-of-flight (TOF) difference of the two γ-rays in the reconstruction process, with several side benefits.

Without any information about the difference in the arrival times of the two photons, any point along the LOR has the same probability of being the origin of the event. By including the TOF information in the reconstruction process, each pixel along the LOR is weighted by the probability of being the origin of the annihilation point, resulting in a reduction of the noise propagation in the image. The reduction is related to the width of the kernel used, being inversely proportional to the square root of the CTR [1].

The TOF-PET research community is now addressing their efforts to reduce the coincidence time resolution (CTR) below 100 ps at system level, with the final aim to achieve 10 ps [2]. A CTR of 10 ps would lead to an increased effective PET sensitivity, as compared to the state-of-the-art, of at least a factor 16 and the best desirable spatial resolution along the LOR (1.5 mm, then limited by the range of the positron), paving the way to reconstruction-less TOF-PET.

The state-of-the-art total body TOF-PET scanner is the Siemens Biograph Vision.X, with a CTR of 178 ps [3]. Therefore, going down to 10 ps requires to face several technical challenges and the optimization of the whole detection chain. Within this field, numerous research avenues are actively explored, focusing on

various aspects: the search for the most suitable material [4, 5], the optimization of the photodetector [6–8], and of the readout electronics [9–12]. As the CTR is largely limited by the scintillation mechanism, recent works focusing on the material stage aim to exploit prompt photon emission processes: e.g. Cherenkov photons [13–16], cross-luminescence [17–19], hot-intraband luminescence [20, 21], and quantum confinement properties of nanocrystals [22–25]. However, each of them comes with its own set of disadvantages, often related to low photon yield or low stopping power for 511 keV γ-ray.

In response to these challenges, a novel approach has been proposed: a combination of two materials with complementary properties into a single scintillating detector known as a heterostructure [26, 27]. The principle behind heterostructures is the energy sharing mechanism: when combining a high-Z scintillator with a fast but low-density material, the incoming γ-ray is most likely absorbed in the heavy material, but for a fraction of events, that we will refer to as *shared events*, the recoil photoelectron can deposit its energy in both materials. The more energy is deposited in the fast material, the more fast photons are produced, improving the overall time resolution of the detector.

Objective and Structure of the Thesis

This thesis focuses on the understanding and optimization of heterostructured scintillators for TOF-PET. The core of the thesis is divided into three main parts:

- Part II introduces the imaging technique of PET and TOF-PET. First, a general overview of the principles of PET, the history and current status of this technique is provided, and the advantages of TOF measurements are explained. The main building blocks of a PET measurement are analyzed in detail to understand the main contributions to time resolution. Finally, the concept of heterostructures is proposed as a solution to overcome current barriers to the best achievable temporal resolution.

- Part III presents a comprehensive investigation of heterostructured scintillators consisting of alternating layers of BGO and plastic scintillators. This configuration allows for a solid understanding of the properties of this technology as uses two well known materials. The experimental validations of analytic model describing the scintillation kinetics and the CTR of heterostructures are provided. The improved timing performance of heterostructures compared to bulk BGO is evaluated and further studied through double-sided readout.

- Part IV focuses on the first steps toward the development of a new generation of heterostructured scintillators, in which plastic will be replaced by an even faster and heavier material, so as to effectively become a competitive alternative to the current state of the art. The most promising candidates for this role are nanocrystal scintillators, which by benefiting from quantum confinement effects can exhibit a sub-nanosecond decay time and high intrinsic light yield.

Finally, Part V draws the conclusions and discusses the next steps.

Part II

Heterostructured Scintillators for TOF-PET

Chapter 1

Introduction to PET and TOF-PET

1.1 Introduction

Positron emission tomography (PET) is a functional imaging technique capable of providing metabolic images of the patient. With its ability to detect concentrations down to the picomolar level, PET is the imaging technique offering the highest molecular sensitivity and quantitative accuracy. It enables, for example, the early diagnosis, staging and follow-up of cancer and the diagnosis of certain neurodegenerative diseases, such as Alzheimer. Other fields of application are cardiology, psychiatry, and *in-vivo* studies of small animals.

The main disadvantages of PET are the higher dose delivered to the patient and the worse spatial resolution compared to other medical imaging techniques, such as computed tomography (CT) and magnetic resonance imaging (MRI).

In this chapter, the basic principles of PET are initially outlined in Section 1.2. Section 1.3 then illustrates the significant historical events and developments that have contributed to the current state of PET technology. Section 1.4 introduces the Time-of-Flight (TOF) technique as a potential means of enhancing spatial resolution and PET image quality, and discusses the benefits derived from this technique. Finally, Section 1.5 outlines the essential requirements of a TOF-PET scanner.

1.2 Principles of PET

The physical principle on which PET relies is the β^+-decay and the following positron-electron annihilation events. By substituting an atom of a biotracer with a β^+ isotope, the resulting radiotracer is injected into the patient and it spreads physiologically within the body so that the radioisotope activity distribution is proportional to the drug concentration (i.e., the metabolic activity). By detecting in coincidence the two back-to-back γ-rays resulting from the positron-electron annihilation, it is possible to reconstruct the position of the annihilation event itself, obtaining a map of the radioisotope activity distribution, hence of the body metabolic activity.

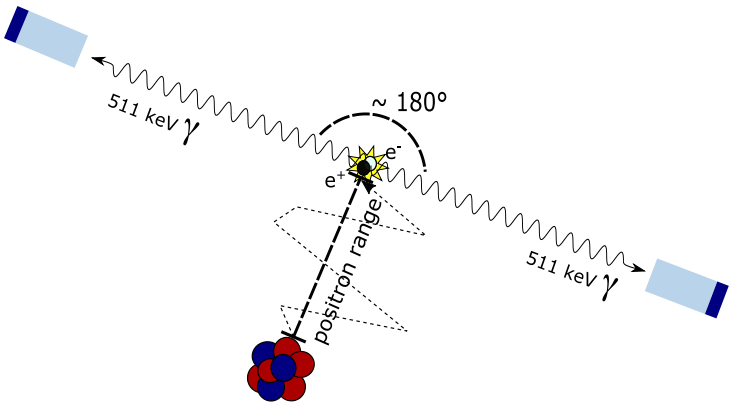

Figure 1.1: Principle of PET. Positron emission via β^+-decay, its annihilation with an electron of the tissue into two 511 keV γ-rays that are detcted in coincidence.

1.2.1 The Physics of PET: β^+ Decay

The β^+-decay is a type of radioactive decay in which a proton within an atomic nucleus is converted into a neutron by the simultaneous emission of a positron with a neutrino:

$$p \rightarrow n + e^+ + \nu_e. \tag{1.1}$$

Being this a 3-body decay process, the positron can be emitted with any energy up to the maximum available in the decay, resulting in a typical continuous emission spectrum. It loses this energy through multiple Coulomb interactions with orbital electron of the tissue atoms. Once it reaches thermal equilibrium with the tissue, it forms an unstable bound state with an electron, the positronium, which annihilates into two quasi-anticollinear 511 keV γ-rays. The two back-to-back γ photons are detected in coincidence, outlining a line of response (LOR) along which the annihilation occurs. This mechanism is illustrated in Figure 1.1.

In order to reconstruct the position of the annihilation event, many LORs need to be acquired and processed with reconstruction algorithms, as briefly introduced in Section 1.2.3. While several sources of uncertainty on the reconstructed annihilation position in PET are related to the reconstruction algorithms or limitation of the whole system, there are two constraints intrinsic to the physics process that set a limit in the best achievable spatial resolution:

- The positron range, i.e. the path traveled by the positron before the annihilation occurs. The point of emission and annihilation therefore do not correspond exactly, generating an error in the reconstruction of the spatial distribution of activity. The range depends on the energy of the positron, the atomic number Z, and the density of the medium. The range of positrons resulting from the isotopes used in PET in water (similar in composition to human tissues) is about 1-2 mm (see Table 1.1).

- The *quasi* anti-collinearity of the two annihilation photons. If both the electron and positron were at rest, due to the conservation of energy and momentum, the annihilation would generate two anti-collinear 511 keV

γ-ray. However, neither is properly at rest. The positron has a kinetic energy determined by the thermal energy that may be negligible, but the energy with which the electron is bound to the atom is not, and this causes the two annihilation photons to lose their collinearity.

1.2.2 Radio-tracers

The substitution of an atom of a biotracer with its respective β^+ isotope is possible because it does not significantly affect the biological and chemical behavior of the molecule [28].

The β^+-emitters most commonly used in PET are ^{11}C, ^{13}N, ^{15}O and ^{18}F. They are called *physiological radioisotopes* because the corresponding stable isotopes are the main constituents of human tissues. Their most relevant physics properties for PET application are listed in Table 1.1. All these isotopes have a short half-life, which has the advantage of delivering to the patient just the dose needed for the PET examination. The disadvantage, especially for very short-lived radioisotopes such as ^{15}O, is related to the time needed to transport the radioisotope from the production site (the cyclotron) to the hospital, as hospitals rarely have cyclotrons on site. To minimize the waste of the radioisotopes produced, the delivery time from production to the patient should be of the order of the half-life of the radioisotope. The one of ^{18}F ($\sim$ 110 min) is a good compromise. Moreover, ^{18}F can replace both its stable isotope ^{19}F and the hydroxyl group OH^-, the most common free radical in biological systems. Finally, the positron resulting from the decay of ^{18}F has low average kinetic energy therefore small average range. All these factors make ^{18}F a suitable radioisotope for PET. Indeed, the most commonly used radiotracer is fluorodeoxyglucose (^{18}F-FDG), a glucose analog that, when injected into the patient, diffuses into regions of high metabolic activity.

Table 1.1: Most commonly used physiological radioisotope and their physical properties. Adapted from [29].

Radioisotope	Half-life [min]	Positron average kinetic energy [keV]	Positron average range in water [mm]
^{11}C	20.4	385	1.2
^{13}N	10.0	491	1.6
^{15}O	2.0	735	2.8
^{18}F	109.8	242	0.6

1.2.3 Image Reconstruction

When a pair of detectors records an annihilation event, given their finite size, it does not outline a line but a volume of response (VOR) containing all the possible LORs connecting that pair of detectors. The key principle of PET imaging is that the total number of coincidence events detected by the two detector elements is proportional to the total amount of radiotracer contained in the VOR:

$$N_{ij} = k \int_{VOR_{ij}} \rho(x, y, z) dv. \tag{1.2}$$

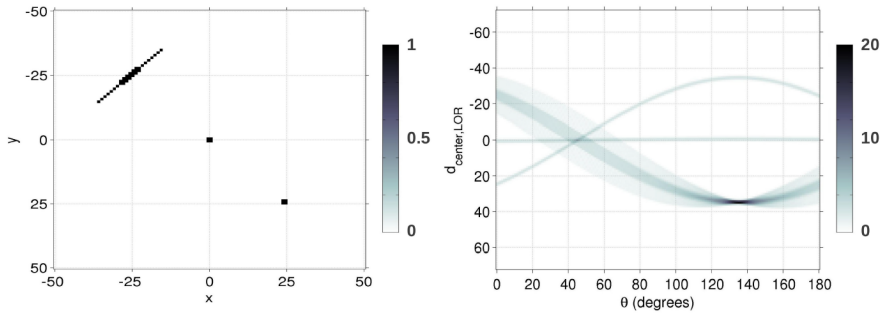

Figure 1.2: Illustration of Radon Transformation, taken from [31]. Left: point distribution in the coordinates space. Right: sinogram of the corresponding Radon Transform.

$\rho(x, y, z)$ is the spatial distribution of the radiotracer and is the quantity to be obtained from a PET measurement. The mathematical formulation of the problem is described by the inverse of Radon Transform [30], at the basis of the reconstruction algorithms.

The Radon transform data are also called *sinogram* as the Radon transform of a point in the center of the coordinate system is a straight line but any off-center point source is transformed into a sinusoid. Consequently, the Radon transform of a series of points results in a set of blurred sine waves with different amplitudes and phases. An example of the Radon transform is shown in Figure 1.2.

There are mainly two types of algorithms to transform the sinogram back to the original image in the coordinate space: analytic and iterative algorithms.

Analytic Algorithm

The most widely used analytic algorithm in PET is the *Filtered Back Projection* (FBP). The back projection is the inverse of the Radon transform. The latter is the operation that maps a $f(x, y)$ distribution in the space of Cartesian coordinates into the space of polar coordinates $p(s, phi)$. Since the data resulting from a PET measurement are the polar coordinates of the LOR, one needs to apply the inverse transformation to obtain the original activity distribution. However, it can be demonstrated that the simple back projection returns the $f(x, y)$ distribution convolved by a term that explode in the center $(1/\sqrt{x^2 + y^2})$ and introduces a blurring to the original image. The correct solution is obtained by applying the so-called *ramp filter* to the sinogram before doing the back projection, hence the name of filtered back projection.

Iterative Algorithm

Recently, iterative image reconstruction methods have become quite popular in PET imaging reconstruction as they are better suited if the recorded data are noisy [32].

The most used iterative algorithm in PET reconstruction is the *Maximum likelihood Expectation Maximization* (ML-EM) [33]. It starts with an assumed tracer distribution image in the body, whose expected projection is computed according to equation 1.2. The calculated sinogram is compared with the measured

one, and the differences will be the input for an updated tracer distribution function. This procedure is iterated until a predefined criterion or a fixed number of iterations is reached.

1.3 Brief History of PET

The history of PET goes through several discoveries that have often been awarded Nobel Prizes [29]. First of all, the discovery of the positron by American physicist Carl D. Anderson in 1932. This discovery not only provides the experimental confirmation of the prediction of antimatter made by Dirac, earning Anderson the Nobel Prize in Physics in 1936, but, together with the fundamental theory of the radioactive β decay, constitutes the theoretical basis of PET [34]. The invention of the cyclotron, for which Ernest Lawrence in 1939 received the Nobel Prize in Physics, was fundamental for the production of the proper radioisotopes to be used in medical applications, the already mentioned physiological radioisotope [35]. The next step was the understanding of the principle of radiotracers. György Hevesy received in 1943 the Nobel Prize in Chemistry for proving that changing an atom in a molecule with its radioisotope does not significantly affect its chemical and biological behavior [28]. Because of this principle, the diffusion and concentration of a molecule within a living organism can be measured by loading the molecule with a radioisotope and detecting the product of its decay.

In addition to these fundamental discoveries that made possible the application of β decay and positron annihilation for medical purposes, the development of a proper detection system was essential to bring PET measurements from the laboratory to the clinical level. In this regard, the invention of the first Photomultiplier Tube (PMT) by Leonid A. Kubetsky in 1934 [36] and the discovery of the scintillation properties of thallium-doped sodium iodide (NaI:Tl) by Hofstadter in 1948 [37] were essential.

The very first prototype of a PET scanner was built in 1952 by Gordon L. Brownell and William Sweet using two opposite NaI:Tl crystals coupled to two PMTs as detectors [38]. In the 1970s, the first tomographs comprising up to 48 NaI:Tl crystals were realized [39–41] adopting for the first time the ring geometry, the most widespread also nowadays as it allows for 360-degree coverage.

A few years later NaI:Tl was substituted by Bismuth Germanate (BGO), more favorable for PET because of its higher stopping power. BGO became the preferred choice for PET for the following 20 years, until the discovery of Lutetium Oxyorthosilicate (LSO:Ce) [42] which has slightly lower stopping power than BGO but much greater photon yield and faster decay time (40 photons/keV and 40ns instead of 10 photons/keV and 300ns). The use of LSO:Ce provided increased spatial, energy, and time resolution with a reduction of scatter and random coincidence contribution, and paving the way to time-of-flight (TOF) PET.

The main limitation of PMTs was their size, which was a physically constraining factor and an expensive means of crystal-photodetector one-to-one coupling, necessary for good spatial resolution. This limitation was initially overcome with the introduction of the block detector concept by Casey and Nutt in 1986 [43]. This concept relies on a module consisting of NxN PMTs coupled to an array of MxM crystals with M>N, in which the crystal where the interaction occurs is identified via light sharing method between the PMTs.

Moreover, in the same years, a new class of more compact photodetectors, based on Silicon diodes, was emerging. Avalanche photodiodes (APD) allowed for one-to-one coupling at the millimeter scale, offering unprecedented granularity and improved spatial resolution. In 1994, the first PET scanner using APD was built at the University of Sherbrooke by the team of Roger Lecomte. Other advantages of the APDs over the PMTs were the lower supply voltage needed and the insensitivity to magnetic fields. Since then, further development on the photodetection technologies led to Silicon Photomultiplier (SiPM), offering, compared to APD, higher photodetection efficiency, gain, and timing performances.

Nowadays, most of commercial scanners consist of modules (either in block detector or one-to-one coupling configuration) of L(Y)SO:Ce crystals read out by SiPMs as they provide the best timing and spatial resolution performance. The state-of-the-art commercial TOF PET scanner is the Biograph Vision by Siemens, with 214 ps TOF resolution [44]. A new upgraded system, Biograph Vision.X, has been released this year and presented at the Society of Nuclear Medicine and Molecular Imaging (SNMMI) 2023 annual meeting in Chicago, which is reported to feature a TOF resolution of 178 ps [3].

1.3.1 Why PET at CERN?

In the 1980s, the first idea of the Large Hadron Collider (LHC) project was launched and in the 1990s the outline of the project became clear: a particle accelerator consisting of a 27-kilometre ring of superconducting magnets with a number of accelerating structures and a huge system of detectors with the-state-of-the-art technology for four experiments to work in parallel.

In 1990, the Crystal Clear Collaboration (CCC) [45] was established with the purpose to develop scintillating materials suitable for being use at the LHC collider. To achieve this goal, a interdisciplinary network was set up, involving world experts in different aspects of material science (crystallography, solid state physics, luminescence, defects in solids) and in instrumentation for the detection of high energy photons and electrons. Following the studies carried on by the several groups of the CCC, the CMS collaboration chose to use lead tungstate (PWO) as inorganic scintillators for the electromagnetic calorimeter [46, 47]. In the same years, the results about the first PET scanner consisting of inorganic scintillators read out by APD were published. This configuration triggered interest in the high-energy physics (HEP) community. First, PMTs could not be used in the CMS experiment because of the 4 T magnetic field. Moreover, PWO is characterized by relatively low light yield and APD and then SiPM, allowing much higher gain at lower biased voltage compared to PMT, could provide better performances.

Since then, the CCC carried out the R&D on scintillators and photodetectors in parallel both for HEP and PET applications, as the main requirements to meet were the same for both applications: high stopping power, high light yield, good energy resolution, and fast decay time.

Some medical imaging devices that were developed inside the collaboration, based on LuAP, LuYAP, LSO, and LYSO crystal, are: ClearPET [48], ClearPEM [49], ClearPEM-Sonic [50], EndoTOFPET, and EndoTOFPET-US [51].

Presently, the CCC is directing its efforts toward exploring new techniques and materials that can potentially overcome the current limitations in timing,

light yield, and energy resolution associated with conventional method. This thesis work is performed within this framework.

1.4 Time-of-Flight in PET

TOF PET includes in the reconstruction process the information about the difference in the time of arrival of the two γ-rays. The direct effects are a spatial resolution along the LOR and an improvement in the signal-to-noise ratio (SNR) of the final image.

1.4.1 Role of Time Resolution in PET

Since the speed of γ-rays is known, from the measurement of the time of flight of the annihilation photons, it is possible to retrieve the position of the event along the LOR. Specifically, the spatial resolution (Δx) along the LOR is proportional to the coincidence time resolution (CTR) [29]

$$\Delta x = \frac{c}{2} CTR. \tag{1.3}$$

Therefore, given the correlation between time and spatial information, one can aim to recover the annihilation point simply by measuring the TOF and to get rid of the reconstruction process. However, to obtain a spatial resolution comparable to the one currently achieved with reconstruction, i.e. down to 3.5 mm [44], a CTR of 20 ps is needed (Equation 1.3). This represents a tenfold improvement compared to the current state-of-the-art TOF PET scanner [3, 44] and requires addressing several technological challenges as all elements of the detection chain need to be simultaneously improved. This aspect will be discussed in the next Chapter 3.

On this trail, a challenge has been launched to achieve 10 ps CTR [2]. The reason for the choice of this value is that it would allow for a spatial resolution of 1.5 mm, which corresponds to the range of positron in water, the inherent limitation to the best spatial resolution achievable in PET, as discussed in Section 1.2.

It should be mentioned that there are other limitations for reconstruction-less PET. The most important one is the need to correct for the attenuation of γ-rays from the human body to obtain an accurate measure of the dose. This is typically achieved through a computed tomography (CT) scan, which offers a twofold advantage. In addition to measuring the attenuation coefficients of the tissues of interest, since CT offers morphological images with much better spatial resolution than PET, it can be used to assist in the interpretation of PET scans.

However, a time resolution of 10 ps would bring a number of advantages to TOF-PET, even if the reconstruction process continued to be necessary. The principle of tomographic reconstruction in PET is known for being ill-posed, meaning that small errors in the input data cause large errors in the final image [52]. However, by including the TOF information in the image reconstruction process, its conditioning can be significantly improved. This is achieved by using a probability function, called TOF kernel, to weigh the likely positions of the annihilation site along the LOR, as shown in Figure 1.3. This

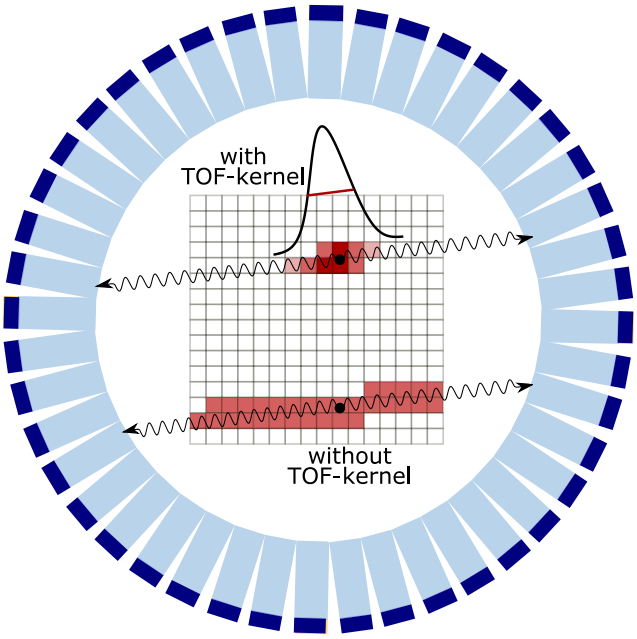

Figure 1.3: Time-of-flight concept. In standard PET, all pixels along the LOR have the same probability of matching the annihilation point. When a TOF kernel is included in the reconstruction process, each pixel is weighted by the probability of being the annihilation point.

kernel is typically considered to be a Gaussian centered on the annihilation position with the standard deviation given by the CTR of the system. When imaging an object of diameter D in a discretized region with $n = D/d$ image elements (pixels), where d is the dimension of each pixel, the SNR of the image is inversely proportional to the square root of the number n of pixels [53, 54], i.e. $SNR \propto 1/\sqrt{n}$. Because of the relation between time and spatial resolution (see Equation 1.3), when using a TOF kernel with a CTR giving a spatial resolution Δx, only $n = \Delta x/d$ pixel will contribute to the reconstruction process. The SNR gain obtained when using TOF compared to non-TOF is then given by

$$\frac{SNR_{TOF}}{SNR_{no-TOF}} = \sqrt{\frac{D}{\Delta x}} = \sqrt{\frac{2D}{c \cdot CTR}}. \tag{1.4}$$

1.4.2 Benefits from TOF-PET

As a consequence of the improved SNR in the reconstructed image according to Equation 1.4, PET imaging significantly benefit from a performing CTR.

The first and immediate effect is an improved image quality. Moreover, the SNR is proportional to the square root of the noise equivalent counts (NEC) [55]

$$SNR \propto \sqrt{NEC}. \tag{1.5}$$

Therefore, considering also Equation1.4, it can be concluded that with TOF it is possible to get a better SNR for the same number of counts, or equivalently, the

same SNR as without TOF but with fewer counts. This allows to use smaller amount of radiotracer, hence to deliver lower doses to the patient, and also to reduce the acquisition time.

This increased effective sensitivity, which with a CTR of 10 ps would increase at least of a factor 16 compared to state-of-the-art, has a number of positive effects:

- The radiation doses of molecular imaging procedures could be reduced to negligibly low levels, with the possibility to apply PET imaging also in the paediatric, neonatal, and prenatal contexts.
- Reducing the acquisition time can lead to more examinations in the same time, thus also reducing costs for the patient.
- The reduction of the synthesized quantity of radiopharmaceutical needed for each examination would lead to a further lowering of the costs associated to PET imaging.
- The possibility to further extend PET imaging beyond oncology and towards cardiovascular, neurological, metabolic, inflammatory, infectious or metabolic disease (such as diabetes).

1.5 TOF-PET scanner

1.5.1 Description of a TOF-PET scanner

Most of the modern PET scanners feature a ring-shape geometry, i.e. a cylindrical detector placed around the patient bed, as this design offer a 360-degree coverage. The detector consists of several modules, each of them consisting of a number of scintillating crystals coupled to photodetectors, arranged in adjacent and concentric rings. Total body PET scanners usually have an inner diameter of 65-85 cm and an axial length up to 200 cm [56], while the single crystals size is usually between 3-5 mm in section and 15-25 mm in length.

Each module is readout in coincidence with several modules belonging to the opposite arc of the detector. When considering only the coincidences between detectors within the same ring, the result will be a set of 2D images. However, by extending the analysis to coincidences between modules belonging to adjacent rings, a 3D image can be generated, thus also capturing depth information.

The acquisition system selects the recorded data based on energy and time information. Whenever a pulse coming from a crystal has an amplitude (or any other characteristic chosen for the energy measurement) compatible with a signal coming from the photoelectric absorption of a 511 keV γ-ray, the coincidence chain waits for a second signal meeting the same requirement for a certain time (coincidence window). If such an event occurs, the signals from the two modules are acquired, otherwise the event is discarded.

The recorded data are then fed to a reconstruction algorithm (Section 1.2.3) producing the final image of the measured dose.

1.5.2 Requirements for a TOF-PET scanner

The performance of a PET scanner are defined by four fundamental parameters: spatial, energy resolution, time resolution and sensitivity.

Spatial resolution

Earlier in this chapter the limits to the spatial resolution inherent to the physics process of β^+-decay were discussed (Section 1.2.1). However, there are also other aspects related to the detection process and the technology used, which limit the best achievable resolution:

- The cross-section of the crystal means that the triggering of a coincidence does not outline a line but a response volume (VOR).
- The thickness of the crystals, which without any information about the Depth-of-Interaction (DOI) generates a parallax error.
- The misidentification of the detector where the annihilation takes place, which may be due to multiple crystal interactions or other coding errors.

In the center of the FOV and using FBP as reconstruction algorithm, the spatial resolution can be modeled, in terms of full-width-half-maximum (FWHM), as:

$$FWHM = 1,25\sqrt{(d/2)^2 + b^2 + p^2 + (0,0022D)^2 + r^2}, \tag{1.6}$$

where d is the size of the detector, b^2 and p^2 are factor accounting for the coding and parallax error respectively, r is the positron range and $(0,0022D)^2$ (with D diameter of the scanner) is the estimate uncertainty due to not perfect collinearity of the two annihilation γ-rays [57] [29].

The spatial resolution is further deteriorated by scattering events and random coincidences, which contribute to misidentification of the LOR, as depicted in Figure 1.4. Random coincidences refer to those events which are accidentally detected within the same coincidence window but that are actually unrelated. Instead, scattered coincidences come from the same annihilation events but at least one of the 511 keV γ-rays has been scattered within the patient.

Typical spatial resolution values of modern commercial PET scanners are in the order of 3-6 mm.

Energy resolution

The energy resolution of a detector is its ability to discriminate particles with different energies. It is usually quoted as the ratio between the FWHM and the peak position of the distribution of signals produced by a monoenergetic source (e.g., the photoelectric peak at 511 keV of a ^{22}Na source).

In PET applications a good energy resolution is essential to discriminate the 511 keV photons from the background but also for discarding the scattered annihilation γ-rays (which have lost some of their energy in the scattering) that deteriorates the spatial resolution.

Time resolution

The other fundamental property of a detector, in order to correctly identify the annihilation γ-rays pair, is the coincidence time resolution (CTR). The main factors contributing to the time resolution will be discussed in detail in the next chapter, Section 2.5.

The role of CTR in TOF-PET as means to improve the SNR of the final image and the countless benefits resulting from this were illustrated in Section 1.4.

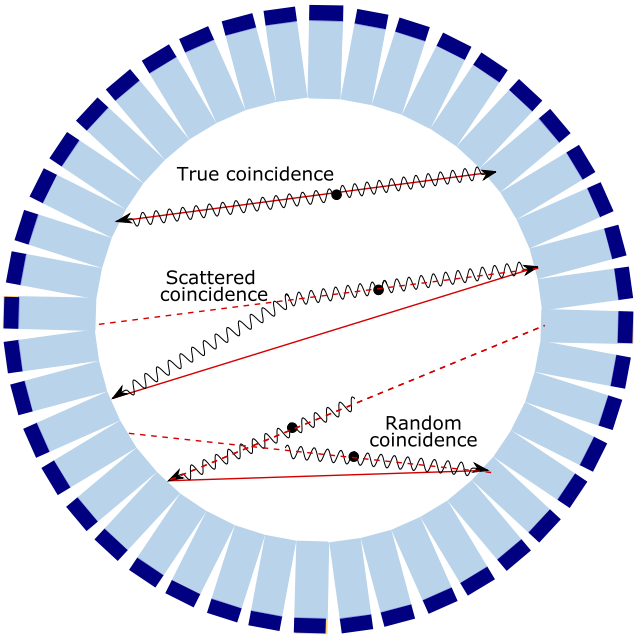

Figure 1.4: Diagram of true, scattered, and random coincidences. The solid lines represents the recorded LOR while the dashed line the "true" ones.

However, also in standard PET the time resolution of the detector has always played an important role as it allows to reduce the random coincidences.

Sensitivity

The sensitivity or detection efficiency (E) of a PET scanner is given by the ratio between the counting rate and the source activity. Several elements go to define the efficiency of a PET scanner, primarily: the intrinsic detection efficiency (ϵ), the geometrical efficiency (g), the electronic recording efficiency (f), and the absorption or scattering of the γ-ray in the screened object (F) [29]. They can be factored as:

$$E = \epsilon \times g \times f \times F. \tag{1.7}$$

The optimisation of these parameters is essential to reduce the injected dose to the patient, but is controversial as the dependence of spatial resolution on some of these parameters goes in the opposite direction. Indeed, the geometric efficiency g, which is related to the coverage of the solid angle of the PET ring, can be increased by reducing the diameter or increasing the axial extension of the PET scan. However, the parallax effect worsens as the radius of the scanner is reduced and axial extension can lead to an increase in the recorded scattered events. The intrinsic ϵ efficiency can be improved by increasing the crystal thickness, at the expenses of time and spatial resolution. Moreover, increasing the crystal length or the axial extension of the scanner lead to a significant increase in scanner costs.

Chapter 2

Physical Processes in PET Detection

2.1 Introduction

The first step of a PET measurement is the detection of the two back-to-back γ-rays. As photons are uncharged particles, their detection is done by detecting the secondary particles resulting from their interaction with the material they cross. Typically, a scintillator serves as the absorbing medium. It converts the incoming γ-ray into recoil electrons, which, through excitation and ionization processes, generate scintillating photons. These scintillating photons are subsequently detected by a photodetector, which converts them into an electric signal.

Section 2.2 illustrate the γ-ray interactions relevant in PET – photoelectric absorption and Compton scattering. In Section 2.3, the process of scintillation is explained distinguishing between organic and inorganic scintillators, pointing out the respective advantages and disadvantages for TOF-PET. The photodetection process, with a specific focus on SiPM, is discussed in Section 2.4. Finally, Section 2.5 discuss how all these processes contribute to the overall CTR of the detector.

2.2 Gamma-ray Interaction with Matter

Gamma-rays interact with matter mainly through Compton scattering, Photoelectric absorption and pair production. The cross section of each of these processes is function of the photon energy and of the atomic number Z of the absorber medium, as shown in Fig. 2.1. Pair production is a threshold process which cannot occur when the photon energy is less than 1022 keV (twice the electron mass). Since the photons resulting from the annihilation of positron have an energy of 511 keV, the only two interaction mechanisms which play an important role in PET are the Compton scattering and the photoelectric absorption.

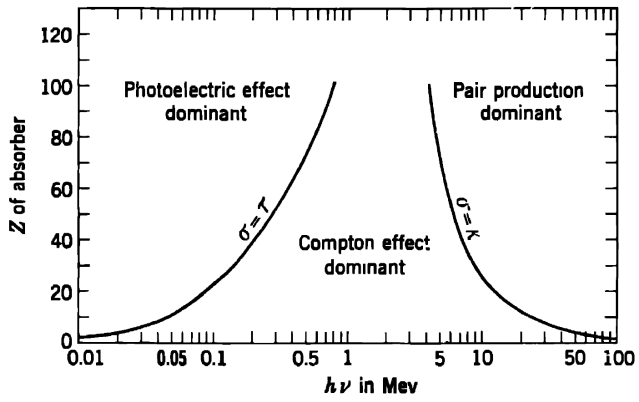

Figure 2.1: Relative importance of the main three types of photon interaction with matter in function of the atomic number (Z) of the absorber medium and of the photon energy ($h\nu$). The lines represent the $h\nu$ and Z values for which the two neighboring effects are just equal Figure taken from [58].

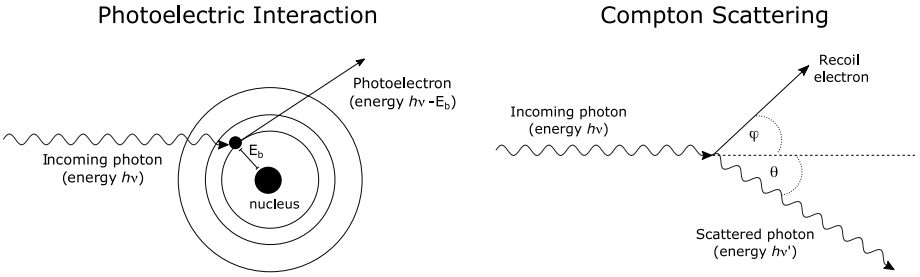

Figure 2.2: Schematic illustration of Photoelectric interaction (left) and Compton Scattering (right).

2.2.1 Photoelectric Absorption

In the photoelectric absorption, the incoming photon interacts with an atom of the absorber medium transferring its whole energy to an atomic electron. As a result, the photon disappears and the electron (called *recoil photoelectron*) is ejected from the atom by one of its bound shells with an energy given by

$$E_{e^-} = h\nu - E_b \tag{2.1}$$

where $h\nu$ is the incoming photon energy and E_b is the binding energy of the photoelectron in its original shell. This process is illustrate on the left side of Figure 2.2.

If the gamma-rays has sufficient energy, photoelectric absorption is likely to occur with the most tightly bound K-shell electron. Consequently, the interaction creates a ionized atom of the absorber medium, with a vacancy in one of its shells. This vacancy is quickly filled through the capture of a free electron from the medium and/or the rearrangement of electrons of the other shells, resulting in the emission of characteristic X-photons. These low energy X-ray photons are in general reabsorbed close to the primary photoelectric event. If the size of the

scintillator is small, such photons may escape the detector and cause an escape peak in the response. A competing process to the emission of characteristic X-rays is the emission of Auger electrons, carrying away the atomic excitation energy. However, at the Z values typical for scintillators used in PET (hence for high Z) it is less likely than characteristic X-rays emission.

Photoelectric interaction is predominant for low gamma energies and an enhancement in the cross section can be observed in materials with high atomic number Z materials (see Figure 2.1). A rough estimation of the Photoelectric cross section is given by

$$\tau \propto \frac{Z^n}{E_\gamma^{3,5}}, \tag{2.2}$$

where n varies between 4 and 5 depending on the photon energy.

2.2.2 Compton Scattering

Compton scattering is the inelastic scattering between a gamma-ray and a weakly bound or free electron in the material. The incoming gamma-ray transfers only part of its energy to the electron and it is deflected through an angle θ with respect to the original direction (see Figure 2.2, right). The equation relating the energy transfer and the scattering angle can be derived by the energy and momentum conservation laws. Assuming the recoil electron initially at rest, it results to be

$$h\nu' = \frac{h\nu}{1 + \frac{h\nu}{m_0c^2}(1 - cos\theta)}, \tag{2.3}$$

where $h\nu$ is the energy of the incoming photon, $h\nu'$ that of the scattered photon and m_0c^2 the rest-mass energy of the electron (511 keV). The greater is the scattering angle the greater is the energy transfer. However, some of the original energy is always retained by the incident photon, even in the extreme case of $\theta = \pi$.

The cross section of Compton scattering scales linearly with Z, as its probability per absorber atom depends on the number of available electrons as scattering centers. The differential cross section of Compton scattering is given by the Klein-Nishina formula:

$$\frac{d\sigma}{d\Omega} = Zr_0^2 \left(\frac{1}{1 + \alpha(1 - cos\theta)} \right)^2 \left(\frac{1 + cos^2\theta}{2} \right) \left(1 + \frac{\alpha^2(1 - cos\theta)^2}{(1 + cos^2\theta)[1 + \alpha(1 - cos\theta)]} \right), \tag{2.4}$$

where $\alpha \equiv h\nu/m_0c^2$ and r_0 is the classical electron radius. From Figure 2.1, it can be seen that Compton scattering is the most likely interaction process for gamma-rays in the energy range 0.1-1 MeV, hence in the energy domain of PET, unless for atomic number larger than 60.

2.3 Scintillation

Scintillation is the physical process where a material, called scintillator, emits ultraviolet (UV) or visible (VIS) light, following the excitation from ionizing radiation. One can generally distinguish between organic and inorganic scintillators.

2.3.1 Scintillators Requirements for PET

The first requirement for a good candidate scintillators for PET is high detection efficiency for 511 keV γ-rays. The detection efficiency is the ability of a material to stop the incoming radiation, and it is described by the γ-ray attenuation length coefficient (λ). When a photon beam of intensity I_0 cross a target of thickness L, the transmitted intensity is given by the exponential law:

$$I = I_0 \cdot e^{-L/\lambda}. \tag{2.5}$$

The attenuation length is a function of the density of the atomic number of the absorber material. Specifically,

$$\lambda = \frac{\rho}{\mu}, \tag{2.6}$$

where ρ is the density of the material and μ the linear attenuation coefficient μ, i.e. the total probability of interaction of the incoming γ-rays. For PET, where the two relevant processes are Photoelectric absorption and Compton scattering,

$$\mu = \tau(Photoelectric) + \sigma(Compton), \tag{2.7}$$

with $\tau \propto Z^{4-5}$ and $\sigma \propto Z$ (see Equation 2.2, 2.4). High linear attenuation coefficient (μ), thus low attenuation length (λ), means higher gamma absorption capability.

In PET it is also important to discriminate between Compton and Photoelectric events, as Compton scattering occurring in the patient can lead to an erroneous identification of the LOR. For this purpose, good energy resolution is required. The energy resolution of a scintillator depends in first instance on the light yield and on the homogeneity of the light yield as a function of the interaction position. In an ideal crystal, the energy resolution would be given by statistical fluctuations in the number of photons (according to Poisson statistics). However, crystals always have some impurities that introduce a systematic variation in the number of photons produced depending on the interaction position. This effect usually overrides the nominal light output of the scintillator in determining its energy resolution. Moreover, other factors affect the light output (i.e., the number of detected photons) and by consequence the energy resolution. The scintillator needs to be transparent to its own emission and of good optical quality to guarantee a good light transport from the emission point to the photodetector. The refractive index should match the one of the photodetector for a good light transfer efficiency (LTE).

2.3.2 Organic Scintillators

Organic scintillators are divided into plastic, liquid, and crystalline. Plastic scintillators are the most common due to their low cost and easy manufacturing. They consist of a polymer matrix, usually polystyrene (PS) or ponyvinyltoluene (PVT), in which organic dyes are embedded.

The scintillation mechanism in organic scintillators is based on the fluorescence process. When an organic molecule absorbs energy, it rises to an excited state and returns to its fundamental state through the emission of visible light. This process has a typical time scale of a few nanoseconds. There are a number of processes competing with fluorescence that affect the scintillation efficiency of

organic scintillators. These include phosphorescence, which is also a radiative process but with longer decay times (up to a few minutes) as it is associated with forbidden transition in quantum mechanics, and non-radiative processes such as internal conversion and quenching.

An additional effect affecting the light output is the small Stoke Shift. The Stoke Shift is the difference between the excitation and emission energy, which is usually small in organic molecules, leading to a non-negligible probability of self-absorption.

2.3.3 Inorganic Scintillators

Inorganic scintillators are generally semiconductor or insulator crystals, and in such materials, the energy diagram is described in terms of conduction, valence, and core bands. The energy difference between the valence and conduction band is called energy bandgap and it constitutes a forbidden band i.e., electrons cannot occupy those state in a pure crystal. Scintillation in inorganic materials can be either intrinsic or extrinsic. Examples of intrinsic inorganic scintillators are BGO and PWO. Extrinsic scintillators, on the other hand, involve luminescent centres that are not intrinsic to the crystal lattice, but are introduced through the addition of specific impurities, known as activators. This intentional doping of impurities leads to the creation of special allowed sites within the band structure of the material, with enhanced scintillation properties. This is the case for most inorganic scintillators, such as LSO:Ce, LSO:Ce:Ca, GAGG:Ce, GAGG:Ce:Mg, NaI:Tl.

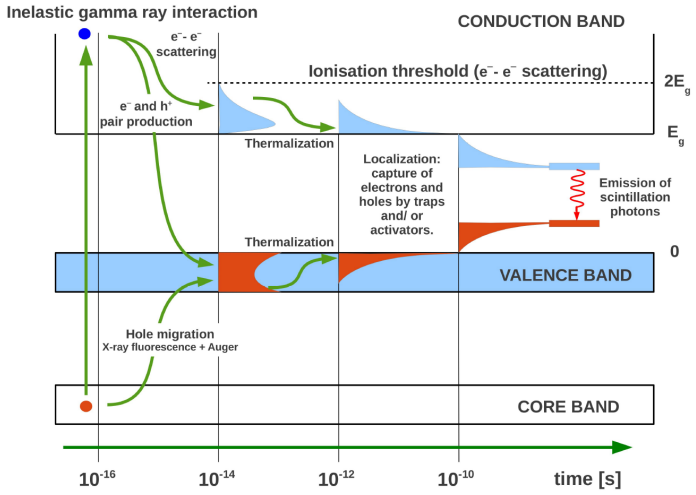

Figure 2.3: Diagram of scintillation mechanism in inorganic scintillators. The four different stages – multiplication, thermalization, transfer to luminescence centers, and recombination – are highlighted. Figure from [31].

After a γ-ray interacts in a scintillating inorganic crystal and releases its energy to an electron of the medium, a hot electron-hole pair is created and it initiates the scintillation. The scintillation mechanism in inorganic crystals can be described distinguishing four stages (see Figure 2.3), each of them characterized

by a different time constant.

- Multiplication. The hot electron-hole pair is subjected to electron-electron scattering and Auger processes in the material. In this way, further electron-hole pairs are created through inelastic scattering, until the energy of each electron and hole falls below the ionisation threshold, i.e. twice the bandgap. This process usually takes between 0.1 and 10 fs.

- Thermalization. Once the energy of the charge carriers is below the ionization threshold, their thermalization via phonon scattering starts. This process is in the order the picosecond.

- Transfer to luminescence centers. The thermalized charge carriers form excitonic states (Coulomb-bound state between hole and electron) and are transferred to the luminescence centers. The filling of luminescence centers takes between 1-100 ps.

- Recombination. Finally, the relaxation of the luminescence centers and recombination of the electron-hole pairs with the corresponding light emission can start. This process is characterized by time constants distributed in a wide time range, up to hundreds of nanoseconds, depending on the levels involved in the transition.

The sum of the time needed for the thermalization of the charge carriers and filling of the luminescence centers defines the rise time of the scintillation pulse, and it is usually below 100 ps. The time needed for the recombination defines instead the decay time of the scintillation pulse, usually between 20 and 600 ns.

2.3.4 Nanoscintillators

Nanoscintillators are scintillating materials with at least one dimension smaller than 100 nm [59]. At this scale, materials can exhibit unique scintillation properties that differ from their bulk counterpart. This effect is due to quantum confinement, a physical phenomenon that occurs when the motion of the particles responsible for scintillation is spatially confined [60–62]. In inorganic crystals, whose scintillation is exciton based, this happens when any of the crystal dimensions is comparable to or smaller than exciton Bohr radius, i.e. the distance between the electron and the hole in such bound state which, depending on the material, is between 2 and 50 nm. Quantum confinement results into more frequent exciton decays, i.e. faster decay time and higher light yield.

According to the number of confined dimensions, nanocrystals are classified into quantum dots (3D confined), quantum wells (2D confined), and quantum wires (1D confined).

The optical properties of nanocrystals depend strongly on their size and geometry. As the nanocrystal size decreases, the bandgap increases and the band structure turns into discrete, molecule-like energy levels which become prominent near the band edges. This strong correlation between the size and bandgap of nanocrystals enables the tuning of their emission spectrum [63].

Semiconductor nanocrystals are usually prepared in the form of a colloidal solution and subsequently incorporated into a host matrix, in a so-called nanocomposite. This process can both prevent their deterioration (as most nanocrystals

are sensitive to environmental conditions) and make them more suitable for a wider range of applications. The main drawbacks of nanocrystals are their lack of volume to efficiently stop the incoming ionizing radiation together with their small Stokes shift. This means that in layers thick enough to provide good stopping power, most of the light produced would be lost due to self-absorption.

A careful choice of the host matrix is therefore mandatory to fully exploit the properties of nanocrystals in radiation detectors. The biggest challenge is to fabricate a nanocomposite with high filling factor of nanocrystals while keeping its transparency. If the filling factor is too low, so will be the stopping power of the nanocomposite. However, as the filling factor increases so does the probability of self absorption making the composite opaque [64].

2.3.5 Prompt Photon Emission Processes

Besides the mechanism described above, the interaction of ionizing radiation with a medium can result in the production of UV-VIS photons also through other processes. The most relevant for timing application are those leading to the emission of prompt photons, i.e. with instantaneous rise and decay time. A common drawback of these processes is the low light yield.

Hot Intraband luminescence (IBL) and Cross-Luminescence (CL)

Hot electrons and holes produced by ionizing radiation have several ways to recombine. The scintillation mechanism described above, based on the recombination of hot electrons in the conduction band with hot holes in the valence band, is the most efficient in terms of light production. However, the charge carriers can also recombine differently.

When there is a high density of sub-levels at the bottom of the conduction band and/or the top of the valence band, it is possible that hot electrons and holes radiatively recombine during the thermalization process with holes and electron belonging to the same band. The luminescence resulting from this process is called *hot intraband luminescence* (IBL) and is characterised by extremely fast decay times, of the order of picoseconds [20, 65].

Another possibility is that the electron-hole recombination occurs between an electron of the valence band with a hole in the core band. This process is referred to as *cross-luminescence* (CL), and it only occurs in crystals having an energy gap between the valence and the core band smaller than the one between the conduction and valence band. If this condition is satisfied, the recombination probability between electrons and holes of the valence and core band, respectively, is large. As such, cross-luminescence is an intrinsically fast scintillation characterized by a decay time of the order of nanoseconds or less [66]. An example of cross-luminescent crystal is BaF_2, for which a decay time constant of 0.6 ns has been measured [66]. The associated light yield is of 1400 ph/MeV, which his high compared to other cross-luminescent materials but low for PET purposes. Another complication in exploiting CL is the emission in deep UV. The CL of BaF_2 is peaked at 195 nm, where the PDE of photodetectors is generally low. Therefore, new photodetection technologies are being investigated to increase the detection efficiency in the vacuum UV (VUV) region [17, 18].

Cherenkov

The Cherenkov effect occurs when a charged particle travels into a transparent material with a speed exceeding the one of light in that material. The reason is that charged particles traveling into a dielectric medium temporarily polarise the atoms close to its trajectory and, if their speed is faster than the phase velocity in the medium ($v > c/n$, with n the refractive index of the material), the electron polarization becomes asymmetric, resulting in a persistent dipole field. This field leads to the emission of coherent radiation at a specific angle, given by the equation $cos(\theta_c) = (n\beta) - 1$, where $\beta = v/c$ [67].

Cherenkov is therefore a threshold process and the higher the refractive index of a material, the higher the Cherenkov yield. The Cherenkov yield for typical PET scintillators (e.g., LSO and BGO) at PET energies (recoil electron resulting from photoelectric of 511 keV γ-ray) is of only a few tens of photons [68].

2.4 Photodetection

The photodetection is the process converting the optical photons produced by the scintillating material in into an electrical signal preserving the original energy and timing information. The photon detection is based on generating free electrons or electron-hole pairs in a medium. Two main technologies of photodetector devices can be distinguished: the vacuum photodetectors and the solid state photodetectors. The most commonly used ones for PET are the Photomultiplier Tubes (PMTs) and the Silicon Photomultipliers (SiPMs), belonging to the former and latter class, respectively.

2.4.1 Photomultiplier Tube

Photomultiplier tubes are vacuum photodetector and their operating principle is illustrated in Figure 2.4. First, the photons produced by the scintillator enter the tube through a glass or quartz window. The inner surface of the window is covered with a photosensitive material (usually bialkali), so that a free electron is produced following the photoelectric absorption of the incoming photon. The probability for a photon to be converted into an electron is called Quantum Efficiency (QE). It depends on the photon's wavelength and it is usually around 25-30 % [70]. This part of the PMT is called photocatode, since it is at a negative potential with respect to the dynodes so the generated electron is accelerated toward them. The dynodes are electrodes in series, each of them held to a higher potential than the previous one acting as multiplication stages. In this way, each time an electron strokes a dynode, it emit 3-4 secondary electrons that are accelerated to the next dynodes. Usually in a PMT there are 8-12 dynodes, hence 8-12 acceleration steps, which means that each generated photoelectron produces around 10^6 secondary electrons. This number represents the typical amplification factor of a PMT.

The primary drawbacks of PMTs include their low quantum efficiency, susceptibility to electrical and magnetic fields, high power consumption, and the transit time spread due to the several multiplication stages that degrades pulse time resolution. Moreover, as previously mentioned, PMTs are quite bulky, making the crystal-photodetector one-to-one configuration unfeasible while keeping high granularity.

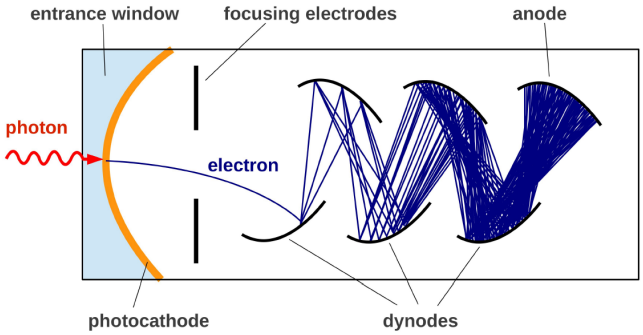

(a)

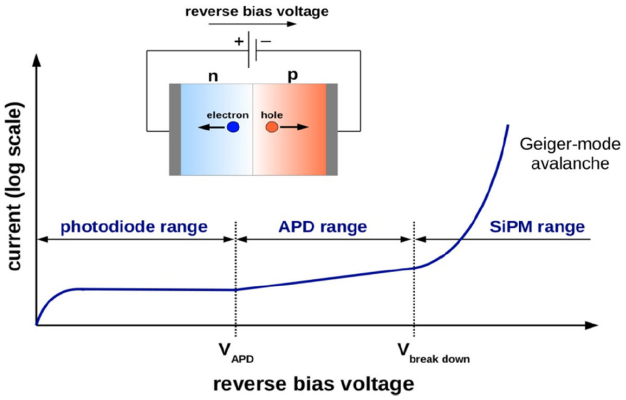

(b)

Figure 2.4: Schematic illustration of the working mechanism of (a) photomultiplier tubes [31] and of (b) avalanche photodiodes [69].

The advances reached in the 1990s in the semiconductor photodiode technology have paved the way for the substitution of PMTs with solid-state photodetectors in several applications, including PET.

2.4.2 Photodiodes and Silicon Photomultiplier

Photodiodes are semiconductor devices that generate an electrical current when exposed to light. When a photon with an energy greater or equal to the energy gap between the valence and conduction band strikes a photodiode, it creates an electrons-hole pair. By applying a reverse bias voltage, the charge carriers migrate toward opposite sides and generate a current.

The conversion of photons in electrons-hole pair has a QE up to 80-90 % [71], i.e. up a factor three better than in PMTs, as it does not require that charge carries escape from a surface. However, the first photodiodes lacked of an internal amplification stage because a low reverse bias voltage was used and the resulting current was smaller by several order of magnitude compared to PMTs (photodiode regime).

By increasing the reversed bias, the electrons gain enough kinetic energy in

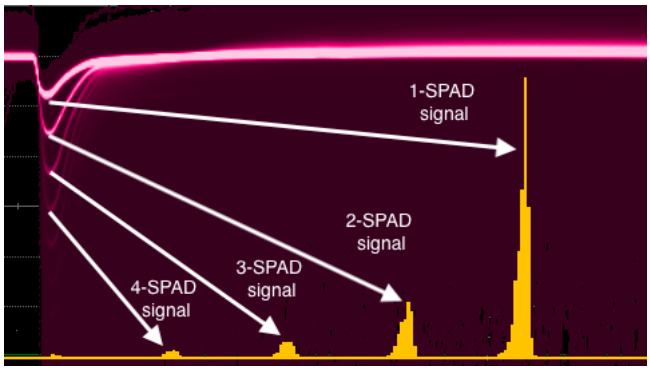

Figure 2.5: Dark count measurements of Broadcom NUV-MT SiPM biased at 48 V (over voltage of 16 V) showing the signals produced from 1,2,3,4 etc. triggered SPADs. The histogram in yellow represents the integrated charge of the corresponding signals.

the electric field to produce additional electron-hole pairs by inelastic scattering. Because of the higher mobility and ionization coefficient, only electrons participate to the avalanche process. The multiplication process is linear and the resulting current is proportional to the initial number of produced electron-hole pairs. These devices are called avalanche photodiodes (APD) and work in the so-called avalanche regime.

When the reverse bias voltage is further increased beyond a certain threshold, called breakdown voltage, the electric field is high enough that both electrons and holes contribute to the multiplication process generating a self sustained avalanche that need to be quenched externally. The multiplication is so high that even a single photoelectron can be detected, while in the photodiode and the avalanche regime the minimum detectable signal are of a few hundreds (200-300) and a few tens (10-20) photoelectrons, respectively [71]. This working regime is called Geiger-mode APD (G-APD) and imply the loss of proportionality between the primary and the multiplied charges. A single G-APD device cannot therefore be used in energy measurement.

To overcome this lack of proportionality, silicon photomultiplier (SiPM) integrates a dense array of independent single-photon avalanche diodes (SPADs), also called microcells, connected in parallel and each with its own quenching resistor. SiPMs have a SPADs density between 100 and several 1000 per mm^2, depending on the SPAD size, making unlikely that more than one photon strikes the same cell at the same time. The energy information is therefore carried on by the number of activated SPADs, which corresponds to the number of photons detected. Figure 2.5 shows the well distinct signals coming from 1,2,3 etc. triggered SPADs.

In the context of this thesis, mainly SiPMs were used as photodetectors, therefore an overview of their main properties and characteristics is reported [72].

- The breakdown voltage (V_{br}) is the voltage that must be applied to trigger the Geiger discharge. In a graph of current versus voltage, V_{br} is the voltage value at which the current begins to increase exponentially and no longer linearly with the voltage.

- The over voltage (OV) is the difference between the bias voltage at which

the SiPM is operated and the breakdown voltage:

$$V_{bias} = V_{br} + OV.$$

– The gain of a SiPM is defined as the amount of charge created for each detected photons, and it is a function of the overvoltage and of the SPAD size. Given the capacitance C of a microcell and the electron charge q, the gain (G) is given by:

$$G = \frac{OV \cdot C}{q}.$$

– The photodetection efficiency (PDE) is the statistical probability for an incident photon that interacts with a microcell to produce an avalanche. Therefore, it differs from the QE stated for PMT or APD due to the microcells structure. It is a function primarily of the wavelength of the incident photon and of the applied OV:

$$PDE(\lambda, OV) = \eta(\lambda) \cdot \epsilon(OV),$$

where $\eta(\lambda)$ is the quantum efficiency of Silicon and $\epsilon(OV)$ the avalanche initiation probability. The former is the probability for a photon of a given wavelength to create a electron-hole pair in Silicon. The latter takes into account that not all the charge carriers in the active volume will initiate an avalanche.

– The recovery time is the time needed for an activated SPAD to recharge to the full operating voltage. When a microcell in the SiPM is triggered and the Geiger avalanche is initiated, a photocurrent flowing through the microcell is generated causing a voltage drop across the quench resistor. Once the photocurrent is quenched, the voltage across the diode recharges to the full operating voltage.

– The fill factor refers to the percentage of the SiPM surface actually sensitive to the light. Each SPAD needs to be optically and electrically isolated from its neighbours, which results in a fraction of dead space around each microcell. Because the separation necessary between two microcells is fairly constant, regardless on the microcell size, SiPMs with larger microcells will have higher fill factor. High fill factor results in higher gain and PDE, but because of higher capacitance, also in longer recovery time and lower dynamic range.

– The single photon time resolution (SPTR) measures the accuracy of the SiPM in recording the arrival time of a detected photon.

– The dark count rate (DCR) refers to electrical pulses generated by the SiPM in the absence of any incident photons. It is primarily due to thermal electron generated in the active volume and it is the main source of noise in an SiPM. The DCR is a function of the active area, the OV, and temperature.

– The internal crosstalk is defined as the probability that a secondary photon produced by an avalanching microcell causes a secondary avalanche in a

neighboring SPAD. The process occurs instantaneously and as a consequence, single incident photons generate signals equivalent to two or more photons.

– The external crosstalk is defined as the probability that a secondary photon produced by an avalanching microcell can exit the surface of the SiPM but be reflected back to it. This probability become likely in systems, where the SiPM is coupled to a crystal which can act as a reflector.

– The afterpulsing is the generation of an electrical signal with a delay of up to several nanoseconds due to charge carries that during the avalanche become trapped in defects of Silicon and once released trigger a secondary avalanche.

2.5 Considerations on Contributions to Time Resolution

All the sequential steps involved in the conversion of a 511 keV γ-ray into an electron pulse described above contribute to the detector time resolution. However, what ultimately limits the time resolution of a detector is the stochastic nature of the light emission process.

The probability that a photon is emitted at a time t is given by [73]:

$$P_{scint}(t) = \frac{e^{-t/\tau_d} - e^{-t/\tau_r}}{\tau_d - \tau_r}\Theta(t) \tag{2.8}$$

where τ_d and τ_r are respectively the decay and rise time of the scintillator, while $\Theta(t)$ is the Heaviside function for a signal starting at the time $t = 0$. From order statistics consideration about the scintillation process [74–76], a first approximation of the coincidence time resolution is given by:

$$CTR \propto \sqrt{\frac{\tau_d \cdot \tau_r}{N_{ph}}}, \tag{2.9}$$

with N_{ph} the number of detected photons.

This approximation accounts only for the scintillation process, namely for the conversion of the γ-ray into optical photons. The other contributions that need to be considered are the γ-ray depth of interaction (DOI), the transport of the optical photons to the photodetector, the photodetection process and the electronic readout. A graphical representation of all the contributing factors to the CTR is given in Figure 2.6.

The γ-ray interacts within the crystal and is converted into a photoelectron at a certain distance from the entering face, called depth of interaction. The probability for an interaction occurring at a certain DOI is given by the exponential attenuation low. The propagation time of the optical photons depend on the DOI, therefore if this is unknown, the DOI uncertainty is reflected into time uncertainty.

Optical photons are emitted isotropically, except for Cherenkov photons whose directionality is described by the wave cone (see Section 2.3.5). The scintillator is usually wrapped in a reflective material to allow also photons emitted in a

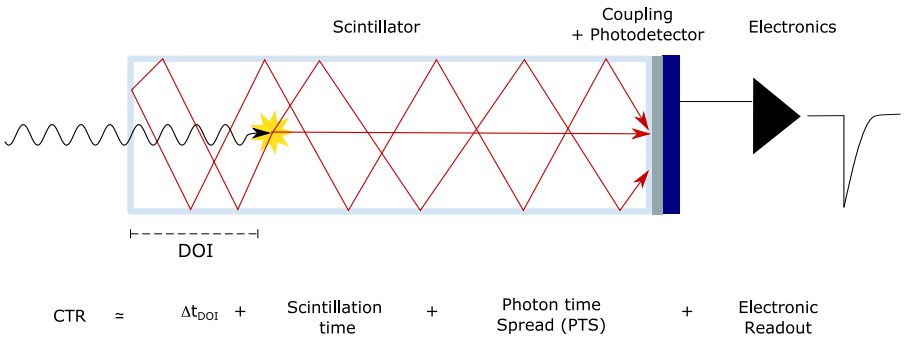

Figure 2.6: Schematic illustration of the contributions to the broadening of the CTR, thoroughly explained in the text.

different direction than that of photodetector to reach it and maximize the light collection. According to the original emission direction and the incident angle on the crystal surface, photons take different paths, hence different times, to reach the photodetector. This generates a photon transit time spread (PTS) which plays an important role in time resolution. The PTS depends on the DOI, the refractive index of the crystal, its geometry and surface treatment.

Optical photons need first to reach the exit face of the crystal without being absorbed and then to be extracted from it and converted by the photodetector in a current signal. The mismatch between the crystal and the coupling medium with the photodetector makes some photons bounce in the crystal several times before being extracting contributing to the PTS and other will be lost. The probability for an emitted photons to reach the photodetector is called light transfer efficiency (LTE).

The main parameters of the SiPM contributing to the time resolution are the SPTR and the PDE (Section 2.4). The latter further affects the number of detected photons. The parameter N_{ph} can therefore be factored as:

$$N_{ph} = N_{emitted} \cdot LTE \cdot PDE = LY \cdot E_{\gamma} \cdot LTE \cdot PDE, \tag{2.10}$$

where LY is the light yield of the material and E_{γ} the energy of the γ-ray (i.e., 511 keV), giving the total number of emitted photons $N_{emitted}$.

Finally, the electronic readout can also affect the time resolution, because electronic background noise can cause variation in the time trigger pulse, generating fluctuations.

Statistical considerations on all the processes described above led to the formulation [77] and experimental verification [5] of a full analytic expression for the CTR:

$$CTR_{analytic} = 3.33 \cdot \sqrt{\frac{\tau_d \cdot (1.57 \cdot \tau_r + 1.13 \cdot \sigma_{SPTR+PTS})}{PDE \cdot LTE \cdot LY_{@Energy}}}. \tag{2.11}$$

Equation 2.11 comprises all the factors explained before: the rise and decay time of the crystal, its LY at the incoming radiation energy, the LTE to the photodector and its PDE. The PTS of the crystal and the SPTR of the SiPM are enclosed in a single parameter, $\sigma_{SPTR+PTS}$, which represents the sigma of the

Gaussian convolution between PTS and SPTR. The factor 3.33 is because we are considering the coincidence time resolution between two detectors expressed in FWHM.

Chapter 3

Heterostructured Scintillators

3.1 Introduction

In the previous chapters, the concept of TOF-PET and the advantages of 10 ps TOF resolution were discussed: improvement in image quality and patient workflow, and reduction of delivered dose are among them.

This achievement proved to be quite challenging as it requires the improvement of all the components of the detection chain. Given the recent improvements in photodetectors and readout electronics, the major limitation is now represented by the stochastic process of light emission.

Current research is actively exploring strategies to exploit the prompt photon emission processes – such as Cherenkov photons [13–16], cross-luminescence [17–19], hot-intraband luminescence [20, 21] – to improve the overall time resolution of PET detectors. The common drawback of these light emission mechanisms is the low associated light yield, which affects both the time and energy resolution. In recent years, nanoscintillators have gained significant attention because of their potential high intrinsic light yield and ultra-fast scintillation kinetics due to quantum confinement. Here, the main disadvantages are the lack of volume to effectively stop incoming radiation and the small Stokes shift affecting light extraction.

One possible solution is to incorporate a material that guarantees fast emission and/or high light output in a detector that also includes another material that provides the missing properties, i.e. stopping power, in a so-called heterostructure.

In this chapter, the concept and fundamental principle of heterostructures is illustrated.

3.2 Concept of Heterostructures

Heterostructured scintillators involve the combination of two or more materials with distinct properties, used strategically to exploit the advantages of each component. In the specific context of TOF-PET, the two key properties that are not simultaneously found in a single material to the required extent are an efficient stopping power for gamma rays at 511 keV and a high photon density, i.e. the emission of a large number of photons in the first few nanoseconds.

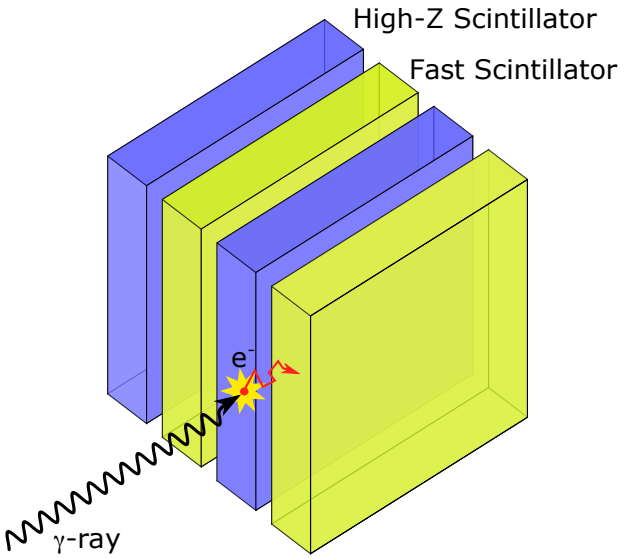

Figure 3.1: Concept of heterostructures and mechanism of energy sharing. The incoming γ-ray is most likely stopped in the heavy material, and the resulting recoil photoelectron can escape from it, travel into the fast emitting material where it will deposit the remaining energy producing fast photons. Figure published in [81].

The concept follows the one of sampling calorimeter in HEP, where two different materials are combined [78, 79]. Here, a heavy and non-scintillating material (e.g. Tungsten) is used with the only purpose to stop the incoming radiation and trigger the hadronic or electromagnetic shower. It is then combined with a scintillating material providing the desirable properties for energetic measurements.

The simplest way to combine different materials is by stacking alternating layers, as illustrated in Figure 3.1. Despite other configurations are also possible and are being investigated [80], this is the one elected for this research project and from here on we will refer to it for the discussion of heterostructures properties. However, the underlying principle of heterostructure is the same independently on the configuration used. It is called energy sharing [26, 27] as it refers to the fact that the energy of the incoming radiation is deposited in both materials. This phenomenon becomes relevant when the thickness of the heavy material is comparable to the range of the recoil electron resulting from the photoelectric absorption of a 511 keV γ-ray in the material itself (a few hundred micrometres). Thus, the incident γ-ray can be stopped by the photoelectric effect in the heavier material, but there is a non-negligible probability that the photoelectron will escape from it to the faster material, where it will deposit the remaining energy. The events for which energy sharing occurs are called *shared events*. The more energy is deposited in the fast material, the more fast photons are produced, improving the overall time resolution of the detector. The discussion regarding optimisation and the compromises to be made when choosing the thickness of the two materials is the specific subject of Section 4.2 but will return frequently in this thesis work.

3.3 Overview of Heterostructures to Date

The first proof-of-concept of heterostructure for TOF-PET was presented by Turtos et al. [27]. Here, the fast plastic scintillator BC422 [82] was successfully combined first with BGO and LYSO in small ($3\times3\times3\,mm^3$) pixels. This work shows the possibility to discriminate the events according to the material where the energy is deposited and gave the experimental proof that a CTR improvement compared to the bulk heavy material can be achieved with this approach.

Further works [81, 83–85] investigated the properties of heterostructures with BGO or LYSO and plastic scintillators. These studies deepened the understanding of heterostructure properties and also tested longer heterostructure pixels (15-20 mm), approaching the length used in commercial scanners.

Despite plastic scintillators like BC422 and EJ232 [86] features an effective decay time of 1-2 ns [5], considering their modest light yield and low density, they do not allow for exceeding the performance of the current state-of-the-art.

Other fast materials have already been tested, ranging from BaF_2 [87], to 2D perovskite [88], and nanomaterials [21, 89, 90].

In addition to the several studies conducted on individual heterostructured pixels in order to gain a complete understanding of this technology and test the best achievable performance, simulation works have been carried out to assess the effect of the heterostructure approach on the final reconstructed image [91]. The multi TOF-kernel approach [92, 93] in image reconstruction is highly attractive for heterostructure-based scintillators because of the different time response of the two materials.

On the road to heterostructure-based systems, an interesting configuration is the semi-monolithic approach. This approach aims to combine the advantages of semi-monolithic readouts, in which a crystal is read by several photodetectors that allow precise estimation of the interaction depth, with the supreme timing of heterostructure designs [94, 95].

3.4 Objective of this Research Project

Some of the aforementioned studies have been the subject of this research project [81, 85, 89, 96, 97]. The results presented in this dissertation are divided into two main topics. The first one focuses on heterostructures based on BGO and plastic scintillators, specifically EJ232, with the aim of deepening the fundamental principles and pushing the limits of this technology. The second part shifts to the investigation of the next generation of heterostructures, in which plastic scintillators will be replaced by higher-performance materials. The focus will be on nanoscintillators, in particular lead halide perovskites.

Part III

BGO&Plastic Heterostructured Scintillators

Overview

Heterostructured scintillators offer a possible solution to the trade-off between fast timing and sensitivity for TOF-PET detectors [26, 27]. They rely on the combination of two (or more) materials with complementary properties (i.e., high stopping power and fast timing) and on the mechanism of energy sharing. The annihilation $\gamma-$rays are most likely stopped in the heavy material, while the recoil photoelectron can deposit part of its energy also in the fast emitter boosting the time resolution of the detector.

In the next chapters, a thorough study on the fundamental properties of heterostructure is presented. For this purpose, a simplified proof of concept of heterostructured scintillators consisting of two well-known materials, BGO and EJ232 plastic scintillator [86], organised in stacks of alternating layers, is considered. Specifically, the next chapters are organized as follow:

- Chapter 4 investigates the mechanism of energy sharing through Monte Carlo simulation and outline a method to identify the events depositing energy in both materials in experimental measurements;
- Chapter 5 presents the experimental validation of an analytic model describing the scintillation kinetics of heterostructured scintillators;
- Chapter 6 shows the results in terms of coincidence time resolution (CTR) of heterostructures, comparing their performances with BGO crystals. It also provides an insight of the impact of light transport in heterostructures;
- Chapter 7 applies double-sided readout as technique to compensate the degradation of timing performances due to light transport and to retrieve the information on the γ-ray's depth of interaction (DOI).

The findings of these studies have already been published or are under consideration for publication [81, 85].

Chapter 4

Energy Sharing in Heterostructured Scintillators

4.1 Introduction

The fundamental principle of heterostructured scintillators is the energy-sharing mechanism from the recoil photoelectron. Namely, once the γ-photon interacts through photoelectric effect in the heavy material, the recoil electron must be able to escape from it and travel into the fast scintillator where to deposit the remaining energy. These events are called *shared photopeak events*. For this to work, the thickness of the heavy scintillator must be thin enough to maximize the probability for the recoil photoelectron to escape. At the same time, the thicker the fast scintillator, the greater the amount of energy deposited here and, by consequence, the higher the number of fast photons produced. However, a higher volume fraction of fast (and light) material also leads to low stopping power. A compromise therefore needs to be found.

The next step to fully exploit the potential of heterostructured scintillators is to identify and select the shared photopeak events, those that boost the overall timing performances.

The first part of this chapter, Section 4.2, presents a Monte Carlo simulation study that investigates the energy deposition as a function of the thickness of the two materials (BGO and plastic scintillator) and finds the best trade-off between fast timing and stopping power.

Section 4.3 illustrates how to experimentally retrieve the information about the material where the energy is deposited and perform the events classification. The method outlined in this section is the initial stage of all the studies presented in the next chapters.

4.2 Monte Carlo Simulations

4.2.1 Geometry, Input and Output Parameters

The simulation framework is based on GEANT4 toolkit [98] and reproduces a layered heterostructure made of alternated plates of BGO and plastic separated

by a thin layer (set to 1 μm) of air. The focus of this study is the energy deposition. Therefore, only the chemical composition, the atomic number, and the density of the two materials were taken into account.

A heterostructure of overall size $3\times3\times15\,\mathrm{mm}^3$ was simulated. The optimal thickness of BGO was determined as described in Section 4.2.2 and next the thickness of plates of plastic scintillator was varied from 10μm to 220 μm in steps of 10 μm.

A 511 keV γ-ray source was placed in front of the pixels, shooting in random direction toward the $3\times3\,\mathrm{mm}^2$ face, as shown in Figure 4.1. A sample of 500000 events was used for each configuration.

The information extracted to find the best compromise between stopping power and fast timing are: the number of events going through photoelectric interaction; the fraction of these events depositing energy in both materials; the amount energy deposited in plastic. The photoelectric (PE) probability is evaluated as the percentage of events depositing more than 400 keV (therefore including the photoelectric events with following X-ray escape) compared to the total of events interacting in the pixel:

$$PE = \frac{\text{Events depositing} > 400\,\text{keV}}{\text{Events depositing} > 0\,\text{keV}} \cdot 100 \quad [\%]. \tag{4.1}$$

The fraction of shared 511 keV was calculated as the fraction of photoelectric events depositing at least 50 keV (same threshold applied also in the analysis of the experimental data) in plastic:

$$Shared\,PE = \frac{\text{PE Events } En_{\text{plastic}} > 50\,\text{keV}}{\text{PE Events}} \cdot 100 \quad [\%]. \tag{4.2}$$

Finally, for each shared photopeak event, the amount of energy deposited in plastic was considered and the average over all the shared events (N_{shared}) was evaluated:

$$< En_{\text{plastic}} > = \frac{1}{N_{\text{shared}}} \sum_{i=0}^{N_{\text{shared}}} En_{\text{plastic,i}} \quad [\text{keV}]. \tag{4.3}$$

Bulk pixels of BGO and LYSO with same size were also simulated to evaluate the sensitivity loss, defined as:

$$Sensitivity\ loss = \frac{PE_{\text{bulk}} - PE_{\text{het}}}{PE_{\text{bulk}}} \cdot 100 \quad [\%]. \tag{4.4}$$

In this case only the photoelectric probability was evaluated, allowing to quantify the sensitivity loss of heterostructure in relation to pure BGO and to compare the sensitivity of heterostructure with LYSO, the standard scintillator for TOF-PET nowadays.

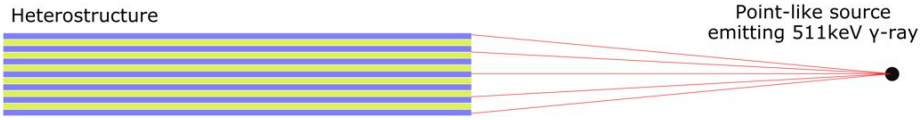

Figure 4.1: Sketch of the simulation setup. Figure published in [81].

4.2.2 Electron Projected Range in BGO

The thickness of BGO plates was established according to the mean range of an electron resulting from photoelectric absorption of 511 keV γ-ray. Electrons lose energy through excitation and ionization, and the figure of merit commonly use to evaluate their range before they are fully stopped is the continuous-slowing-down approximation (CSDA) range. However, because of the light mass of electrons and the high atomic number of BGO ($Z_{\text{eff}} = 73$), the CSDA range in this material is significantly different from the geometrical distance between the emission and absorption point (projected range). According to the NIST database [99], the CSDA range of an electron of 511 keV in BGO is $2.982 \cdot 10^{-1}\,\text{g/cm}^2$, i.e. about 420$\mu$m.

Monte Carlo simulations were performed to evaluate the projected range. For simplicity, a point source shooting electron of energy 511 keV was placed at the center of a bulk BGO crystal. For each event the geometrical distance between the emission and the absorption point was evaluated, resulting in an average value of 70μm. This result is compatible with a recent work performed on recoil electrons after photoelectric interaction of 511 keV γ-ray, which confirms this value being below 100 μm [100].

Taking into account the practical aspects of obtaining such thin crystal layers for the experimental work (both in terms of costs and actual feasibility), a thickness of 100 μm was chosen for BGO plates.

4.2.3 Optimization of plastic thickness

Once the thickness of BGO plates was decided, a scan over different thicknesses of plastic (from 10 μm to 220 μm in steps of 10 μm) was performed. The results of this scan are illustrated in Figure 4.2. The photoelectric probability (PE), percentage of shared events ($Shared\ PE$), and mean deposited energy in plastic ($<En_{\text{plastic}}>$) are represented as a function of the plastic thickness. The photoelectric probability of pure BGO and LYSO of the same dimensions are also shown. It should be reminded that the following results refer to a single detector.

The comparison with bulk BGO allows to quantify the sensitivity loss, which goes from 4 % to 37 % for the two extreme thicknesses considered (10 μm and 220 μm, corresponding to the conditions in which, out of the total volume, a fraction of 9 % and 67 % is made of plastic, respectively). By increasing the plastic thickness, the mean energy deposited in plastic increases from 70 keV to almost 200 keV, and the probability to have shared 511 keV events from 5 % to 65 %.

The photoelectric probability of LYSO was used as criterion to choose the optimal geometry for this kind of heterostructure. L(Y)SO is the state-of-the-art crystal detector for TOF-PET due to its relatively fast decay-time, good stopping power and energy resolution. However, its photoelectric probability is lower than BGO because of the lower effective atomic number. Indeed, Figure 4.2 shows that for a plastic thickness up to 70 μm, the photoelectric probability of the heterostructure is higher than LYSO.

Looking at the configuration with 100 μm thick plastic plates (and 100 μm thick BGO plates, so half volume plastic and half volume BGO), one can observe that the photoelectric probability of the heterostructure is similar to that of an equivalent bulk crystal of LYSO, almost half of the photoelectric events is shared

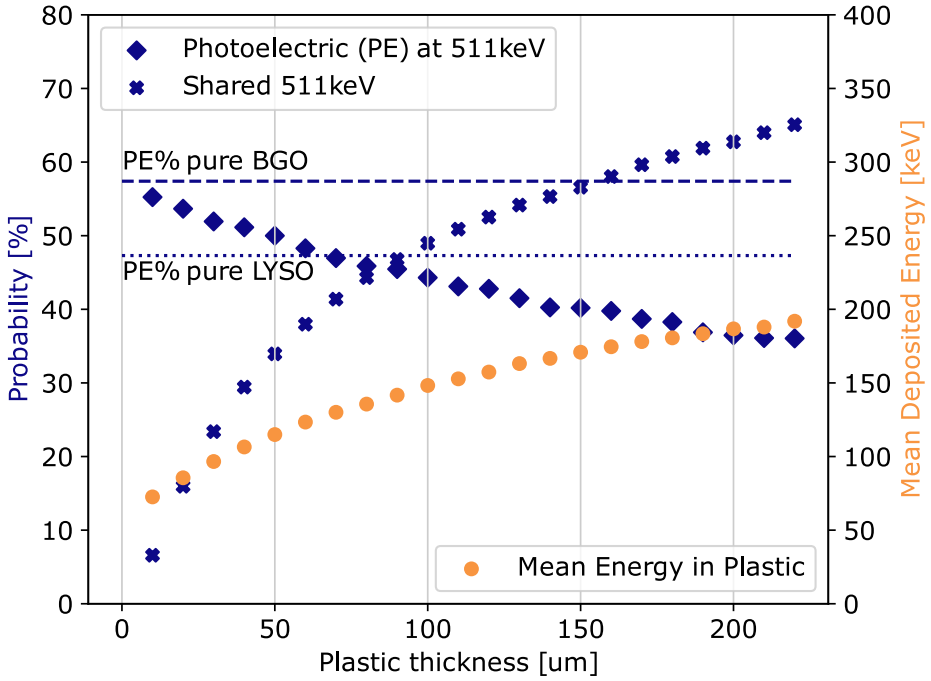

Figure 4.2: Results of Monte Carlo simulations with Geant4 toolkit about the energy deposition in a $3\times3\times15\,\mathrm{mm}^3$ heterostructure made of alternating layers of BGO ($100\,\mu$m thick) and plastic scintillator (variable thickness from $10\,\mu$m to $220\,\mu$m). The probability of photoelectric effect for 511 keV γ-ray (blue diamonds, left y-axis), the probability for having shared 511 keV events (blue crosses, left y-axis) and the mean deposited energy in plastic (yellow dots, right y-axis) are represented as a function of the thickness of plastic scintillator plates. The photoelectric probability for 511 keV of heterostructures is then compared to the one of a pure BGO and pure LYSO crystal of the same dimension (dashed and dotted horizontal blue lines, respectively). Figure published in [81].

and, on avarage for these events, one third of the total energy is deposited in plastic.

4.3 Events Classification

The first step for the evaluation of the timing performances of TOF-PET detectors is the selection of the photopeak events. With heterostructured scintillators, depending on the scintillation properties of the materials that are combined together, this selection may not be straightforward. Moreover, to fully exploit the potential of heterostructures, it is necessary to classify the events according to the material where the energy is deposited.

For the specific case of heterostructures with BGO and fast plastic scintillator as EJ232, the events classification can be performed via pulse shape discrimination [27, 81]. Because BGO and EJ232 have similar light yield – 8-10 ph/keV – but different decay kinetics (the effective decay time of BGO is almost a factor 100 slower than EJ232 [97]), the pulse shape changes depending on how the deposited energy is distributed between the two materials. Specifically, the amplitude and the integrated charge of the pulses proved to be two features allowing for clear

pulse shape discrimination [27, 81].

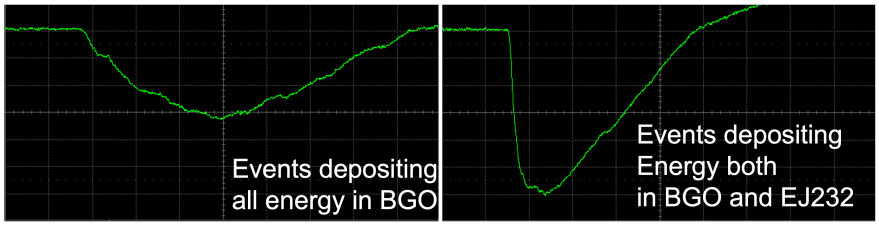

Figure 4.3: Example of heterostructures' pulse shape for different types of events.

The method for the events classification is presented referring to a $3\times3\times3\,\mathrm{mm}^3$ heterostructure with BGO plates $100\,\mu\mathrm{m}$ thick and EJ232 plates $200\,\mu\mathrm{m}$ thick, measured in dry coupling with a $6\times6\,\mathrm{mm}^2$ Hamamatsu (S13360-6050CS) SiPM. The double thickness of EJ232 compared to BGO was chosen to maximize the energy deposited in plastic and better illustrate the energy sharing. The signal was processed by a linear operational amplifier (AD8000) and digitized with Teledyne Lecroy HDO8108A oscilloscope. Figure 4.3 shows the snapshot of a slow pulse corresponding to an event depositing energy only in BGO (left) and of a much faster pulse, corresponding to an event depositing a significant fraction of the energy in EJ232 (right).

For each event, both the amplitude and the integrated charge need to be recorded. Their correlation is shown in the density scatter plot in Figure 4.4 (a). The pure events lie along a straight line because, while the integrated charge and amplitude depend on the amount of energy deposited, their ratio depends only on the scintillation kinetics and light output, therefore is fixed for a given material.

The present method for the events classification aims to provide for each event the amount of energy deposited in BGO and in EJ232, and it relies on a change of coordinates allowing to go from the (*Amplitude*, *Int.Charge*) to the (*EJ232 energy*, *BGO energy*) coordinates system.

First, the ratio between integrated charge and amplitude is evaluated for each event, allowing to compute the angle between the x-axis and each line passing through the origin and the point on the scatter plot corresponding to the considered event:

$$\theta = 180^\circ/\pi \cdot \arctan\left(\frac{Int.Charge}{Amplitude}\right). \tag{4.5}$$

θ_B and θ_P, the angles of BGO and plastic events respectively, correspond to the two maxima of the resulting distribution (Figure 4.4 (b)). The change of coordinates is then applied according to Equation 4.6. The result is shown in Figure 4.4 (f)

$$\begin{cases} EJ232\,Energy &= Amp. - Int.Charge \cdot \tan\left(\dfrac{90^\circ - \theta_B}{180^\circ/\pi}\right) \\ BGO\,Energy &= Int.Charge - Amp. \cdot \tan\left(\dfrac{\theta_P}{180^\circ/\pi}\right). \end{cases} \tag{4.6}$$

The following step consists in the energy calibration. In all the measurements carried out for the studies presented in the following chapters, the energy spectra

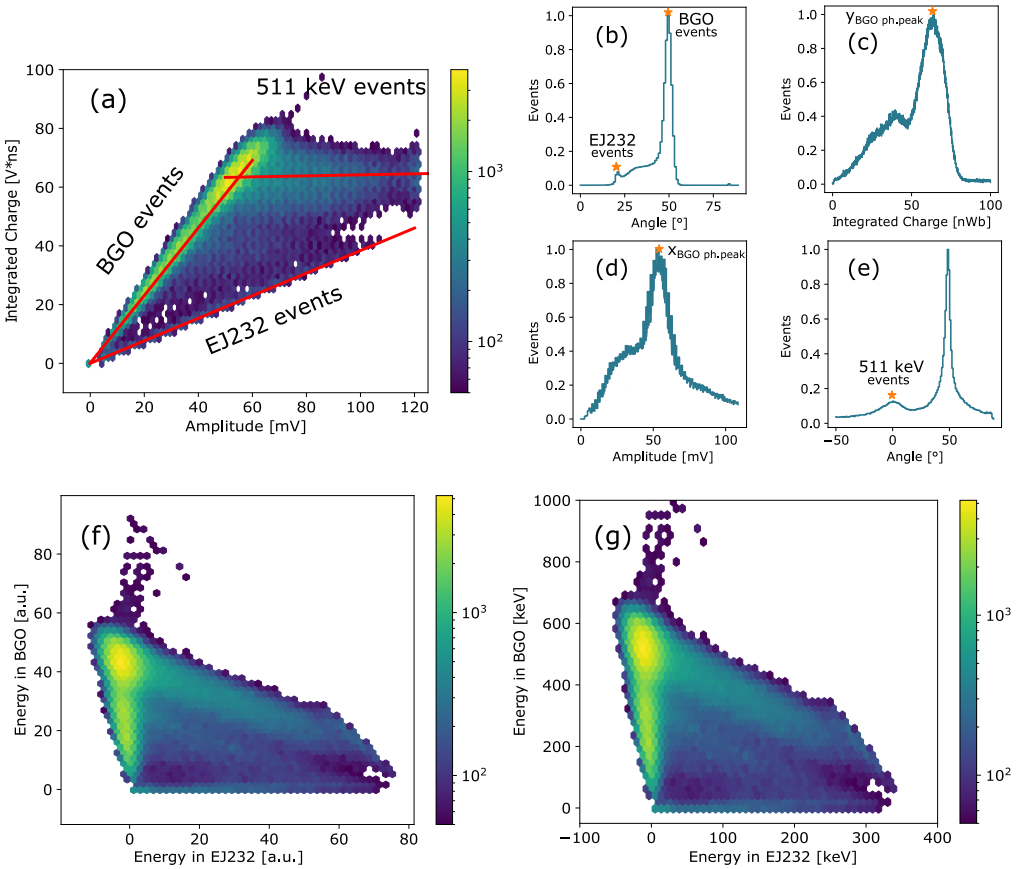

Figure 4.4: Illustration of the steps of the coordinates transformation. (a) Density scatter plot of integrated charge vs amplitude with BGO, EJ232 and 511 keV events outlined by red straight lines. (b) Angular distribution of the lines passing through the origin of the axis and each point in the density scatter plot. (c) Integrated charge distribution of all the events. (d) Amplitude distribution of all the events. (e) Angular distribution of the lines passing through the position of the photopeak in BGO and each point density scatter plot. (f) Density scatter plot resulting from the coordinates transformation. (g) Density scatter plot after energy calibration. Figure adapted from [85]

(amplitude and integrated charge) of the BGO and EJ232 heterostructures were acquired using SiPMs. The main assumption for the energy calibration is the SiPM saturation to be negligible. This is reasonable, considering the relatively low light yield of the two materials, the light loss due to not optimal light transport in heterostructures, and the SPAD size of the SiPM used. Depending on the considered study, the light extraction surface of the heterostructures ($3\times3\,mm^2$) was coupled to Hamamatsu SiPM with $6\times6\,mm^2$ active area and $50\,\mu m$ SPAD pitch or NUV-HD Broadcom SiPM with $3.7\times3.7\,mm^2$ active area with $30\,\mu m$ SPAD pitch.

With this assumption, only one point per axis (*EJ232 energy* and *BGO energy*) for which the deposited energy is known is enough to perform the energy calibration. One of these is clearly the photopeak of the BGO events, while for the energy calibration along the x-axis (*EJ232 energy*) the hypothetical photopeak in the plastic can be estimated.

In Figure 4.4 (a) an accumulation region extending from the photopeak in BGO to higher amplitude values can be observed: these are photopeak shared events with increasing energy deposited in plastic. Following this line, if the photoelectric interaction for the 511 keV γ-rays in the plastic was likely, the photopeak in EJ232 would be found. The hypothetical photopeak in EJ232 is then estimated from the intersection of the shared photopeak events with the EJ232 events. The line delineating the shared photopeak events is found by computing the angle of each line passing through the photopeak in BGO and any point on the scatter plot. First, the coordinates of the BGO photopeak ($X_{BGOph.peak}$,$Y_{BGOph.peak}$) are obtained from the fit of the integrated charge and amplitude distribution (Figure 4.4 (c) and (d)), then the angle is obtained as

$$\theta = 180°/\pi \cdot \arctan\left(\frac{Int.Charge - Y_{BGOph.peak}}{Amplitude - X_{BGOph.peak}}\right). \tag{4.7}$$

The main peak of the resulting distribution corresponds to BGO events, while the second one to the shared photopeak events. From the intersection between the latter and the EJ232 line, the hypothetical photopeak in EJ232 is estimated and the energy calibration along both axes is performed. The resulting density scatter plot is shown in Figure 4.4 (g).

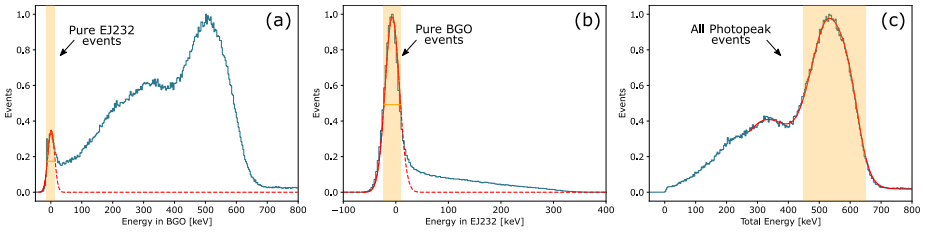

Figure 4.5: Distribution of energy deposited in BGO (a) EJ232 (b) and of total energy (c).

The photopeak events are selected as those with total reconstructed energy (sum of the energy deposited in BGO and EJ232) between 440–665 keV (Figure 4.5 (c)). The selection of the pure events is done by considering the distribution of the energy deposited in BGO and the energy deposited in EJ232, and taking the events under the peak at 0 keV (in BGO for pure EJ232 events and viceversa) within the FWHM of the same (see Figure 4.5 (a) and (b), respectively). For the selection of shared (photopeak) events, an arbitrary threshold is set at 50 keV of energy deposited in plastic to ensure the selection of events with an amount of energy deposited in the fast material sufficient to impact the overall timing. A complete overview of this classification is shown in the density scatter plot in Figure 4.6.

The occurrence of events with negative energy deposited in BGO or EJ232 should not be a concern. It is related to the smearing of the peak (due to non-infinite energy resolution) corresponding to events which do not deposit energy in one of the two materials. Looking at the distribution of the total energy deposited in the heterostructure, shown in Figure 4.5 (c), it only extends over positive values.

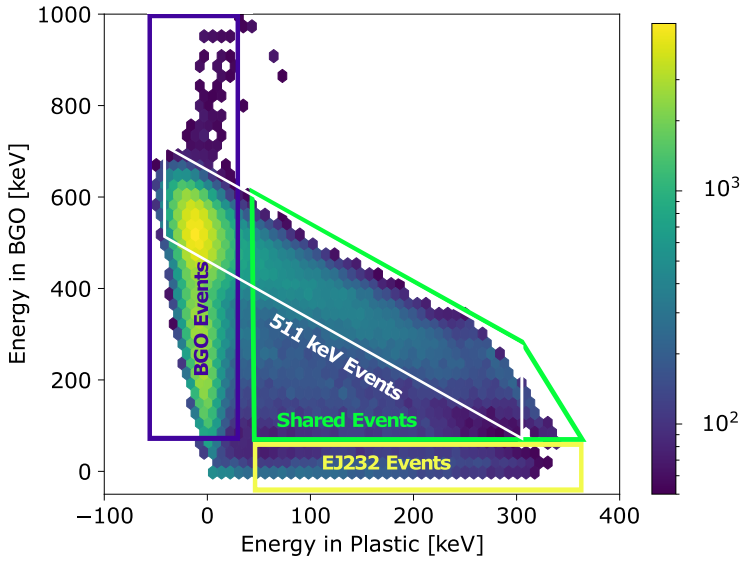

Figure 4.6: Classification of the events based on the energy deposited in BGO and EJ232. Pure BGO events (no energy deposited in EJ232); pure EJ232 events (no energy deposited in BGO); shared events (at least 50 keV deposited both in BGO and EJ232); photopeak events (reconstructed total energy between 440 keV and 665 keV); shared photopeak events (photopeak events with at least 50 keV deposited in EJ232).

4.4 Summary and Conclusion

Monte Carlo simulations with Geant4 toolkit were performed to investigate the energy sharing mechanism in BGO and plastic heterostructures. It was found that an heterostructure made of plates of BGO and plastic with 100 μm thickness each has the same photoelectric probability of LYSO. Additionally, with this geometry almost half of the photopeak events are shared, depositing at least 50 keV in plastic. For these reasons, this configuration has been selected as the optimal one. However, for the following studies, other configurations were also tested experimentally to better investigate the properties of heterostructure (Chapter 6 and Chapter 7) or due to practical difficulties in handling such thin layers (Chapter 8).

In Section 4.3 a possible method to classify the events according to material where the energy is deposited is presented. The proposed approach allows to estimate, within the limits of the energy resolution, the amount of energy deposited in each materials event-by-event. The events classification as described above is the basis for all the studies presented in the following chapters about BGO&EJ232 heterostructures.

Chapter 5

Light Production in Heterostructures

5.1 Introduction

The scintillation kinetics of standard scintillators is commonly described by the sum of bi-exponential function [4, 101]:

$$S(t) = \sum_{i=1}^{N} \frac{e^{-t/\tau_{r_i}} - e^{-t/\tau_{d_i}}}{\tau_{r_i} - \tau_{d_i}} \cdot w_i, \tag{5.1}$$

where τ_{r_i} and τ_{d_i} are the rise and decay components, respectively, and w_i is the weight of the $i-th$ component. It is reasonable to assume that when two materials are combined together, the scintillation kinetics of the resulting scintillator is given by the linear combination of the scintillation kinetics of the two materials, with a contribution that depends on the energy deposited in each. For a heterostructures, constituted by two materials A and B, the scintillation kinetics can therefore be formulated as:

$$S(t)_H = S(t)_A \cdot w(E_A) + S(t)_B \cdot w(E_B). \tag{5.2}$$

$S(t)_A$, $S(t)_B$ are the scintillation kinetics of the two materials individually as defined in Equation 5.1, and $w(E_A)$, $w(E_B)$ are the two weighting factors depending on the energy deposited in each.

In this chapter, the experimental validation of this assumption is shown. A $3{\times}3{\times}3\,\mathrm{mm}^3$ BGO&EJ232 heterostructure was measured in time-correlated single-photon counting (TCSPC) mode under 511 keV irradiation. The experimental setup used for this study allows for recording simultaneously the TCSPC signal and the scintillation pulse event-by-event [4]. The validation of Equation 5.2 relied on the analysis of the scintillation kinetics of events classified according to the amount of energy deposited in the two materials.

In Section 5.2, the mathematical model is described in detail for a heterostucture constituted by two generic materials. In Section 5.3, the experimental setup and the method are explained. Finally, the results are presented in Section 5.4.

5.2 Mathematical Model

5.2.1 Scintillation Kinetics

Let us consider a heterostructure composed of two generic scintillators A and B, each characterized by the time profile

$$\begin{aligned} S(t)_A &= \sum_{i=1}^{N_A} \tilde{w}_{i,A} \cdot s(t)_{i,A} \\ S(t)_B &= \sum_{i=1}^{N_B} \tilde{w}_{i,B} \cdot s(t)_{i,B}. \end{aligned} \tag{5.3}$$

as described in Equation 5.1, where the bi-exponential functions, for sake of convenience, are named $s(t)_{i,A}$ and $s(t)_{i,B}$. N_A and N_B are the number of decay component of each scintillator.

The weight ($\tilde{w}_{i,A/B}$) of each component is related to the number of photons produced according to the corresponding kinetics. More precisely, to the number of detected photons with that kinetics. Several parameters contribute to define $\tilde{w}_i$: the light yield (LY) of the material, the light transfer efficiency (LTE) to the photodetector, and the photon detection efficiency (PDE) of the latter.

Equation 5.2 can therefore be generalized into:

$$S(t)_H = N_{ph,A}(E_A) \cdot S(t)_A + N_{ph,B}(E_B) \cdot S(t)_B, \tag{5.4}$$

with $N_{ph,A}$ and $N_{ph,B}$ the number of detected photons from scintillator A and B, respectively:

$$\begin{aligned} N_{ph,A}(E_A) &= LY_A \cdot LTE_A \cdot PDE_A \cdot E_A \\ N_{ph,B}(E_B) &= LY_B \cdot LTE_B \cdot PDE_B \cdot E_B. \end{aligned} \tag{5.5}$$

It should be noticed that by imposing the constraint $\sum_i^N w_i = 1$, Equation 5.1 is normalized. To normalize Equation 5.4, the integral over time in the interval $[0, +\infty]$ needs to be computed. Additionally, the constraint $E_A + E_B = 1$ is imposed to have only one variable e.g., the fraction of energy deposited in scintillator A. The normalization factor then is $N_{ph,A}(E_A) + N_{ph,B}(E_A) \equiv N_{ph,TOT}(E_A)$ and Equation 5.4 can be expressed as:

$$\begin{aligned} \hat{S}(t)_H &= \frac{N_{ph,A}(E_A)}{N_{ph,TOT}(E_A)} \cdot S(t)_A + \frac{N_{ph,B}(E_A)}{N_{ph,TOT}(E_A)} \cdot S(t)_B \\ &= \frac{N_{ph,A}(E_A)}{N_{ph,TOT}(E_A)} \cdot \sum_{i=1}^{N_A} \tilde{w}_{i,A} \cdot s(t)_{i,A} + \frac{N_{ph,B}(E_A)}{N_{ph,TOT}(E_A)} \cdot \sum_{i=1}^{N_B} \tilde{w}_{i,B} \cdot s(t)_{i,B} \\ &\equiv n_{ph,A}(E_A) \cdot \sum_{i=1}^{N_A} \tilde{w}_{i,A} \cdot s(t)_{i,A} + n_{ph,B}(E_A) \cdot \sum_{i=1}^{N_B} \tilde{w}_{i,B} \cdot s(t)_{i,B} \end{aligned} \tag{5.6}$$

where $n_{ph,A}(E_A)$ and $n_{ph,B}(E_A)$ are the fraction of photons (over the total $N_{ph,TOT}$) produced by the scintillator A and B, respectively, as function of the fraction of energy deposited in A.

5.2.2 Effective Decay Time

An important figure of merit for timing, properly describing the decay kinetics of materials with multi-exponential decay components, is the effective decay time:

$$\tau_{\mathrm{d,eff}} = \sum_{i}^{N} \left(\frac{w_i}{\tau_{d,i}} \right)^{-1} \tag{5.7}$$

i.e., the weighted harmonic mean of all decay components.

According to Equation 5.6, the weight of each component is given by

$$\begin{aligned} w_{i,A} &= n_{ph,A}(E_A) \cdot \tilde{w}_{i,A} \\ w_{i,B} &= n_{ph,B}(E_A) \cdot \tilde{w}_{i,B}. \end{aligned} \tag{5.8}$$

By replacing them in the definition of the effective decay time, the expression for the effective decay time of heterostructures as a function of the fraction of energy deposited in one material is obtained:

$$\tau_{\mathrm{d,eff}} = \left[\sum_{i}^{N_A} \frac{n_{ph,A}(E_A) \cdot \tilde{w}_{i,A}}{\tau_{d,i_A}} + \sum_{i}^{N_B} \frac{n_{ph,B}(E_A) \cdot \tilde{w}_{i,B}}{\tau_{d,i_B}} \right]^{-1}. \tag{5.9}$$

From an application standpoint, having an analytical expression for $\tau_{\mathrm{d,eff}}$ is crucial, as it is one of the main parameters influencing the CTR (see Section 2.5):

$$CTR \propto \sqrt{\frac{\tau_{\mathrm{d,eff}}}{N_{ph,TOT}}} \tag{5.10}$$

Thus, knowing the scintillation properties and the stopping power (enabling to evaluate the fraction of energy deposited in one material over the total) of the materials constituting the heterostructure is enough to estimate its CTR. The experimental validation of Equation 5.10 for heterostructured scintillators is provided in the next chapter, Section 6.3.2.

5.3 Experimental Validation

5.3.1 Experimental Setup and Materials

For this study, a $3{\times}3{\times}3\,\mathrm{mm}^3$ heterostructure made of alternated plates of BGO and EJ232 was used. The heterostructure was hand-assembled in the workshop at CERN by stacking one plate on top of the other within a plastic holder, to keep the structure compact. The plastic holder had an open face and a hole was drilled in an adjacent face for reasons that will be clarified later in this section. BGO plates had a thickness of $100\,\mu\mathrm{m}$ according to what was concluded in Chapter 5. For EJ232 plates a thickness of $200\,\mu\mathrm{m}$ was chosen to maximize the energy deposited in plastic for shared events. This aspect will also become clearer later, in the next section.

The heterostructure was measured in TCSPC mode [102] under 511 keV irradiation (^{22}Na source) using the experimental setup schematized in Figure 5.1 (left) and described in [4].

The start-signal was given by a reference crystal ($3{\times}3{\times}15\,\mathrm{mm}^3$ LYSO:Ce) coupled to a Hamamatsu S13360-3050PE SiPM and readout by the NINO

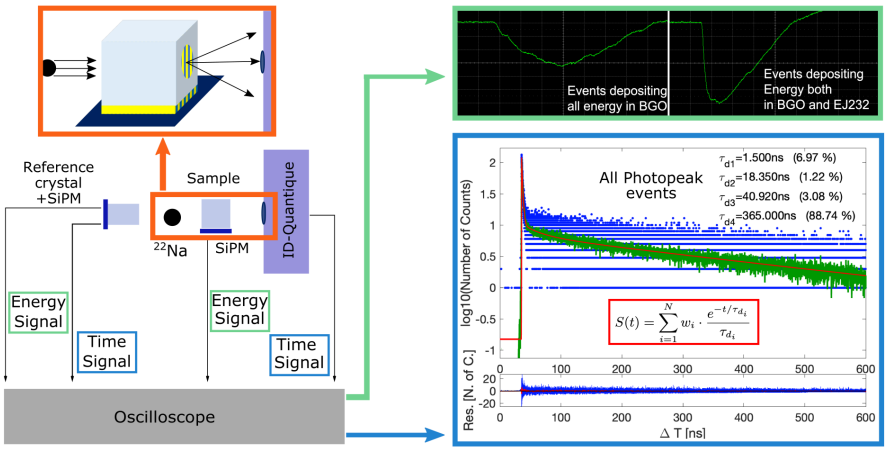

Figure 5.1: Scheme of the experimental setup (left) and examples of the output of the energy signal for different types of events (top right) and of the scintillation time profile resulting from TCSPC measurement (bottom right). The blue points represent the data, the green line is the smoothing of the histogram (performed via moving average), and the red one is the fit function. Figure published in [85]

chip [103], a low noise time-over-threshold comparator discriminator. Only the time information was extrapolated from the NINO ASIC, while for the energy information a linear operational amplifier (AD8000) was used. The waveforms were recorded event-by-event and the integral was evaluated in the off-line analysis. In this way, only photopeak events with full energy deposition in the starting crystal could be selected.

The stop-signal was given by an ID-Quantique (IDQ) ID100-50 sensor [104], detecting in TCSPC mode the light produced by the heterostructure. The hole drilled in one of the lateral faces of the holder allowed the ID-Quantique to collect light from the heterostructure while this was standing on a SiPM facing it with the open face (see Figure 5.1, top left). The SiPM used was from Hamamatsu (S13360-6050CS) and its signal output was processed by a linear operational amplifier equivalent to that of the starting detector (AD8000) to record the pulse shape of the heterostructure simultaneously with the TCSPC signal. The waveforms were recorded and analyzed off-line.

The impulse response function (IRF) of the system was measured by performing an analogous measurement but with a PbF_2 crystal replacing the heterostructure [105]. PbF_2 has a high refractive index, does not scintillate, and has good transparency in the NUV region. It is therefore a good, sole-Cherenkov radiator [15], and as Cherenkov emission is prompt, this allowed to accurately measure the IRF, accounting also for photon time spread in the crystal, resulting in 75 ps sigma.

5.3.2 Method

With the TCSPC setup previously described, the scintillation time profile of the heterostructure was measured (see Figure 5.1 bottom right) and correlated to the deposited energy.

The scintillation kinetics was evaluated for the different categories of events

separately: *pure BGO*, *pure EJ232*, *all photopeak*, and *shared photopeak* events with a specific amount of energy deposited in EJ232 (see Figure 5.2). The events selection was performed as described in Section 4.3 with a further classification of the shared photopeak events according to the amount of energy deposited in EJ232. Specifically, five intervals were selected, from a minimum of 50 keV to a maximum of 300 keV and 50 keV amplitude each of energy deposited in EJ232. The distribution of events within each of them was fairly uniform, so the mean energy deposited in EJ232 coincides with the average of the interval. Thus, for events with reconstructed deposited energy in plastic between 50 and 100 keV, the mean energy deposited here is 75 keV, corresponding to 15 % of the entire energy deposited (511 keV) in the heterostructure.

For all the events classes, the fit of the scintillation time profile was performed with the convolution between the sum of exponential functions (Equation 5.1) and the system IRF (Gaussian with 75 ps sigma measured as explained in Section 5.3.1).

First, the fit of the pure BGO and EJ232 events was performed leaving all parameters (exponential decay components and corresponding weights) free. Next, the fit of the shared photopeak events was performed by fixing the decay components according to the results obtained from the fit of the pure events and leaving only the corresponding weights as free parameters. The same was done for the individual classes of shared photopeak events with a given fraction of energy deposited in EJ232

For each class of events, the effective decay time was evaluated. By studying the dependency of the weights w_i and of the effective decay time on the fraction of energy deposited in plastic (over the total of 511 keV), the relation in Equation 5.2 was validated.

5.4 Results

In literature, rise-time values of 8 ps and 35 ps are reported for BGO and BC422 (a plastic scintillator equivalent to EJ232 but from a different producer), respectively [5]. As the IRF of the system was measured to be 75 ps sigma, the rise-time of the two materials could not be distinguished, therefore these parameters were fixed during the fit procedure. The decay-time constants and the corresponding weights were let free in the fit of the pure materials, and the obtained results (summarized in Table 5.1) are in good agreement with those measured from bulk materials [81, 106, 107]. This constitutes a validation of the coordinates transformation method and of the classification of pure events.

The fit of the photopeak events was performed by merging the fastest decay components of BGO and EJ232 into a single one (1.5 ns) as they were comparable (see Table 5.1), allowing to reduce the number of the degrees of freedom. The reduced chi-squared (χ^2) resulted ≈ 1 (see Table 5.1), confirming the goodness of fit for the shared events when using the decay components of pure materials and constituting a first validation of Equation 5.2.

The fit results of the shared photopeak events with increasing energy deposited in EJ232 are also summarized in Table 5.1. The reduced chi-squared (χ^2) between 0.85 and 0.9 is due to the limited statistics of events when selecting on a specific interval of energy deposited in plastic, leading to large fluctuations and a possible over-fitting. The shared photopeak events with $< E_P > = 75$ keV constitutes the

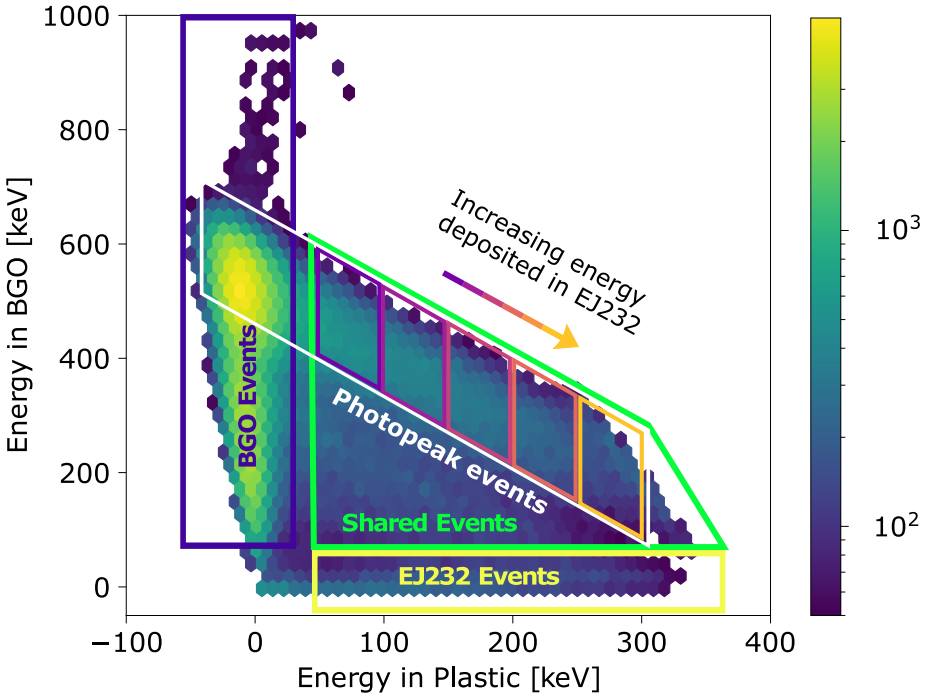

Figure 5.2: Density scatter plot showing the distribution of events depositing energy in BGO and in EJ232 and their classification. Figure published in [85].

Table 5.1: Results from the fit of decay scintillation of all the events classes considered. For *pure BGO* and *pure EJ232* events all the decay-time constants and the corresponding weights were free parameters. For photopeak events (both *all* and *shared*) the decay-time constant were fixed and only the corresponding weights were left free parameters.

Events Type	$\tau_{\text{d,fast}}(\tilde{w}_1)$ [ns (%)]	$\tau_{\text{d,middle-EJ232}}(\tilde{w}_2)$ [ns (%)]	$\tau_{\text{d,middle-BGO}}(\tilde{w}_3)$ [ns (%)]	$\tau_{\text{d,slow}}(\tilde{w}_4)$ [ns (%)]	$\tilde{\chi}^2$
Pure BGO	1.69 ± 0.06 (1.3 ± 0.1)	–	40 ± 7 (5 ± 1)	365 ± 23 (93.6 ± 0.1)	0.96
Pure EJ232	1.49 ± 0.05 (74 ± 1)	18 ± 2 (26 ± 3)	–	–	0.95
All Photopeak	1.5 (6.97 ± 0.04)	18 (1.2 ± 0.5)	40 (3.1 ± 0.9)	365 (88.7 ± 0.4)	0.99
Shared Photopeak with $< E_P >$					
75 keV	1.5 (11.9 ± 0.9)	18 (2.1 ± 0.6)	40 (2.5 ± 0.7)	365 (83.6 ± 0.2)	1.02
125 keV	1.5 (18.8 ± 0.2)	18 (5 ± 1)	40 (1.9 ± 0.6)	365 (74.8 ± 0.7)	0.89
175 keV	1.5 (22.4 ± 0.2)	18 (6 ± 1)	40 (1.6 ± 0.5)	365 (70.3 ± 0.7)	0.88
225 keV	1.5 (29.1 ± 0.3)	18 (8 ± 2)	40 (1.3 ± 0.4)	365 (61.6 ± 0.6)	0.85
275 keV	1.5 (34.3 ± 0.3)	18 (10 ± 3)	40 (1.0 ± 0.3)	365 (55.1 ± 0.6)	0.85

8.5 % of the all photopeak events, and this percentage decreases further with E_P increasing: only the 2.3 % of all photopeak events have $< E_P > = 275$ keV. The low statistics also explains the high relative error obtained for w_2 and w_3, the weights of the two minor components of EJ232 and BGO, respectively.

Figure 5.3 shows the obtained fit functions for *pure BGO*, *pure EJ232*, and

shared photopeak events with increasing energy deposited in plastic. The shortening of the decay tail as the contribution from EJ232 increases can be appreciated.

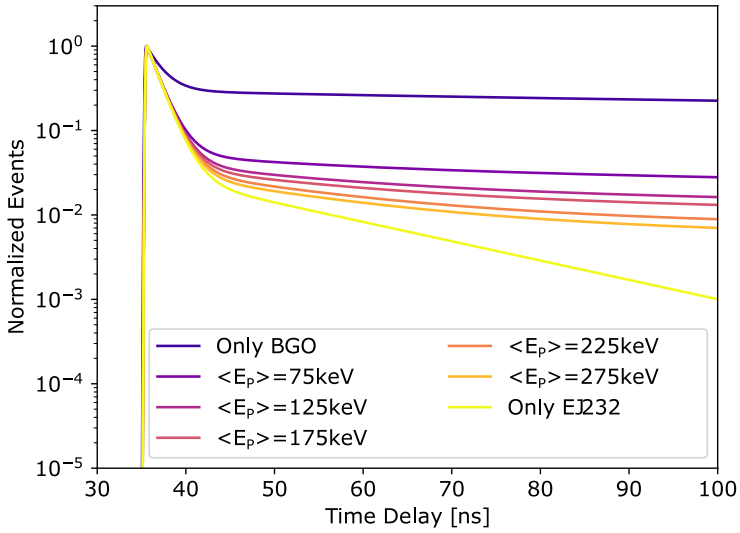

Figure 5.3: Comparison between the normalized fit function of *pure BGO*, *pure EJ232*, and *shared photopeak* events with increasing energy deposited in plastic. Figure adapted from [85].

The specific choice of BGO and EJ232 as materials to combine in a heterostructure allows for some approximations which lead to a simplification of Equation 5.6. Assuming LY, LTE, and PDE to be the same for the two materials, Equation 5.6 becomes

$$S(t)_H = e_P \cdot S(t)_P + (1 - e_P) \cdot S(t)_B. \tag{5.11}$$

where e_P is the mean fraction of energy deposited in EJ232 (i.e., $e_P =< E_P > /511\,\text{keV}$) and $S(t)_P$ and $S(t)_B$ are the scintillation time profiles of plastic and BGO, respectively, namely:

$$\begin{aligned} S(t)_P &= \tilde{w}_{1,P} \cdot s(t)_1 + \tilde{w}_{2,P} \cdot s(t)_2 \\ S(t)_B &= \tilde{w}_{1,B} \cdot s(t)_1 + \tilde{w}_{3,B} \cdot s(t)_3 + \tilde{w}_{4,B} \cdot s(t)_4. \end{aligned} \tag{5.12}$$

By making $S(t)_P$ and $S(t)_B$ explicit in Equation 5.11, the weights of the four decay components in the heterostructure ($w_{1,2,3,4}$) were found to be linear with the fraction of mean energy deposited in plastic:

$$\begin{aligned} S(t)_H =& e_P \cdot [\tilde{w}_{1,P} \cdot s(t)_1 + \tilde{w}_{2,P} \cdot s(t)_2] + \\ &+ (1 - e_P) \cdot [\tilde{w}_{1,B} \cdot s(t)_1 + \tilde{w}_{3,B} \cdot s(t)_3 + \tilde{w}_{4,B} \cdot s(t)_4] \\ =& [\tilde{w}_{1,B} + (\tilde{w}_{1,P} - \tilde{w}_{1,B}) \cdot e_P] \cdot s(t)_1 + [\tilde{w}_{2,P} \cdot e_P] \cdot s(t)_2 + \\ &+ [\tilde{w}_{3,P} - \tilde{w}_{3,P} \cdot e_P] \cdot s(t)_3 + [\tilde{w}_{4,P} - \tilde{w}_{4,P} \cdot e_P] \cdot s(t)_4 \end{aligned} \tag{5.13}$$

and according to Equation 5.2:

$$
\begin{aligned}
w_1(e_P) &= \tilde{w}_{1,B} + (\tilde{w}_{1,P} - \tilde{w}_{1,B}) \cdot e_P \\
w_2(e_P) &= \tilde{w}_{2,P} \cdot e_P \\
w_3(e_P) &= \tilde{w}_{3,P} - \tilde{w}_{3,P} \cdot e_P \\
w_4(e_P) &= \tilde{w}_{4,P} - \tilde{w}_{4,P} \cdot e_P.
\end{aligned}
\tag{5.14}
$$

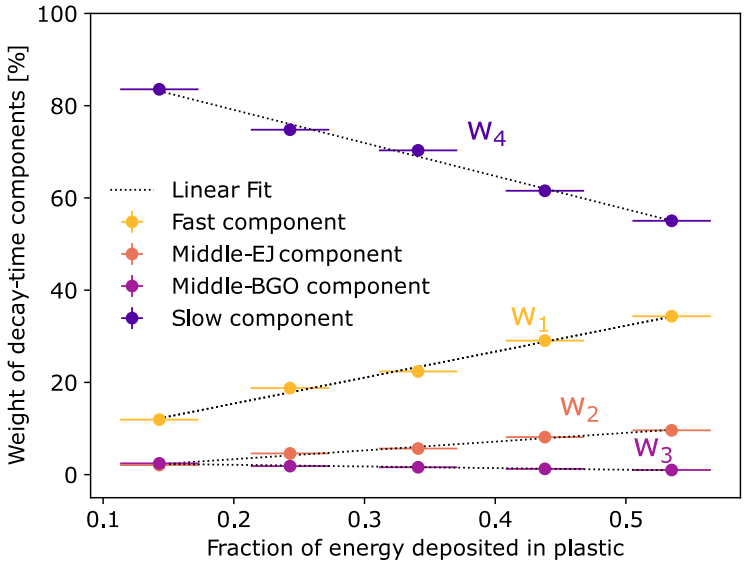

Figure 5.4: The weights of the four decay components of the 511 keV shared events are represented as a function of the fraction of the mean energy deposited in plastic (e_P), for each group of events. Figure published in [85]

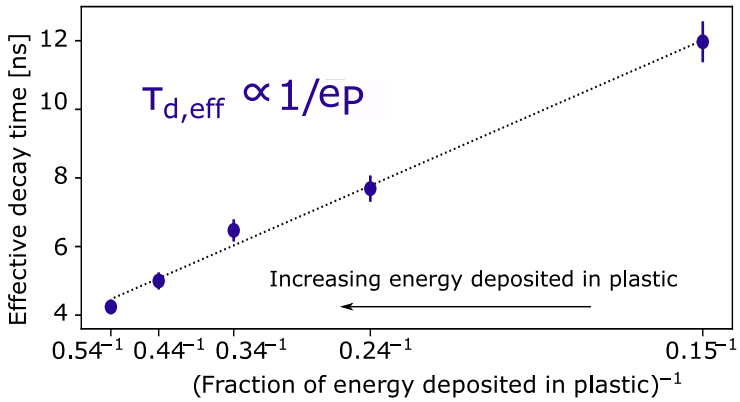

Figure 5.5: Effective decay time as a function of the inverse of the fraction of the mean energy deposited in plastic ($1/e_P$). Figure published in [85].

This result found experimental confirmation as shown in Figure 5.4. It is worth to mention that the reported values are not corrected by the photon detection efficiency of the IDQ which was assumed to be the same for the two materials. Actually, the PDE of the IDQ at the peak emission of EJ232 and BGO

is about 15 % and 30 %, respectively [104], which explains the high contribution from BGO even when we are considering events with 55 % of energy deposited in plastic.

After obtaining the analytical expressions of $w_{1,2,3,4}$ as a function of e_P (Equation 5.14), they were replaced into the definition of the effective decay time (Equation 5.7). A linear dependency between the effective decay time and the reverse of e_P ($\tau_{\mathrm{d,eff}} \propto 1/e_P$) was found. This relation too found experimentally validation, as it can be seen from the linear fit of the measured decay time as a function of the mean fraction of energy deposited in plastic shown in Figure 5.5.

5.5 Summary and Conclusion

The aim of this chapter was to investigate the scintillation kinetics of heterostructures. The scintillation kinetics of standard bulk materials is well described by the sum of bi-exponential functions. When two or more materials are combined in heterostructured scintillators, it is reasonable to assume that the resulting scintillation kinetics can be determined by a linear combination of the constituent materials' scintillation kinetics. The contribution of each material is determined by the fraction of energy deposited in it over the total energy deposited (Equation 5.2).

First, the model was illustrated for two generic materials combined together. The analytical expression for the factors weighing the contribution of these two materials is obtained as a function of the energy deposited in each material. Accordingly, also the effective decay time (Equation 5.7) was expressed as a function of the energy deposited in the two materials.

Afterwards, the experimental validation is presented using a BGO&EJ232 heterostructure of size $3{\times}3{\times}3\,\mathrm{mm}^3$. The selection of these two materials allows for certain approximations, leading to a simplification of the analytical expression of the weighting factors and the effective decay time. The former resulted linearly dependent on the fraction of energy deposited into the plastic, while the latter resulted inversely proportional to it. The measurements were performed with a TCSPC setup using 511 keV irradiation capable of simultaneously recording the TCSPC signal and pulse shape on an event-by-event basis [4, 105]. This made it possible to classify events according to both the total amount of energy deposited (enabling the selection of photopeak events) and the material in which the energy was deposited. The scintillation kinetics was then separately analyzed for each class of events identified, as a function of the energy deposited in the plastic scintillator.

Chapter 6

Exploring the Coincidence Time Resolution of Heterostructures

6.1 Introduction

The ultimate parameter defining the performances of TOF-PET detectors is the coincidence time resolution (CTR). The main focus of this chapter is to show the timing improvement which can be achieved with BGO&EJ232 heterostructured scintillators compared to bulk BGO. The experimental setup used for these measurements comprises a high-frequency front-end electronics [9, 108], the state-of-the-art for timing measurements.

Furthermore, this chapter explores the relationship between the CTR and the effective decay time in heterostructured scintillators, as introduced in the previous chapter (Section,5.2.2). The impact of light transport on the CTR is also investigate. In particular, the focus is on understanding the effect of depth-of-interaction (DOI) uncertainties and presenting the experimental validation of a simple model describing this phenomenon.

By delving into these aspects, we aim to improve the understanding of timing performances in heterostructured scintillators, setting the stage for further developments of this type of detectors. A first assessment of the energy resolution in heterostructure is also provided.

This chapter is organized as follows: the materials and the setup are described in detail in Section 6.2. In Section 6.3.1 the CTR results of the measured samples are presented. Section 6.3.2 and Section 6.3.3 show the experimental validation of analytic models describing the CTR and the blurring due to DOI uncertainties, respectively. Finally, in Section 6.3.4, the energy resolution is discussed.

6.2 Materials and Method

6.2.1 Samples

Four different heterostructured pixels were assembled in our workshop at CERN. According to the results of the Monte Carlo simulations about energy sharing (Section 4.2), the thickness of BGO plates was set to 100 μm in all cases. For the EJ232 plates, two different thicknesses were chosen: 100 μm and 200 μm. The former was also selected according to the results of the simulation study, indicating that when both plastic and BGO plates are 100 μm thick, the photoelectric probability of the heterostructure is comparable to that of an LYSO crystal of the same size. The latter was instead selected to explore the timing limits of this kind of structure. As evident from the previous two chapters, the thicker the plastic the more energy is deposited here, resulting in the generation of more fast photons and ultimately enhancing the timing performance.

For each plastic thickness, two different lengths were chosen, 3 mm and 15 mm long (both with cross-section 3×3 mm^2), allowing to investigate the effect of light transport and DOI blurring in heterostructured scintillators.

From here on, the 3 mm and 15 mm long heterostructures will be referred to as *short* and *long*, respectively. While, to distinguish the heterostructure with different EJ232 thickness, the label 1:1 (100 μm thick BGO and 100 μm thick EJ232) and 1:2 (100 μm thick BGO and 200 μm thick EJ232) will be used. All the configurations measured are summarized in Figure 6.1.

To establish the timing improvement of heterostructures, a 3×3×15 mm^3 bulk BGO crystal was measured as a comparison. In addition, a pixel made of a stack of BGO plates 100 μm was tested to disentangle the effect of light transport and DOI due to the layered structure and to the combination of two materials with different optical properties.

For all the layered samples considered, the 3×3 mm^2 and 3×15 mm^2 surfaces of both BGO and EJ232 were polished, while the edges were depolished. All samples were wrapped in enhanced specular reflector (ESR), except for the surface coupled to the SiPM, to maximize the light collection.

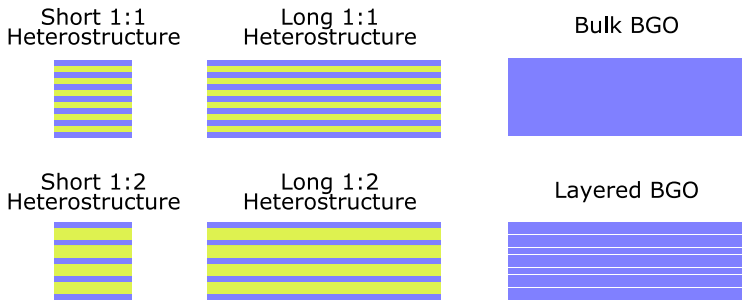

Figure 6.1: Diagram of the samples measured: 3×3×3 mm^3 (short) and 3×3×15 mm^3 (long) heterostructures with 100 μm thick EJ232 plates (1:1) and 200 μm thick EJ232 plates (1:2), 3×3×15 mm^3 bulk BGO and 3×3×15 mm^3 layered BGO. In all cases (except the bulk configuration) the BGO plates are 100 μm thick.

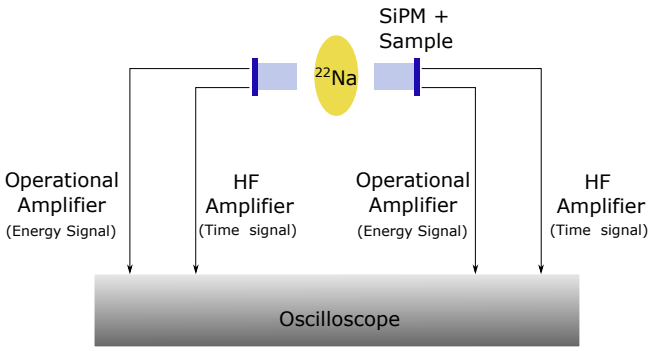

Figure 6.2: CTR bench: two samples are placed at the opposite side of a ^{22}Na source and measured in coincidence. They are coupled to SiPMs whose signal is read out by a custom-made front-end electronics which processes separately the energy (operational amplifier) and time information (HF amplifier) to optimize the resolution on both channels.

6.2.2 CTR Bench and High-Frequency Readout

The CTR bench consists of two samples placed at the opposite side of ^{22}Na source and measured in coincidence. Each sample is coupled to a SiPM whose output is processed by a custom-made front-end electronics. It comprises two separate paths to separately process the timing and energy information. For timing, an high-frequency (HF) amplifier is used. It consists of a balun transformer connected between the cathode and anode of the SiPM to two BGA616 radio-frequency (RF) amplifiers in cascade, in a balanced-to-unbalanced configuration [9]. This type of circuit is called passive compensation and is an attractive amplification techniques because it does not require injection of noise and guarantees circuit stability [108]. This circuit efficiently amplifies and extracts the high-speed high bandwidth signal from the SiPM. The bandwidth of the HF signal was measured to be about 1.5 GHz. Because of the large voltage amplification, a second path to separately process the energy information was designed. It was realized with a standard AD8000 operational amplifier circuit which does not significantly affect the timing channel bandwidth nor introduce additional electronic noise [9].

The output signals are finally digitized by a LeCroy DDA735Zi oscilloscope (3.5 GHz bandwidth, 20 Gs/s sample rate). A sketch of the experimental setup is shown in Figure 6.2.

Each sample to test (heterostructures, bulk BGO, and layered BGO) was measured in coincidence with a reference crystal ($2\times2\times3\,\mathrm{mm}^3$ LSO:Ce:0.4%Ca, CTR $= 61 \pm 3$ ps FWHM). Both the reference crystal and the test-samples were coupled to the SiPMs with Cargille Meltmount glue (refractive index $n = 1.582$, transmission cutoff at about 300 nm). For the test-samples, a $3.7\times3.7\,\mathrm{mm}^2$ Broadcom SiPM 30 μm SPAD size (AFBR-S4N44C013) [109], biased with an overvoltage of about 11 V, was used. This type of SiPM provides a PDE higher than 50 % (at 38 V bias voltage, about 11 V over voltage) for both EJ232 and BGO emission (360-500 nm) as well as intrinsic SPTR of 88 ± 6 ps FWHM [5].

All samples were measured in *head-on* or *PET like* configuration i.e., in front irradiation. The long pixels were also measured in *DOI* configuration i.e., in electronically collimated side irradiation. The two configurations are shown in

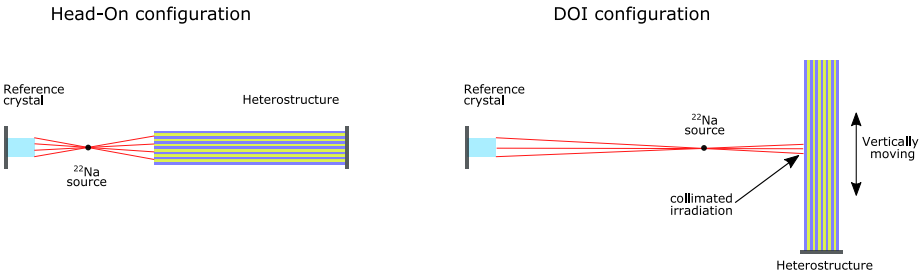

Figure 6.3: Scheme of the Head-On (left) and DOI (right) configuration for the CTR measurements of $3\times3\times15\,\mathrm{mm}^3$ samples. Figure published in [81].

Figure 6.3. The collimation was performed by placing the source 80 mm distant from the reference detector and 10 mm away from the sample. By moving the heterostructure along the vertical direction, five different spots along the DOI coordinate, equally separated by approximately 3.5 mm, were irradiated.

6.2.3 Data Acquisition and Analysis

The necessary information for the analysis was directly extrapolated from the waveforms at the oscilloscope. Figure 6.2 illustrates all the measurements performed on the waveforms: amplitude, integrated charge, time delay, signal rise time.

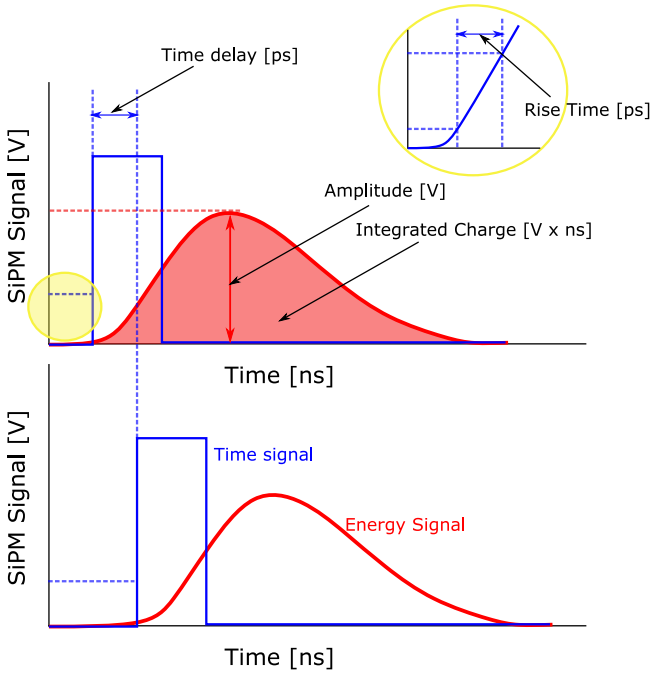

Figure 6.4: Diagram of the SiPM signal outputs of the two detector in coincidence digitized by the oscilloscope and the extrapolated measurements.

The measure of the deposited energy inside both the reference detector

and the test-sample was obtained by recording the integral (time window of about 160 ns) and the amplitude of the energy signal. The recording of both information was specifically necessary for the heterostructures pixel, as the photopeak selection was performed afterward the coordinates transformation described in Section 4.3. Among the photopeak events in the heterostructures, the *shared* photopeak events were selected as those depositing more than 50 keV in plastic. The threshold was set at 50 keV to ensure the selection of events with an amount of energy deposited in the fast material sufficient to impact the overall timing.

After selecting the photopeak events in both detector arms, the timing was analyzed. The timestamps for each event were extracted via the leading-edge time pick-off method. The leading edge threshold was placed, for both detector arms, above the electronic noise level and below the signal amplitude of a single SPAD, which for $3.7\times3.7\,\mathrm{mm}^2$ Broadcom SiPM at 11 V overvoltage is about 30 mV. From the difference between the timestamp of the reference crystal and the test sample, the time delay distribution was obtained.

Despite by placing the leading-edge threshold just above the noise the time walk effect is reduced, this cannot be removed completely. However, by recording the signal rise time, defined as the time difference between the crossing of two fixed thresholds (see Figure 6.4), it can be corrected offline [110] as described in the next subparagraph.

Finally, the corrected time-delay distribution was considered for both *all* and only *shared* photopeak events, and the FWHM was evaluated. It should be pointed out that, as we are not measuring two identical crystals in coincidence, the measured FWHM is not a direct measurement of the CTR. This can be obtained, in first approximation, by correcting the measured FWHM for the contribution of the reference by quadratic subtraction and then multiplying by $\sqrt{2}$. This approximation is based on the assumption to have on both sides two identical detectors. However, this is not entirely true for heterostructured scintillators, where different types of events can occur on the two sides. This aspect will be clarified and investigated in the next chapter (Section 7.3.4).

Time walk correction based on rise time

The time walk effect is a phenomenon that occurs when measuring the timing or arrival time of signals. It refers to the variation in the measured timestamp of an event due to differences in the amplitude of the measured signals. This effect is particularly noticeable when using the leading-edge pick-off method, i.e. measuring the time it takes for the signal to reach a certain threshold voltage level at the rising edge of the signal waveform. In particular, smaller signals tend to be measured with a delayed timestamp compared to larger signals, even if they have the same time of arrival. This concept is illustrated in Figure 6.5.

A correction can be implemented off-line to compensate for this effect by measuring the signal-rise time [110], as smaller signals that are observed to have longer timestamp (i.e. larger time delay) are also characterized by larger signal rise-time.

The correlation between the measured time delay and the rise time is shown in Figure 6.6 (a). The two peaks in the rise time distribution are due to the different types of events: the peak centered at slower rise time corresponds to BGO events, while the peak centered at faster rise time is due to shared events

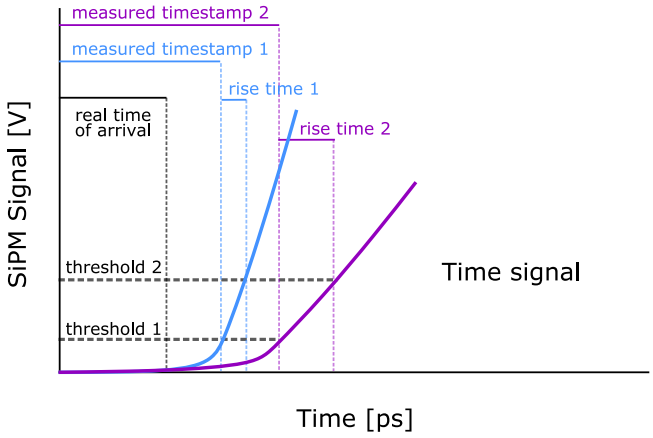

Figure 6.5: Time walk effect. When events have same time of arrival but generate signals of varying amplitudes, their timestamps are observed to differ. Smaller signals are observed to have longer timestamp and larger signal rise time. This correlation is used to correct for time walk effect off-line.

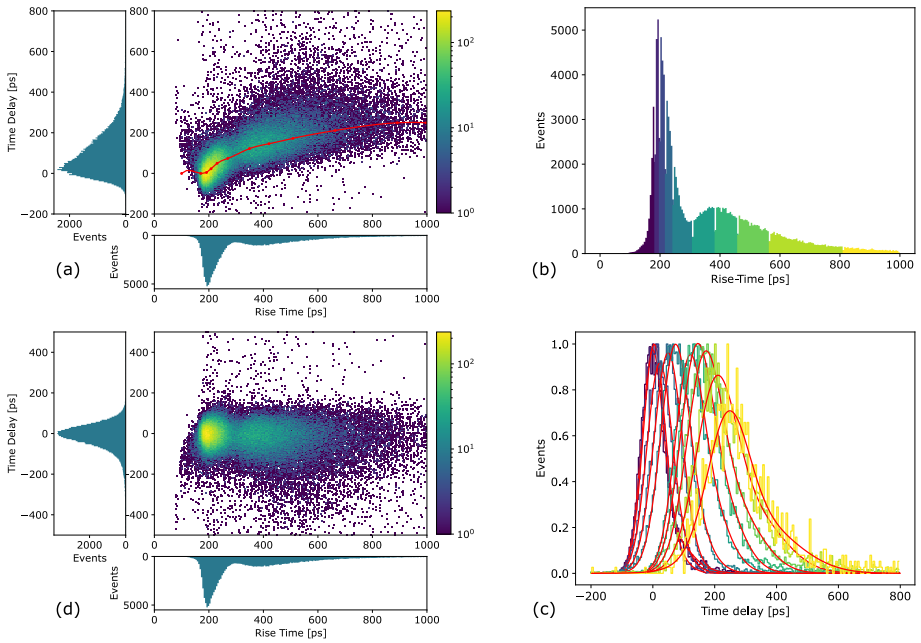

Figure 6.6: Time walk correction procedure. (a) 2D histogram showing the correlation between the measured time delay and signal rise time, and projection of the two distributions. (b) Rise time distribution divided in ten intervals containing approximately the same number of events. (c) Time delay distribution corresponding to the identified rise time intervals, fitted with the sum of two Gaussian. The peak position was extrapolated for each distribution. For a visual representation of the shift of the time delay together with the rise time, the obtained peak positions were superimposed to the 2D histogram in (a). (d) 2D histogram after performing the time walk correction using the calibration curve obtained using interpolating the peak positions of the time delay distribution (red curve in (a)).

with a significant contribution from EJ232.

The rise time distribution was divided into 10 intervals containing approxi-

mately the same number of events (Figure 6.6 (b)). For each of these intervals, the time delay distribution was considered and the peak position of the distribution was extrapolated by performing a fit with the sum of two Gaussian functions (Figure 6.6 (c)). The peak positions were interpolated with a cubic function (using the `CubicSpiline` function from the python library `Scipy`) to obtain the calibration curve (Figure 6.6 (a)). For each event the signal rise time was considered, the corrective factor was computed according to the obtained calibration curve and subtracted to the corresponding time delay. The resulting time delay distribution is shown in Figure 6.6 (d).

It is worth noting that typical time walk correction procedure primarily relies on signal amplitude. However, in the case of BGO , a significant time walk occurs due to fluctuations in the production of Cherenkov photons. While Cherenkov photons promptly accelerate the rising leading edge of the signal, their low photon count has minimal impact on signal amplitude [110]. Therefore, by basing the correction on signal rise time rather than signal amplitude allows for taking into account this additional category of events.

6.3 Results

6.3.1 Assessment of Timing Improvement

Table 6.1 presents a summary of the CTR results of all the samples measured in head-on configuration. A noticeable degradation of the CTR can be observed when transitioning from a bulk to a layered structure with only BGO plates, going from 271 ± 14 ps to 303 ± 15 ps. However, the CTR of the heterostructures, comprising both BGO and the fast EJ232 plastic scintillator, shows significant improvement compared to bulk BGO, even when not distinguishing between *all* and *shared* photopeak events. By applying this distinction and considering only the *shared* photopeak events, the improvement is even more pronounced. Specifically, the CTR of the long 1:1 heterostructure when considering *all* photopeak events is 239 ± 12 ps and it improves to 214 ± 11 ps when selecting only the *shared* photopeak events. With the long 1:2 heterostructure CTR values below 200 ps were obtained both for *all* and *shared* photopeak events: 197 ± 10 ps and 173 ± 9 ps, respectively. The time delay distribution of bulk BGO and the long heterostructures are shown in Figure 6.7.

Table 6.1: CTR results of all the samples measured in head-on configuration: short ($3\times3\times3\,mm^3$) and long ($3\times3\times15\,mm^3$) heterostructure with 100 μm thick plastic plates, with 200 μm thick plastic plates, long bulk and layered BGO. For the heterostructures the CTR of both *all* 511 keV and *shared* 511 keV is reported. For both the heterostructure and layered BGO the thickness of BGO plates was 100 μm.

	bulk BGO	layered BGO	100 μm EJ232		200 μm EJ232	
	long	long	short	long	short	long
CTR [ps] All 511 keV	271 ± 14	303 ± 15	155 ± 8	239 ± 12	142 ± 7	197 ± 10
CTR [ps] Shared 511 keV	//	//	126 ± 6	214 ± 11	114 ± 6	173 ± 9

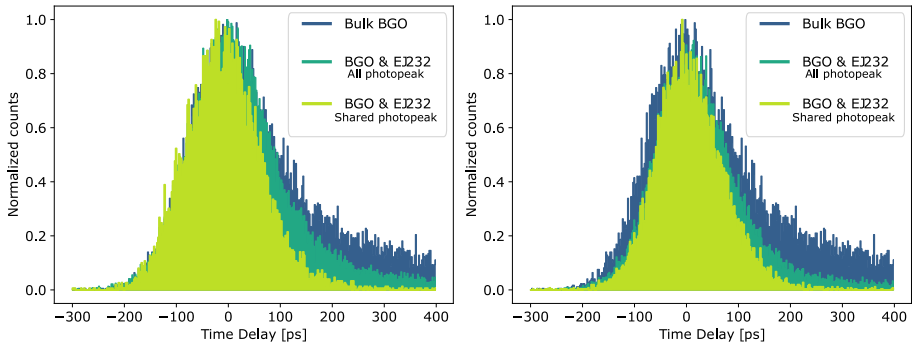

Figure 6.7: Time delay distribution of bulk BGO compared to the long 1:1 heterostructure (a) and to the long 1:2 heterostructure (b). For both heterostructures, the time delay distribution of both all photopeak and only shared photopeak events is shown.

6.3.2 Analytic expression of CTR

For bulk scintillators it is well established that the CTR is inversely proportional to the square root of the photon time density (Equation 5.10) [5]. It is reasonable to assume that this also applies to heterostructured scintillators, with some clarifications.

In Section 5.4, the concept of effective decay time has been extended to heterostructured scintillators. As with bulk scintillators, it is given by the weighted harmonic mean of all the decay component (of both materials). Let us assume that this is an appropriate figure of merit to describe the decay kinetics for heterostructured scintillators as well. In case of a heterostructure constituted by two generic scintillators A and B, Equation 5.10 can be then generalized into:

$$CTR_{E_A} \propto \sqrt{\frac{\tau_{\mathrm{d,eff}_H}(E_A)}{N_{ph,A}(E_A) + N_{ph,B}(E_A)}}, \tag{6.1}$$

where $N_{ph,A}(E_A)$, $N_{ph,B}(E_A)$, defined as in Equation 5.5, are the number of photons detected from material A and B, respectively, in function of the fraction of energy deposited in A over the total energy deposited in the heterostructure. It must be emphasised that Equation 6.1 gives the CTR of only those events with energy fraction E_A deposited in material A. To obtain the overall CTR of the heterostructure, one must sum all the CTR_{E_A} contributions (with E_A ranging from 0 to 1) weighted by the probability of depositing that particular fraction of energy in A.

The experimental validation of Equation 6.1 was performed by measuring the CTR of the short 1:2 heterostructure. Specifically, the same heterostructure pixel of the study presented in the previous Chapter 6 was used and the same measurement conditions (Hamamatsu SiPM S13360-6050CS, air coupling) were adopted. In this way, by performing an equivalent events selection to the one used for studying scintillation kinetics, the CTR was correlated to the effective decay time measured for each events class.

In first approximation, for the specific case considered with BGO and EJ232, we can assume that the total number of photons ($N_{ph,TOT} = N_{ph,A}(E_A) +$

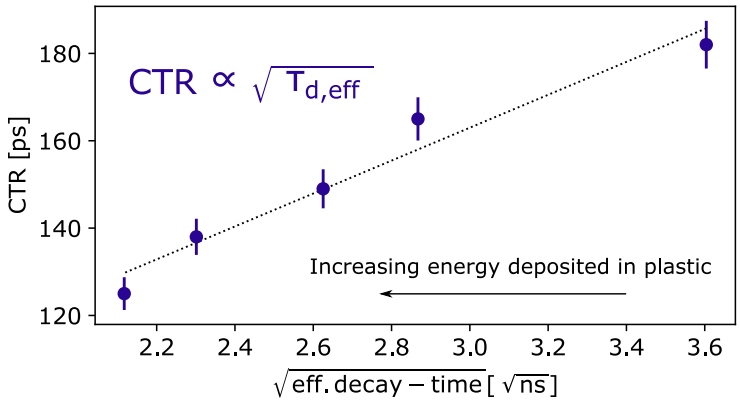

Figure 6.8: CTR of $3\times3\times3\,mm^3$ 1:2 heterostructure as a function of the effective decay time. Figure published in [85].

$N_{ph,B}(E_A)$) does not depend on E_A (see Section 5.4). Thus, Equation 6.1 becomes:

$$CTR_{E_A} \propto \sqrt{\tau_{\mathrm{d,eff}_H}(E_A)}. \tag{6.2}$$

This relation found experimental confirmation, as shown in Figure 6.8.

6.3.3 DOI blurring

Figure 6.9 summarizes the CTR results of all the heterostructures and configurations tested, distinguishing between *all* (Figure 7.3a) and only *shared* (Figure 7.3b) photopeak events. The CTR in head-on configuration for bulk and layered BGO are also added as comparison.

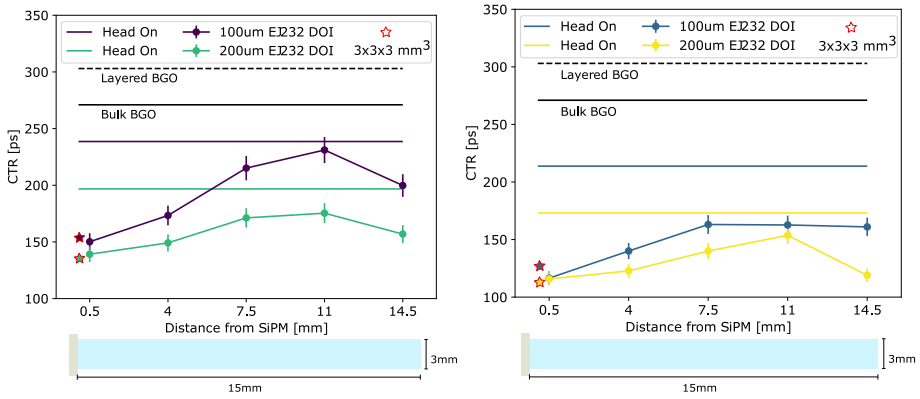

Figure 6.9: CTR results of all the heterostructures tested (100-100 and 100-200 configuration), both in head-on (straight lines) and DOI (dots) configuration, considering *all* 511 keV events (a) and the only *shared* 511 keV events (b). These are then compared to the CTR at 511 keV of a pure BGO crystal (solid black line) and of a layered BGO (dashed black line) pixel with the same dimension of the heterostructures. Figure published in [81].

It can be seen that the CTR of the short heterostructures is comparable to that of the corresponding long heterostructure when only the DOI closest

to the SiPM is irradiated. The DOI closest to the SiPM is also the one that provides the best CTR, then we see that the CTR worsens when moving away from the SiPM and it improves again when reaching the opposite face of the SIPM. A similar trend of CTR as a function of DOI (see Figure 6.9) has been previously observed for bulk materials as well [111], and it can be understood by considering the key factors contributing to the CTR.

The primary one is the light output (LO), which is larger for DOIs closer to the SiPM. Since CTR scales inversely with the square root of the light output, one might expect a consistent improvement in CTR as the DOI approaches the SiPM. However, Figure 6.9 shows that this is not the case.

Another important effect to consider is the photon time spread (PTS). Because of the high aspect ratio of the long pixels – $3\times3\times15\,\mathrm{mm}^3$ – the first scintillation photons reaching the extraction face are mainly those emitted directly toward the SiPM (*direct photons*) or in the opposite direction and then reflected back to the SiPM (*reflected photons*). For interactions occuring far away from the SiPM, the path of direct and reflected photons is approximately the same and the two categories reach the photodetector at the same time. While, as the DOI gets closer to the SiPM, the difference in the distance traveled by direct and reflected photons increases and so does the variance in the arrival times of optical photons increases, leading to a worsening of the CTR. The distinction between these two categories was first observed in simulation studies [112], [113]. Then, thanks to the use of fast and high time precision electornics readout, it was observed also experimentally [15], [16].

The combination of these two effects (LO and PTS) explains why the worse CTR values are obtained for interaction in the central part of the pixels.

The longer the crystal, the larger the PTS and the variation in LO for different DOIs. This is the main reason why the CTR worsens with the crystal length [73]. In the specific study, a CTR of 155 ps was measured for the short 1:1 heterostructure, worsening to 239 ps for the long one. Similarly, for the 1:2 heterostructures a CTR of 142 ps and 197 ps where measured for the short and long geometry, respectively.

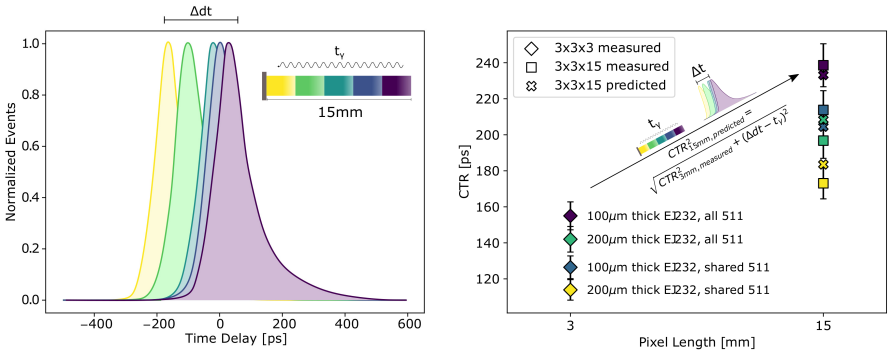

(a) **(b)**

Figure 6.10: (a) Shift of the coincidences peak with DOI. (b) CTR experimental results of both $3\times3\times3\,\mathrm{mm}^3$ (diamonds) and $3\times3\times15\,\mathrm{mm}^3$ (squares) heterostructure (with EJ232 plates thickness of 100 μm and 200 μm, considering *all* and only *shared* photopeak events) and predicted CTR of $3\times3\times15\,\mathrm{mm}^3$ heterostructure (crosses). This latter is obtained adding to the experimental CTR value of $3\times3\times3\,\mathrm{mm}^3$ the DOI blurring. Figure published in [81].

This effect was quantified using the information coming from DOI measurements, specifically the shift of the time delay peak according to the irradiated DOI (see figure 6.10a). The DOI blurring along the pixel was approximated as the shift of the time delay peak from the first to the last DOI (Δdt) minus the time that the γ-ray takes to go from the first to the last DOI (t_γ). Both these concepts are illustrated in figure 6.10a. Assuming that the short heterostructures are not affected by any light transport effect and by adding in quadrature the contribution so estimated to their CTR

$$CTR_{\text{15mm, predicted}} = \sqrt{CTR^2_{\text{3mm, measured}} + (\Delta dt - t_\gamma)^2}, \tag{6.3}$$

it was possible to estimate with a good accuracy the CTR of the long pixels, as shown in Figure 6.10b.

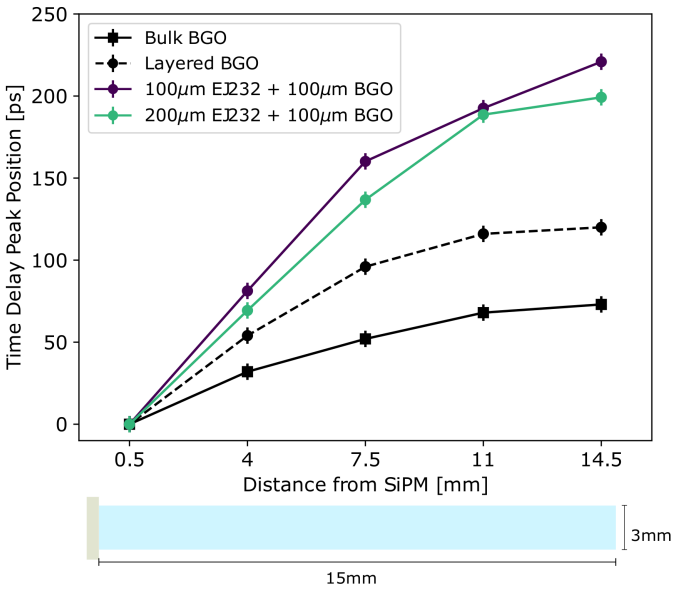

Figure 6.11: Comparison between the shift of the coincidences peak with DOI of the two $3\times3\times15\,\text{mm}^3$ heterostructures measured (considering all the 511 keV events) and of bulk and layered $3\times3\times3\,\text{mm}^3$ BGO. For all the samples the position of the time delay peak of the DOI closest to the SiPM was moved to 0 ps and the other DOIs were properly scaled, to facilitate the comparison. Figure published in [81].

The good agreement between the measured and expected CTR of long pixels confirms that the DOI blurring is one of the main factors related to light transport which contributes to CTR degradation and that Equation 6.3 is a good enough approximation to take into account this effect. The shift of the time delay peak according to the irradiated DOI is therefore a good figure of merit to evaluate the CTR degradation due to DOI uncertainties.

It is interesting to note how the shift of the time delay peak increases when transitioning from bulk to layered BGO and that it becomes even larger when a different material, with different optical properties, is introduced (see Figure 6.11).

This constitutes a further confirmation of the crucial role of light transport for the timing properties, especially when dealing with heterostructured scintillators. Assuming to combine with BGO a scintillating material having the same timing properties of EJ232 but optical properties such that the DOI effect in the heterostructure is the same as in the layered BGO, a CTR of 196 ps – instead of 239 ps – would be achieved with the long 1:1 heterostructure.

From figure 6.11 it can also be noted that the PTS effect due to DOI blurring is greater for the 1:1 than the 1:2 heterostructure. This can be explained by considering that in the former there is a higher number of layers. This means that the better CTR of the 1:2 configuration is not only due to the higher number of fast photons produced but also to better light transport. Indeed, a similar calculation as the one above shows that the difference in CTR between the 1:1 and 1:2 configuration would be smaller (195 ps vs 187 ps respectively instead of 239 ps vs 197 ps) if the shift of the time delay peak of the heterostructure would be the same of layered BGO. Therefore, improving light transport would allow to significantly improve timing while keeping a reasonable sensitivity.

6.3.4 Energy Resolution

The energy resolution is another key parameter to take into account when evaluating the performances of a TOF-PET detector.

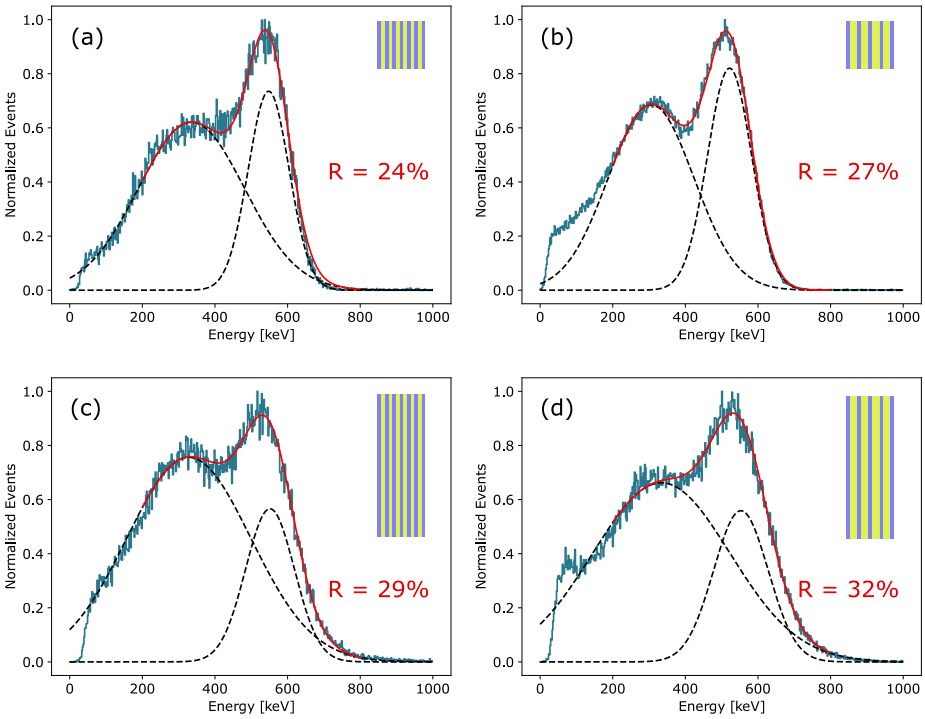

Figure 6.12: Energy spectra of all the heterostructures measured: 1:1 short (a), and 1:2 short (b), 1:1 long (c), and 1:2 long (d). The sum of two Gaussian functions was used to fit the Compton edge and the photopeak. The energy resolution was evaluated as the FWHM of the Gaussian modeling the photopeak.

Figure 6.12 illustrates the energy distribution of the total reconstructed

deposited energy in the four heterostructures that were measured. The Compton part lack of the usual step-shape and there is a significant overlap between Compton and the photopeak. To address this, a combination of two Gaussian functions was used to model the whole spectrum. The energy resolution was thus evaluated as the FWHM of the Gaussian function modeling the photopeak.

Table 6.2: Energy resolution of all the samples measured in head-on configuration: short ($3\times3\times3\,mm^3$) and long ($3\times3\times15\,mm^3$) heterostructure with 100 μm thick plastic plates, with 200 μm thick plastic plates, long bulk and layered BGO.

	100 μm EJ232		200 μm EJ232		bulk BGO	layered BGO
	short	long	short	long	long	long
R [%]	24 ± 2	29 ± 2	27 ± 2	32 ± 3	22 ± 1	30 ± 4

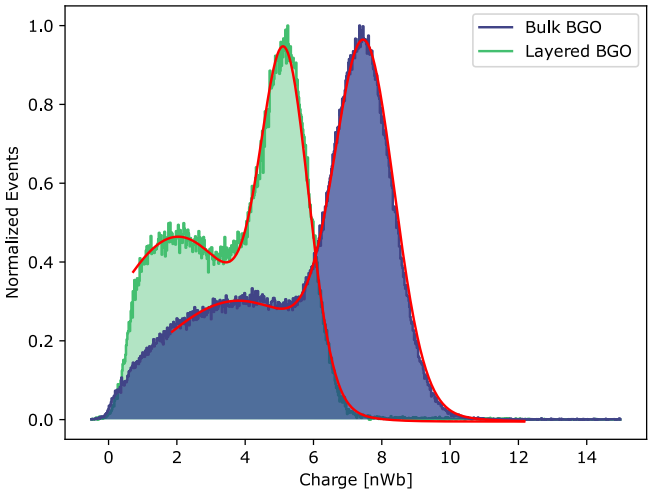

Figure 6.13: Integrated charge distribution of bulk and layered BGO, showing the loss in light output when going from bulk to layered BGO.

In Table 6.2, the energy resolution of the heterostructures is compared to the one of only BGO samples. As expected, the energy resolution worsens for layered structures compared to bulk BGO because of the worse light transport which implies light loss. Comparing the spectra of bulk and layered BGO (Figure 6.13) it can be clearly observed: the photopeak position shifts from 7.4 nWb to 5.2 nWb, i.e. there is a decrease in the number of photons of 30 %. Consistently with this, the degradation is greater for long compared to short pixels. Moreover, structure layering may also contribute to increase the pixel inhomogeneity and further worsen its energy resolution.

The energy resolution of the layered BGO and long heterostructures were found to be comparable. This suggests that the degradation of energy resolution is mainly due to the effect of layering (i.e. worse light transport and increased inhomogeneity) rather than the combination of two different materials, at least for the specific case of BGO and EJ232 which has similar light yield. Events with the same total energy deposited, but distributed differently between BGO and EJ232, will result in approximately the same total number of photons produced and will not significantly affect the energy resolution.

6.4 Summary and Conclusion

In this chapter, the improved CTR of BGO&EJ232 heterostructures compared to only BGO crystal was shown. CTR values (FWHM) of 239 ± 12 ps and 197 ± 10 ps CTR were achieved with the long 1:1 and 1:2 heterostructures respectively. In contrast, bulk and layered BGO exhibited CTR values of 271 ± 14 ps and 303 ± 15 ps, respectively. The inferior CTR performance of layered compared to bulk BGO is due to the worse light transport in such stratified structures. Taking this into account, the CTR improvement of heterostructures is even more significant, demonstrating that the energy-sharing mechanism with a fast scintillator effectively compensates for the degradation introduced by stratification. This results in a CTR improvement of 12 % and 28 % compared to bulk BGO for the 1:1 and 1:2 configurations, respectively, when considering all photopeak events. The CTR improvement becomes even more substantial (21 % and 37 % for the 1:1 and 1:2 configurations, respectively) when considering only the shared photopeak events.

Furthermore, by conducting CTR measurements on the heterostructure investigated in Chapter 6, and applying an analogous events classification to the one used for studying scintillation kinetics, a linear correlation between the CTR and the square root of the effective decay time of the identified event class was established. This approach allowed to experimentally confirm the applicability of the analytical expression for CTR, commonly used for standard bulk scintillators, to heterostructures as well.

By performing DOI collimated measurements, a first understanding and estimation of light transport in heterostructures was provided. The results highlighted that the deterioration of the light transport, resulting in a worsening of the CTR, is intrinsic of such layered structures because of the multiple reflections the optical photons undergo during their path across several layers and surfaces. However, it could be minimized with a proper matching of the optical properties of the material which are combined together.

Preliminary results on energy resolution were also presented. Pixel layering causes a decrease in the light output and, most likely, an increase in inhomogeneity, resulting in a degradation of energy resolution: from 22 % for bulk BGO to about 30 % for both layered BGO and heterostructures 15 mm long.

Collectively, the studies presented in this chapter, along with those in the preceding ones, provide a cohesive understanding of heterostructured scintillators. A simplified proof of concept constituted by two well known materials, BGO and EJ232, was used to investigate the energy sharing mechanism, the scintillation kinetics of heterostructure and main factors affecting the light transport.

The knowledge acquired from these studies will provide valuable support for the design and optimization of the next generation of heterostructured scintillators. The optimization will encompass various aspects, starting from the choice of the most suitable material to replace EJ232, to achieve superior timing and stopping power capabilities. However, before moving to the next generation of heterostructured scintillators, in the next chapter, the CTR of BGO&EJ232 heterostructures scintillator will be further investigated using different readout approaches.

Chapter 7

Enhancing the Coincidence Time Resolution of Heterostructures

7.1 Introduction

The findings presented in the previous chapters highlighted the energy sharing between a heavy and fast scintillator as an effective strategy to improve the time resolution. However, the layering of heterostructured scintillators is a limiting factor for the best achievable time resolution, as it worsens light transport. In Section 6.3.3, we discussed the loss of light collection and uncertainties on the γ-ray's depth of interaction as the key factors affecting this. Reading-out the scintillating light in double-sided configuration allows for simultaneously maximizing the light collection and to retrieve the DOI information, ultimately resulting in better time resolution [114–116].

The implementation of double-sided readout with customised high-frequency electronics for heterostructures is the main focus of this chapter. In Section 7.2.2, the experimental setup and method are described. The results are presented in Section 7.3, focusing first on DOI resolution and then on the comparison between single-ended and double-ended readout. Finally, we switched to a symmetrical configuration, measuring two heterostructured pixels against each other (Section 7.3.4). This configuration was tested in both single- and double-sided readout, and it was repeated using the SiPMs NUV Metal-filled Trenches (MT) (Section 7.3.5) recently developed by Fondazione Bruno Kessler (FBK) and Broadcom [8]. The NUV-MT is an innovative technology that, by minimising internal cross-talk, allows for an unprecedented overvoltage, hence high photon detection efficiency and optimized gain.

7.2 Materials and Method

7.2.1 Samples

The heterostructured scintillators tested until now were hand-assembled in our workshop at CERN, while the ones subject of this study were purchased at Crystal Photonics, Inc (CPI) [117] company. The interest in this technology is also growing outside the walls of universities and research centres: Multiwave Metacrystal [118] and the collaboration they started with CPI for the industrial production of heterostructures are proof of this and represent an important step towards the implementation of this technology also at system level.

Crystal BGO layers of 100 μm proved to be extremely fragile for such fabrication. Therefore, at least for a first test, different thicknesses were chosen compared to those discussed earlier in this thesis: 250 μm both for BGO and EJ232 plates. Moreover, the pixel length was increased from 15 mm to 20 mm, as in most of the PET scanner commercially available [44, 56, 119].

To summarize, two BGO&EJ232 heterostructures $3\times3\times20\,\mathrm{mm}^3$ were used for this study. The $3\times20\,\mathrm{mm}^2$ surfaces of both BGO and EJ232 were polished, while the edges were depolished. The Vikuity ESR reflector was used for wrapping the heterostructure and maximize the light collection.

The heterostructures were coupled with Cargille Meltmount glue (refractive index n=1.58) to Broadcom NUV-HD SiPM with $3\times3\,\mathrm{mm}^3$ active area and 30 μm SPAD size (AFBR-S4N33C013) [120]. The SiPM were biased at about 10 V over voltage (37 V bias voltage), providing a PDE higher than 50 % in the emission region of BGO and EJ232 (360-500 nm) and an intrinsic SPTR of 88±6 ps [5].

7.2.2 Double-ended High-Frequency Readout CTR Bench

The experimental setup closely resembles the one outlined in Section 6.2. The front-end electronics was designed at the Lawrence Berkeley National Laboratory. It is also based on high-frequency circuits (in this case, the RF amplifiers are Minicircuits Mar6-SM+) but it was designed to allow for double-sided readout of the crystal through a single printed circuit board (PCB).

Data acquisition was accomplished using an 8-channel Tektronix MSO68B-400 oscilloscope, exhibiting a sampling rate of 12.5 GS/s and bandwidth of 8 GHz.

Figure 7.1 (top) shows a picture of the experimental setup, with the two heterostructures measured in coincidence in a symmetrical configuration and in double-sided readout.

7.2.3 Method

An heterostructure was initially measured against a reference crystal ($2\times2\times10\,\mathrm{mm}^3$ LSO:Ce:0.2%Ca, 85 ps CTR) first in single-sided readout (SSR) and next in double-sided readout (DSR), with front irradiation.

The measurement in DSR was then repeated in side, collimated irradiation to extract DOI information. To ensure the irradiation of about 2 mm spot along the heterostructure, the ^{22}Na source was placed 12 cm and 1.5 cm far from the reference crystal and the heterostructure, respectively. Eleven DOIs were

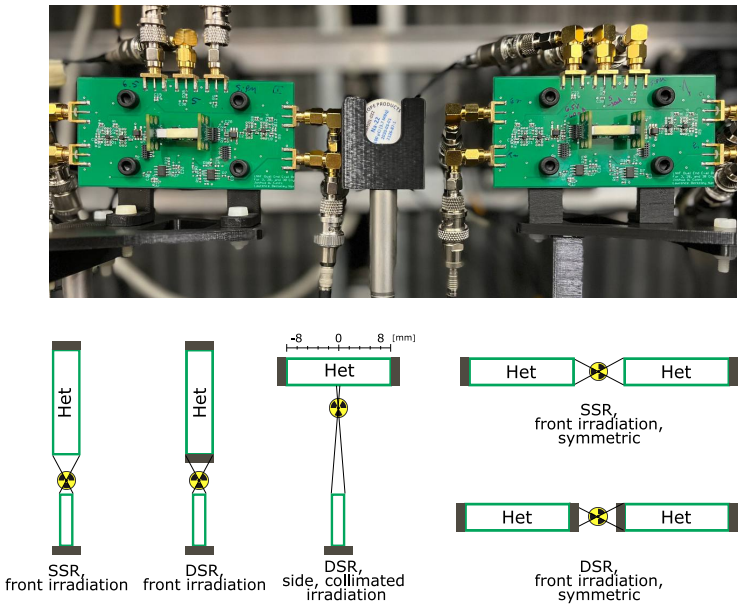

Figure 7.1: Top: picture of the experimental setup. Bottom: scheme of all the configuration tested; from left to right: front irradiation in single side readout (SSR) vs reference crystal, front irradiation in double side readout (DSR) vs reference crystal, side and collimated irradiation in DSR vs reference crystal, SSR of two heterostructures against each other, DSR of two heterostructures against each other.

irradiated to evaluate the DOI resolution of the system and perform the DOI calibration.

The two heterostructures were then measured in coincidence with each other in a symmetrical configuration, both in SSR and DSR. All the configuration tested are summarized in Figure 7.1.

In the DSR measurements, *front side* and *back side* refer to the $3\times3\,\mathrm{mm}^2$ surfaces closest and furthest away from the radioactive source, respectively. The corresponding Silicon Photomultipliers (SiPMs) are referred to as *front SiPM* and *back SiPM*. For consistency, the same nomenclature is kept in the DOI configuration, and in the SSR configuration the readout face is referred to as *back side* and the corresponding SiPM as *back SiPM*.

The data acquisition and data analysis were performed in similar way as described in Section 6.2.3, only extended to the larger number of channels involved (up to 8 in the DSR symmetric configuration).

The time delay (dt) in SSR was recorded as the time difference between the timestamps of the back SiPMs on the two sides, exactly as in Chapter 7. In DSR, when measuring the heterostructure in coincidence with the reference detector, the average between the time delay of the reference with the front and back SiPMs was considered. In DSR symmetrical configuration, the time delay between each side with the back and front side of the opposite detector was recorded, and the average between the four time delays distribution was obtained. Equation 7.1 summarizes all the ways the time delay distribution was obtained for the different configurations, where t_{ref}, t_{back} and t_{front} refers to the timestamps of the reference detector, the back and front SiPM of the heterostructure,

respectively. The subscript 1 and 2 refer to the two heterostructures in the symmetrical configuration.

$$\begin{aligned} dt_{SSR} &= t_{ref} - t_{back} \\ dt_{DSR} &= \frac{(t_{ref} - t_{back}) + (t_{ref} - t_{front})}{2} \\ dt_{SSR,symm} &= t_{back,1} - t_{back,2} \\ dt_{DSR,symm} &= \frac{(t_{back,1} - t_{back,2}) + (t_{front,1} - t_{front,2})}{4} \end{aligned} \tag{7.1}$$

Other possible estimators for timing (i.e., weighted average, covariance combination, corrected for DOI contribution) in DSR were also tested and are discussed in the following sections.

The CTR was obtained directly as the FWHM of the time delay distribution (when measuring in the symmetrical configuration) or as the FWHM corrected for the reference contribution (when measuring against the reference). In both cases, the FWHM was evaluated after applying the time walk correction. For DSR measurements, first the time walk correction was applied on each time delay measurements, then the average between back and front timestamps was evaluated.

7.2.4 NUV-HD Metal-filled Trenches Technology

The SiPM used for the study presented in Chapter 7 and for the main study of this Chapter, as already mentioned, belong to the NUV-HD technology commercialized by Broadcom.

The NUV-HD technology (where NUV stands for near-UV sensitive and HD for high density of cells in the SiPM) was initially developed by FBK [7, 121] for TOF-PET applications to feature high photo-detection efficiency (PDE) in the NUV region, while reducing the correlated noise. This target was achieved by separating the microcells with deep trenches filled with Silicon dioxide. The trenches provides both electrical isolation and partial optical isolation between microcells, because of reflection and diffraction at the trench interface due to different refractive index.

Metal-filled Trenches (MT) technology is an upgrade of NUV-HD and was developed as part of the collaboration between FBK and Broadcom to further suppress internal crosstalk. In this case, the isolation of the microcells is realised using metal-filled trenches. Metal, unlike silicon dioxide, is a reflective material and therefore confines the photons emitted during the avalanche within the fired microcell itself, thus suppressing almost completely the probability of internal crosstalk.

The NUV-MT SiPM were purchased from Broadcom and received at the end of summer 2023. Therefore, the whole study on the transition from SSR to DSR, the DOI resolution, and the transition from the configuration with the reference detector to the symmetrical configuration was performed with the NUV-HD SiPM. Then, the two configurations of greatest interest, i.e. the symmetrics SSR and DSR configurations, were measured again with the NUV-MT SiPM, $3.7 \times 3.6\,\mathrm{mm}^2$ active area and $40\,\mu$m SPAD cell pitch [122]. The low crosstalk probability allowed to use an over voltage up to 15 V (47 V bias voltage).

7.3 Results

7.3.1 Single vs Double-ended Readout

The first advantage of DSR is the increased light collection. As mentioned in Section 6.3.3, in crystals with high aspect ratio, the first photons reaching the SiPM are those emitted along the two longitudinal directions. While in SSR the photons emitted toward the opposite face to the SiPM have high probability to be absorbed, in DSR a large part of these photons is not reflected back but directly detected. Figure 7.2 shows the comparison between the integrated charge in SSR and DSR. The integrated charge collected by the front and back SiPMs individually are also shown.

As the CTR scales as the inverse of the light output squared root, considering the shift of the photopeak in the integrated charge distribution (from 4.06 nWb to 5.77 nWb) we expect a CTR improvement of 15 % due to this effect.

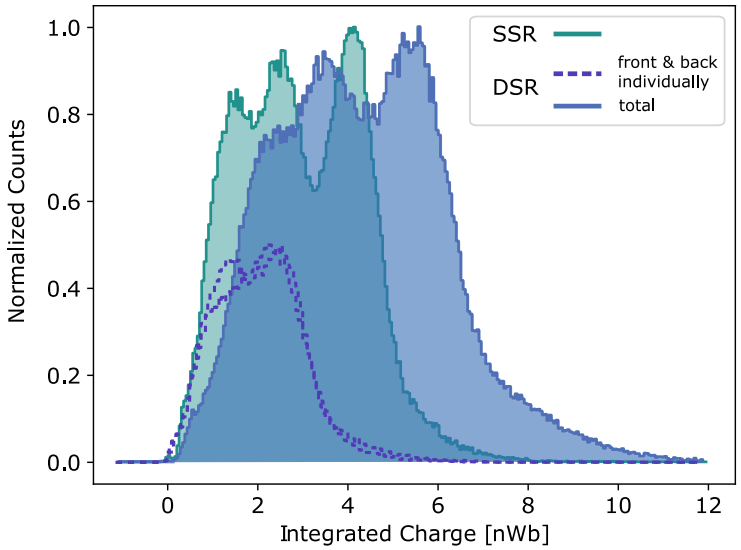

Figure 7.2: Comparison of the integrated charge collected in single-sided reading (SSR) and double-sided reading (DSR). For the DSR configuration, both the integrated charge of the front and back SiPMs individually (dashed lines) and the total one, obtained as the sum of these two (solid line), are shown. The charge distributions of SSR and DSR (total) were normalised with respect to the height of the photopeak. Since the total charge collected in DSR was assessed by summing the charge collected from the front and back SiPMs, the corresponding distributions were normalised to half their height.

The CTR in SSR for all the photopeak events resulted 262 ± 8 ps, while selecting only the shared photopeak events 202 ± 6 ps were measured.

To evaluate the CTR in DSR, different estimators were considered. The first and most obvious one consisted in the simple average between the timestamps of back and front SiPM (dt_{DSR} in Equation 7.1), which led to 174 ± 6 ps and 117 ± 5 ps for all and the only shared photopeak events, respectively.

However, the time resolution of the single channels, i.e. $(t_{ref} - t_{back})$ and $(t_{ref} - t_{front})$, is not the same because of the directionality of the incoming γ-ray and it could contribute differently to the overall time resolution. Therefore, the

weighted average should be also evaluated:

$$dt_{DSR,w} = \frac{t_b/\sigma_b^2 + t_f/\sigma_f^2}{1/\sigma_b^2 + 1/\sigma_f^2}, \tag{7.2}$$

with t_b and t_f being the timestamp of back and front SiPM and σ_b and σ_f the standard deviation of the $(t_{ref} - t_b)$ and $(t_{ref} - t_f)$ distribution. Moreover, the timestamps of back and front SiPMs could be correlated, and in this case the covariance combination (Equation 7.3) should be considered.

The covariant element $(\sigma_{f,b})$ was therefore evaluated according to Equation 7.5 and a correlation coefficient r (Equation 7.6) of 0.006 was found, suggesting that the two variables are not correlated.

$$dt_{DSR,c} = t_b \cdot w_b + t_f \cdot w_f \tag{7.3}$$

$$w_b = \frac{\sigma_f^2 - \sigma_{f,b}}{\sigma_f^2 + \sigma_b^2 - 2\cdot}, \qquad w_f = \frac{\sigma_b^2 - \sigma_{f,b}}{\sigma_f^2 + \sigma_b^2 - 2\cdot} \tag{7.4}$$

$$\sigma_{f,b} = \frac{1}{N} \cdot \sum_i^N (t_{b,i} - \hat{t_b}) \cdot (t_{f,i} - \hat{t_f}) \tag{7.5}$$

$$r = \sigma_{f,b}/(\sigma_f \cdot \sigma_b) \tag{7.6}$$

The weighted average (Equation 7.2) was therefore evaluated, but a negligible difference was measured between σ_b and σ_f (141 ± 3 ps and 145 ± 3 ps, respectively), leading to the same result obtained with the simple average.

Finally, since the greater the number of photons detected, the better the time accuracy, a weighted average was also evaluated based on the charge collected by each SiPM. Again, no further improvement of the CTR over the simple average was obtained, leading us to conclude that this is the best time estimator, unless corrections are made for DOI.

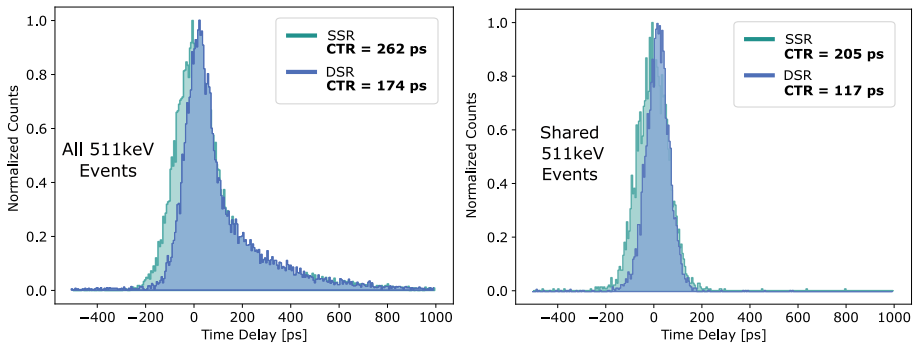

(a) **(b)**

Figure 7.3: Comparison of the time delay distribution in single-sided readout (SSR) and double-sided readout (DSR) for all photopeak events (a) and only shared photopeak events (b).

Figure 7.3 shows the timing improvement when moving from SSR to DSR for all photopeak events (34%) and for only shared photopeak events (42%). The observed improvement exceeded the one predicted considering only the larger

light output in DSR compared to SSR. Moreover, no further improvement was registered by considering the covariance combination of back and front SiPMs (as they resulted uncorrelated) or weighting the timestamps for the charge collected from the corresponding SiPMs. This suggests that the simple average of the timestamps of the back and front SiPMs can compensate for the impact of different DOIs on the timing performance. Interestingly, the improvement is larger when considering only the shared photopeak events.

7.3.2 DOI Resolution

Different estimators for the DOI coordinate were tested: the ratio between the charge collected from the two SiPM (r), the charged collected from one SiPM normalized to the total collected charge (w) [123], and the contrast between the back and front SiPM (c) [114, 124].

$$r = \frac{IntCh_{back}}{IntCh_{front}} \tag{7.7}$$

$$w = \frac{IntCh_{back}}{IntCh_{back} + IntCh_{front}} \tag{7.8}$$

$$c = \frac{IntCh_{back} - IntCh_{front}}{IntCh_{back} + IntCh_{front}} \tag{7.9}$$

Figure 7.4a shows for each DOI the correlation between the integrated charge of front and back SiPMs. For each measured DOI, the variables r, w, and c were evaluated and the correlation with the nominal DOI coordinate was studied. Figure 7.4b and 7.4c show this procedure when the contrast c between back and front SiPM is considered. The average value of c was found to move linearly accordingly to the irradiated DOI:

$$\mathrm{DOI}_{\mathrm{coord}} = m \cdot c + q, \tag{7.10}$$

with m and q being the slope and intercept of the fit curve.

To obtain the DOI resolution, the DOI position was reconstructed for each event using the calibration curve (Figure 7.4c) and the difference from the nominal DOI position in the setup was computed. The FWHM of the resulting distribution (inset in Figure 7.4c) was stated as DOI resolution.

A similar procedure was repeated for the estimator r and w. Table 7.1 summarizes the DOI resolution obtained for each DOI and for all the DOI combined together with the three different estimators, when considering all the photopeak events. While the overall DOI resolution resulted the same independently on the estimator, a larger variance depending on the DOI is observed when using the r estimator:

$$\sigma_r = 1,1 \qquad \sigma_w = 0,5 \qquad \sigma_c = 0,5 \tag{7.11}$$

The estimators w and c gave identical results, with a overall DOI resolution of 6.4 ± 0.04 mm FWHM, almost constant along the 20 mm crystal.

The DOI resolution was then evaluated, using the contrast c as DOI estimator, for only BGO (energy deposited in EJ232 less than 50 keV) and only shared photopeak events (energy deposited in EJ232 more than 50 keV) separately,

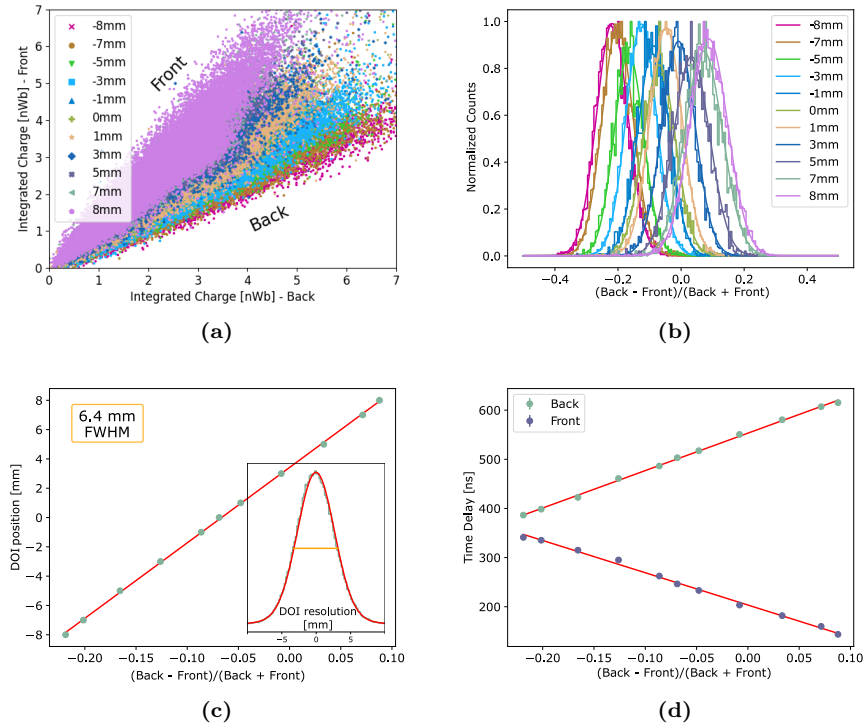

Figure 7.4: DOI calibration. (a) Correlation between the integrated charge collected by the two side according to the DOI. (b) Contrast between the two SiPMs on the opposite sides. (c) DOI calibration curve and DOI resolution. (d) Calibration curve for time correction based on DOI.

Table 7.1: DOI resolution for all photopeak events obtained with three different DOI estimators – the ratio between the integrated charge of back and front SiPM (r), the integrated charge of one SiPM normalized to the total integrated charge (w), and the contrast integrated charge (c) – for each DOI and for all DOIs combined together.

DOI coordinate [mm]	r	w	c
-8	8.6 ± 0.2	6.03 ± 0.04	6.03 ± 0.04
-7	7.9 ± 0.2	5.99 ± 0.04	5.99 ± 0.04
-5	7.1 ± 0.2	5.86 ± 0.04	5.86 ± 0.04
-3	6.6 ± 0.2	6.02 ± 0.04	6.02 ± 0.04
-1	6.1 ± 0.2	6.02 ± 0.04	6.02 ± 0.04
0	6.1 ± 0.2	6.22 ± 0.04	6.22 ± 0.04
1	5.9 ± 0.2	6.39 ± 0.04	6.31 ± 0.04
3	5.5 ± 0.2	6.49 ± 0.04	6.49 ± 0.04
5	5.5 ± 0.2	6.79 ± 0.04	6.79 ± 0.04
7	5.3 ± 0.1	7.05 ± 0.04	7.12 ± 0.04
8	5.4 ± 0.1	7.47 ± 0.04	7.47 ± 0.04
All DOI	6.3 ± 0.2	6.40 ± 0.04	6.40 ± 0.04

resulting in 7.0±0.5 mm and 5.7±0.5 mm. The superior DOI resolution obtained when selecting only events depositing energy also in EJ232 can be attributed to the higher attenuation of EJ232 compared to BGO, because of its partial self-absorption. It is indeed well known that greater asymmetry in the amount of detected photons between the two SiPMs leads to an improved DOI resolution. This is the same reason why with bulk crystals a superior DOI resolution is obtained with deposlished crystals [114, 123, 125, 126].

7.3.3 DOI-based Time Correction

The correlation between the center of the time delay peak with the DOI coordinate estimator was also studied. As it can be observed from Figure 7.4d, the time delay peak moves linearly with the DOI estimator c, in equal but opposite way for the two SiPMs. By consequence, the average time estimator (dt_{DSR}) is nearly constant with the DOI. This explains why the simple average between the timestamp of back and front SiPM yields a significant CTR improvement (from 262 ps to 174 ps for all photopeak events and from 205 ps to 118 ps for the only shared ones) and why by applying a DOI-based time correction [126] no further improvement was obtained (see Table 7.2).

The DOI-based time correction was applied according to the calibration curve obtained from the DOI measurements (Figure 7.4d) to the data acquired in the front irradiation configuration. For each event, the contrast c was computed, and based on this the corrective factors for both the back and front timestamps were evaluated as

$$dt_{corr} = m_t \cdot c + q_t \tag{7.12}$$

with m_t and q_t being the parameters of the corresponding calibration curves in Figure 7.4d. The corrective factors were then subtracted to the measured timestamps and finally the simple average was computed. The FWHM of the resulting distribution was evaluated and corrected for the reference contribution, leading to the results in Table 7.2.

Table 7.2: CTR results in single-sided readout (SSR) and double-sided readout (DSR) considering all and only shared phototpeak events. The results in DSR after applying the correction for DOI are also reported (DSR + DOI corr).

Events type	SSR [ps]	DSR [ps]	DSR + DOI corr [ps]
All Photopeak	262±8	174±6	174±6
Shared Photopeak	205±6	118±5	123±5

The last aspect to consider before concluding that the simple average is the best estimator for timing was the resolution of the single timestamp (back and front) as a function of the DOI.

As before, the contrast c was evaluated on event-basis, and the events were classified in eight intervals according to c. For each interval, the time delay distributions $t_{ref} - t_{front}$ and $t_{ref} - t_{back}$ were considered and the peak position and FWHM were computed. The results of this procedure are illustrated in Figure 7.5. Despite some fluctuation of the FWHM of the time delay distribution of the back and front SiPM, no clear trend was observed with the DOI coordinate (Figure 7.5 (c), (g)). In Figure 7.5 (d), (h), the peak position and corresponding

FWHM of the eight intervals identified are superimposed onto the 2D histogram correlating the time delay with the DOI coordinate (contrast). This visualization further highlights the independence of the single timestamp resolution on the DOI, showing that the width of the distribution remains relatively consistent across the dataset.

All these considerations lead us to conclude that the resolution of both front and back timestamps is largely unaffected by DOI, confirming that the initial approach of using a simple average as the timing estimator is the optimal choice.

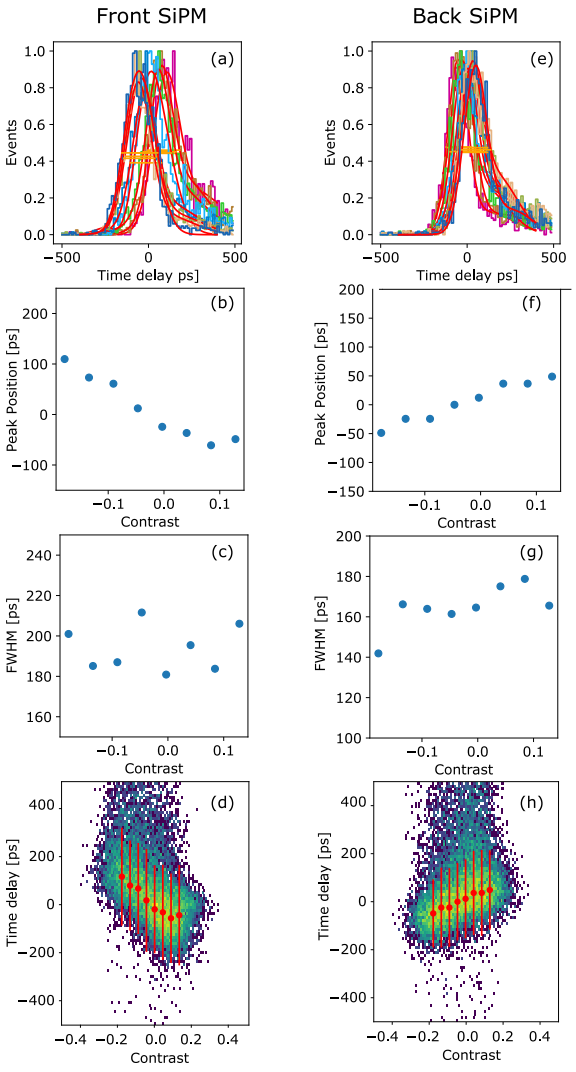

Figure 7.5: Single timestamp (front and back) resolution as a function of DOI. The left column refer to the front SiPM, while the right column to the back SiPM: (a,e) time delay distribution for different DOI coordinate (contrast c); (b,f) peak position of the time delay distribution; (c,g) FWHM of the time delay distribution; (d,h) 2D histogram showing the correlation between the time delay and the contrast. The peak position and FWHM previously obtained are also shown.

7.3.4 Symmetric Configuration

Until now, heterostructured pixels were only measured in coincidence with a (fast) reference crystal. This configuration is widely used to reduce systematics and accurately characterize the sample under investigation. However, it does not always provide an accurate prediction of the actual timing performance of the detector of interest. The main reason for this lies in the method used to correct the contribution of the reference detector. By using quadratic subtraction and multiplying by $\sqrt{2}$, we assume to extrapolate the CTR for two identical detectors. This assumption is no longer valid in the case of detectors with materials showing different light emission processes characterized by strongly different timescales.

An example is BGO, which primarily emits light through slow scintillation but also has a relatively high Cherenkov yield. On average, 15-20 detectable Cherenkov photons (wavelength above 300 nm) are emitted per 511 keV γ-ray photoelectric interaction [5, 13], but large fluctuations on this number are expected. When two coincident BGO crystals are measured, various events can occur [110,127]. Classifying the events as *slow* if no Cherenkov photon is detected and *fast* if at least one Cherenkov photon is detected, the possibilities include: slow events on both detector arms, fast events on both arms or a combination of slow and fast events on opposite sides of the detector. Moreover, different numbers of detected Cherenkov photons give rise to different CTR distributions. The information about the potential combinations of events between the arms of the two detectors is lost when measuring against a reference crystal and performing such correction.

The case of heterostructure is comparable because it may involve shared events on both sides, only on one side, or none at all. Moreover, the timing of shared events depends on the amount of energy deposited in plastic.

The CTR was first evaluated for all the photopeak events and the only shared ones, as previously done (see Figure 7.6). When no events selection is performed (i.e., when taking all the photopeak events), the measured CTR in symmetric configuration is significantly worse than the one extrapolated from the measurement against a reference crystal and assuming two identical detectors: from 262 ± 8 ps to 313 ± 9 ps in SSR and from 174 ± 6 ps to 254 ± 8 ps in DSR. The worsening is absent (SSR) or smaller (DSR) when only the shared photopeak events are selected on both arms. The CTR values obtained in SSR and DSR measuring against reference detector and in symmetric configuration, distinguishing between all and only shared photopeak, are summarized in Table 7.3.

Table 7.3: Comparison of CTR results in single- and double-sided readout (SSR and DSR, respectively) when measuring against a reference detector or in a symmetrical configuration.

Events type	SSR (vs ref.) [ps]	SSR (symm.) [ps]	DSR (vs ref.) [ps]	DSR (symm.) [ps]
All Photopeak	262±8	313±9	174±6	254±8
Shared Photopeak	205±6	195±6	118±5	138±5

To gain a better understanding of the CTR distribution in heterostructures, the photopeak events were classified according to the energy deposited in EJ232. Three interval were selected in both detectors – 0-50 keV (*slow*), 50-250 keV

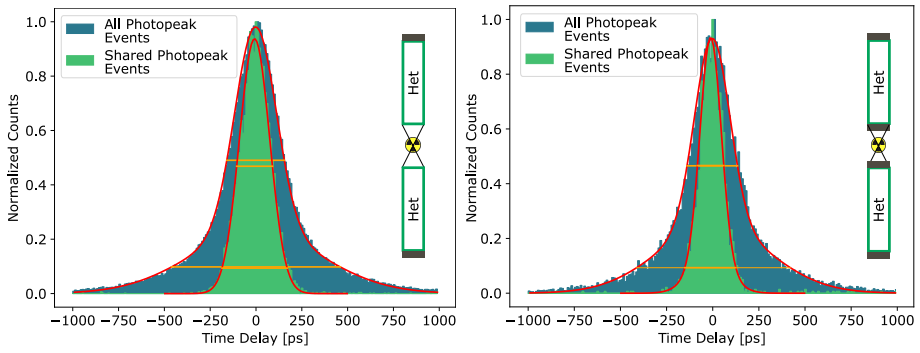

(a) **(b)**

Figure 7.6: Comparison of the time delay distribution in single-sided readout (a) and double-sided readout (b) for all photopeak events and only shared photopeak events, in symmetrical configuration.

(*middle*), and 250-500 keV (*fast*) energy deposited in EJ232 – and all the potential combinations were considered.

Figure 7.7 shows the time delay distribution when slow (Figure 7.7a) and fast (Figure 7.7b) events in one detector occur simultaneously to slow (light blue), middle (blue), and fast (purple) in the opposite detector. Because of the pronounce asymmetry of the distribution when slow events are involved, also the FWTM of the peak was considered.

In SSR, the CTR (FWHM) of all photopeak events is 313 ± 9 ps and 195 ± 6 ps for the only shared photopeak events (corresponding to the 40 % of the all photopeak events). When considering only the BGO photopeak events on both detector arms, the CTR increases up to 394 ± 11 ps, while if we select only the fastest events (i.e., the fast-fast combination, corresponding to only to the 1 % of the photopeak events) it improves up to 181 ± 6 ps.

Repeating the same exercise for the DSR configuration, 254 ± 8 ps CTR (FWHM) was measured for all photopeak events and 138 ± 5 ps for the only shared photopeak events (50 % of the all photopeak events). In the two extreme cases, a CTR of 386 ± 11 ps was measured for only BGO photpeak events of both sides and of 107 ± 5 ps the fastest 1 % of the events.

Figure 7.8 (SSR) and 7.9 (DSR) summarize the CTR measured evaluated as FWHM (left) and FWTM (right) for all the potential combinations considered.

7.3.5 Symmetrical Configuration with MT-FBK SiPM

Table 7.4 summarizes the CTR results obtained when measuring two heterostructures in coincidence in SSR and DSR, each configuration tested both with NUV-HD SiPM and NUV-MT SiPM. As before, the CTR was evaluated both for all and only shared photopeak events.

The CTR improvement in SSR is remarkable especially when considering all photopeak events, hence when there is an important contribution from BGO. From 313±9 ps (NUV-HD) to 270±8 ps (NUV-MT), thus 14 % improvement.

The largest improvement for all photopeak events compared to only shared photopeak event is attributed to the smaller signal of BGO than EJ232 which benefits more from the greater gain achievable with the MT SiPM. This increased

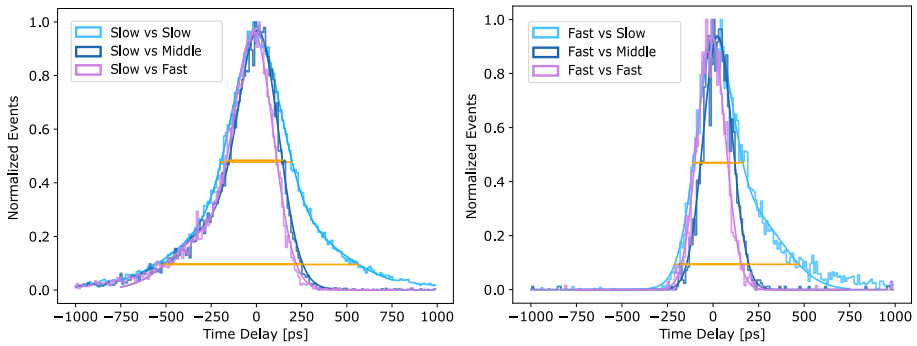

(a) **(b)**

Figure 7.7: Example of time delay distribution when slow (a) and fast (b) events in one detector's arm occur simultaneously to slow (light blue), middle (blue), and fast (purple) in the opposite detector.

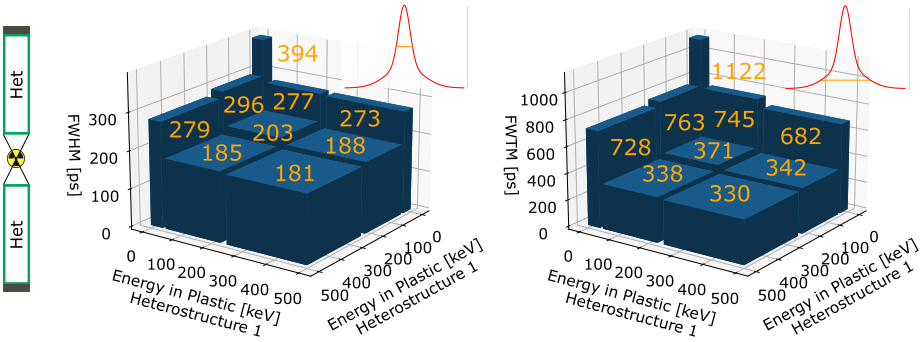

Figure 7.8: Measured CTR in SSR with NUV-HD SiPM for all the potential combination of slow/middle/fast events considered. The CTR was evaluated both as FWHM (left) and FWTM (right).

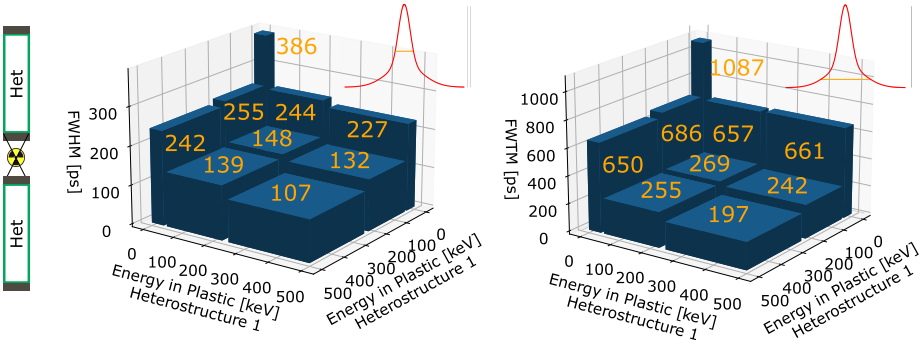

Figure 7.9: Measured CTR in DSR with NUV-HD SiPM for all the potential combination of slow/middle/fast events considered. The CTR was evaluated both as FWHM (left) and FWTM (right).

gain is made possible by the higher over-voltage that can be applied as a consequence to lower crosstalk suppression.

Surprisingly, a minor improvement is observed in DSR when switching from

Table 7.4: CTR results in SSR and DSR comparing Broadcom SiPM belonging to NUV-HD and NUV-MT technology.

	CTR [ps] SSR		CTR [ps] DSR	
Events type	NUV-HD	NUV-MT	NUV-HD	NUV-MT
All Photopeak	313±9	270±8	254±8	239±8
Shared Photopeak	195±6	181±6	138±5	136±5

NUV-HD to NUV-MT technology. This effect is attributed to the fact that the improvement achievable with the MT SiPM is given by larger gain and PDE they offer. In the case of the DSR, this gain is already inherent in the configuration of the DSR itself. This hypothesis is further supported by the CTR values measured in SSR with the MT SiPM approaching those obtained in DSR with the NUV-HD SiPM, suggesting that a performance limit of the considered pixel may have been reached.

7.4 Summary and Conclusion

Having gained a comprehensive understanding of heterostructured scintillators and evaluated their potential as a solution to the trade-off between sensitivity and fast timing in TOF-PET, this chapter focused on further improving the timing performance of these scintillators.

Measurements were performed on a $3\times3\times20\,\mathrm{mm}^3$ BGO&EJ232 heterostructure using both single-sided (SSR) and double-sided (DSR) readout configurations. In DSR, a remarkable improvement, up to 42%, in CTR was achieved when considering only shared events. While part of this improvement can be attributed to increased light collection in DSR compared to SSR (estimated to be around 15% based on the photopeak shift in the integrated charge distributions), the greater enhancement comes from the inherent compensation for the DOI uncertainty through the averaging of back and front SiPM timestamps. The study of correlation between the charge collected from the two SiPMs enabled the estimation of a DOI resolution of $6.40\pm0.04\,\mathrm{mm}$.

CTR values down to $174\pm6\,\mathrm{ps}$ (all photopeak events) and $118\pm5\,\mathrm{ps}$ (shared photopeak events) were measured for $3\times3\times20\,\mathrm{mm}^3$ BGO&EJ232 heterostructure in DSR.

Although DSR may not be an affordable solution at system level, this study provides valuable insights into the performance of pixel heterostructures within a DOI matrix [126]. In that case, a crystals matrix is readout from a single side with a SiPMs array, but by coupling a light guide to the opposite side, the scintillation light emitted in the opposite side of the SiPM is redirected toward to all the crystals of the matrix. The correlation between the charge collected from the SiPM coupled to the crystal where the interaction occurred and its neighbours enable to retrieve the DOI information.

Finally, two heterostructures were measured in coincidence with each other in a symmetrical configuration. This approach allowed for a more accurate assessment of the timing performance of heterostructures, as the correction for the contribution of a reference crystal, assumed to measure two identical detectors, is no longer valid for materials (or combination of materials) having more than one light-emitting process with highly different timescales. The reason

is that the occurrence of the process with same timescales on both detectors, or of the two processes with different timescales on the two detectors, gives rise to different CTR distributions which are not taken into account when correcting for the reference contribution.

To conclude, the measurements in symmetrical (both in SSR and DSR) configuration were repeated using an upgraded SiPM technology, the NUV-MT SiPM from Broadcom developed within the collaboration with FBK. The results showed a significant CTR improvement when transition from the NUV-HD to the NUV-MT technology in SSR (From 313±9 ps to 270±8 ps for all photopeak events and from 195±6 ps to 181±6 ps for only shared photopeak events), while a minor improvement was observed in DSR configuration, where compatible CTR were obtained using the NUV-HD and NUV-MT technology. This led us to conclude that a performance limit of the considered heterostructured pixel may have been reached.

Part IV

Next Generation of Heterostructured Scintillators

Overview

In the previous part of this thesis, the concept of heterostructure was introduced, and the fundamental properties and potential of this technology have been thoroughly investigated using a simplified proof of concept consisting of alternating layers of BGO and EJ232 plastic scintillator.

Despite EJ232 exhibiting much faster decay kinetics compared to standard inorganic scintillators (except for BaF_2 whose sub-nanosecond emission has, however, low light yield and is in the VUV [17, 18]), it is neither fast nor dense enough for the heterostructure to achieve the desired time resolution and exceed the limits set by the current state of the art, L(Y)SO.

Nanoscintillating materials were introduced in Section 2.3.4. Because of quantum confinement, they can exhibit ultra-fast scintillation kinetics and high intrinsic light yield. They usually are inorganic crystals and can potentially have higher density than plastic. However, they are often embedded in polymer matrices and produced in small size, thus the low stopping power still represents a limitation.

Overall nanoscintillators represent a valid alternative to plastic scintillators for heterostructures, and within the Crystal Clear Collaboration, several groups from different universities are working on the fabrication and optimization of these materials.

In the next chapters, the experimental setup and method developed for the characterization of these materials are presented together with the study conducted on lead halide perovskite ($CsPbBr_3$) in collaboration with the Czech Technical University (CTU) in Prague. Specifically:

- Chapter 8 presents the experimental setup based on X-ray excitation which was developed to measure the time resolution and light output of low-stopping power materials. The setup and method were validated using standard bulk organic and inorganic scintillators and afterward tested also with nanoscintillators.

- Chapter 9 focuses on the characterization of $CsPbBr_3$, both in the form of free nanocrystals and nanocomposite embedded in polystyrene. A proof of concept of heterostructure with GAGG and $CsPbBr_3$ is also presented. Furthermore, the experimental setup described in Chapter 8 allowed us to show the potential of $CsPbBr_3$ thin film applied on bulk heavy scintillator for TOF-Xray application.

The findings of these studies have already been published or are under consideration for publication [89, 96, 97].

Chapter 8

Time Resolution and Light Output Measurements upon X-ray irradiation

8.1 Introduction

In Section 2.3.4, the properties of nanocrystals and nanoscintillators were introduced. The growing interest in these materials is due to quantum confinement effects, which result in higher light output and faster scintillation kinetics compared to their bulk counterparts.

One of the primary drawbacks of these materials is their low stopping power, which not only prevents their use as stand-alone detectors, but also limits the possibility of characterising them in terms of time resolution and light yield using standard techniques, as they usually employ γ-ray radiation.

Time resolution measurements require a reference detector, and, with radioactive sources, this is only feasible with β^+ sources, emitting two 511 keV γ-ray in coincidence following the positron annihilation. However, this restricts the investigation of timing at lower energy. Standard light yield measurements usually use ^{137}Cs, due to its single emission at 662 keV. Lower energy radiation sources, such as ^{55}Fe with its primary emission around 6 keV, are more suitable for nanomaterials' stopping power. However, at this energy range, the background contribution is more important and complicates the spectrum interpretation. While a coincidence system can effectively reject background, this is not possible with low-energy radioactive sources.

To address these limitations, an experimental setup was developed to simultaneously measure the detector time resolution (DTR) and light output (LO) of low stopping power materials using soft (0–40 keV) pulsed X-rays and SiPM as a photodetector.

In this chapter, the validation of the experimental setup and of the proposed approach are presented along with a first application to two nanomaterials. The validation was performed measuring well-known bulk scintillators and it was based on the confirmation of the inverse proportionality relationship between the time resolution and the square root of photon time density. Section 8.2.1 summarizes

all the samples used. Section 8.2.2 and Section 8.2.3 describe, respectiveley, the already established experimental setup used to measure the scintillation kinetics (*X-ray TCSPC bench*) and the newly developed experimental setup (*X-ray DTR and LO bench*). In Section 8.3, the method and the data analysis are thoroughly discussed, and the results are presented in Section 8.4. Finally, Section 8.4.4 explores the potential of this experimental setup with nanoscinitllators.

8.2 Materials and Experimental Setup

8.2.1 Samples

The bulk, standard scintillators used for this study were LSO:Ce:0.2%Ca, LYSO:Ce, BGO (inorganic scintillators) BC422, EJ232 and EJ232Q 0.5% quenched (organic scintillators). The latter three allowed to have an insight of the performances of low-density (1.023 g/cm^3 [82,86]) scintillators with ultra-fast rise- and decay time (about 35 ps rise-time and 1-2 ns effective decay time [5]). All the samples were fully polished with a geometry of 3×3×3 mm^3. An overview of these scintillators and their properties is presented in Table 8.1.

Table 8.1: Overview of the standard scintillators used for the validation of the experimental setup, all with size 3x3x3 mm^3.

Sample	Producer	Density [g/cm^3]	Emission peak [nm]	Light Yield [ph/keV]
LSO:Ce:0.2%Ca	Agile	7.4	420	39.2[1]
LYSO:Ce	CPI	7.1	420	41.1[1]
BGO	Epic Crystal	7.1	480	10.7[1]
BC422	Saint-Gobain	1.023	370	10.1[1]
EJ232	Eljen Technology	1.023	370	8.4[2]
EJ232Q 0.5%	Eljen Technology	1.023	370	2.9[2]

[1] Values published in [5]
[2] Eljen Technology datasheet [86]

Two nanomaterial samples were also measured as a proof-of-concept. Lead halide perovskite ($CsPbBr_3$) nanocrystal embedded in polystyrene [96], with a weighted filling factor of 10 % and overall size of 3×3×0.1 mm^3. Multi quantum well (MQW) InGaN/GaN [128] grown on a sapphire substrate of thickness 500 μm with 1 μm thick active layer and cross section of 3×3 mm^2. The former sample was produced at the Czech Technical University (CTU) in Prague, while the latter at the Institute of Physics of the Czech Academy of Science (FZU) in Prague, Czech Republic.

From now on, for the sake of synthesis, LSO:Ce:0.2%Ca, LYSO:Ce, InGaN/GaN, and $CsPbBr_3$ are referred to as LSO, LYSO, InGaN, and CPB respectively.

8.2.2 X-ray Time Correlated Single Photon Counting bench

The decay time of the aforementioned samples was measured in TCSPC mode [102], following pulsed X-ray excitation. To perform these measurements, we utilized the experimental setup depicted in Figure 8.1 (top). It consists of a

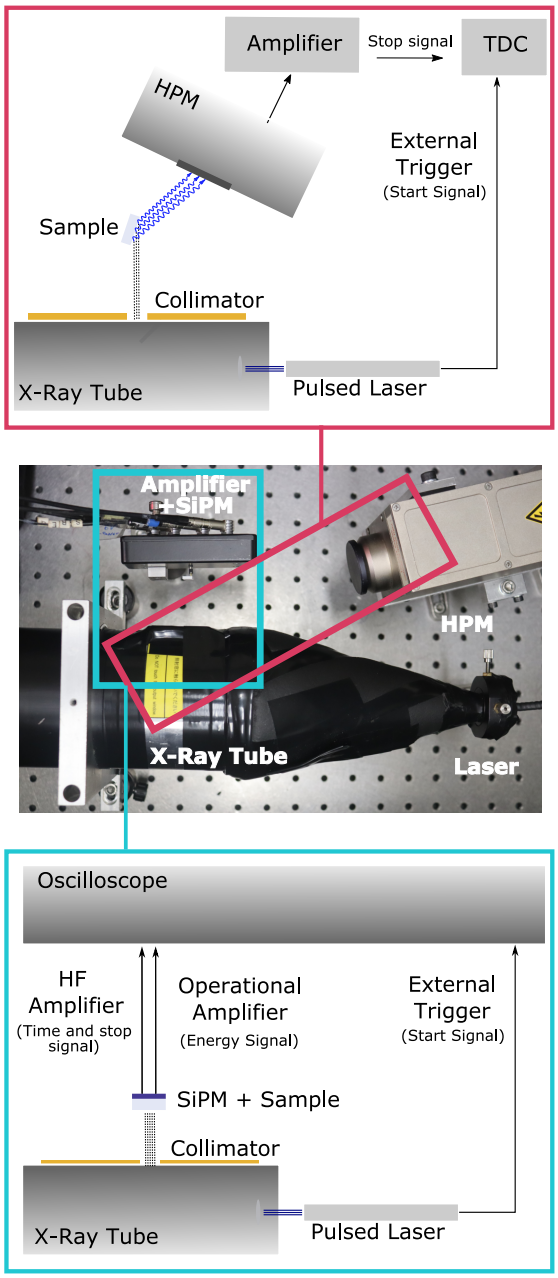

Figure 8.1: Schematic drawing of the TCSPC X-ray bench for rise and decay time measurements (top) and of the X-ray detector time resolution and light output bench (bottom). A picture of the two coexisting setups is also shown (center). Figure adapted from [97].

pulsed diode laser (PDL 800-B from PicoQuant) with 40 ps pulse width (FWHM), which acts as excitation source of a tungsten X-ray tube (XRT N5084 from Hamamatsu) operating at 40 kV. The energy spectrum of the produced X-rays extends from 0 to 40 keV, with a pronounced peak around 9 keV due to Tungsten L-characteristic X-rays and a mean energy of about 15 keV.

A brass collimator is placed in front of the XRT window to focus the irradiation on the samples only. The scintillation light is collected in TCSPC by a hybrid photomultiplier tube (HPM 100-07 from Becker&Hickl), whose signal is fed into an amplifier and timing discriminator (model 9327 from ORTEC). Finally, the output of the amplifier gives the stop signal to the time-to-digital converter (xTDC4 from cronologic), while the start is provided by the external trigger of the same pulsed laser which triggers the X-ray production.

The overall impulse response function (IRF) of the system is shown in Figure 8.2. It was obtained as the analytical convolution between the measured IRF of the laser together with HPM and the previously studied IRF of the X-ray tube [129], resulting in about 160 ps FWHM.

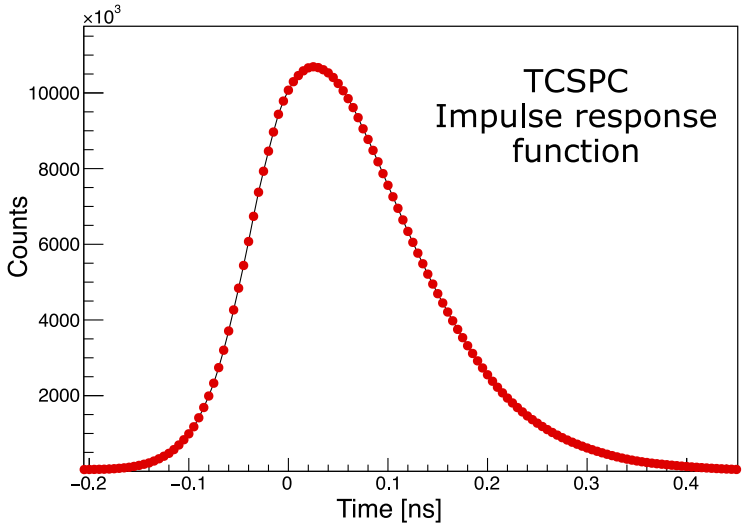

Figure 8.2: Impulse response funcion (IRF) of the TCSPC setup.

8.2.3 X-ray Detector Time Resolution and Light Output bench

Part of the newly developed setup shares components with the one described earlier. Figure 8.1 (center) provides a picture of the whole setup. The excitation branch is indeed constituted by the PDL 800-B laser (whose external trigger constitutes the reference of the coincidence system and gives the start for the timing measurement) and the X-ray tube.

The key distinction from the previous setup is the detection chain, which allows to measure simultaneously the time resolution and the light output. It consists of a SiPM (S13360-3050CS from Hamamatsu, 53 V breakdown voltage, 61 V bias voltage) and a front-end readout based on high-frequency (HF) electronics circuit [9, 108]. This readout electronics has already been described in Section 6.2, here we just remind that the SiPM signal is split into two channels for optimizing both energy and time information. The amplified signals are digitized by an oscilloscope (Lecroy, WaveRunner 8104) with a sample rate of 20 Gs/s and a bandwidth of 1 GHz, where all the necessary analysis information is extracted directly from the waveforms.

As mentioned in Section 6.2, the time resolution was evaluated as the FWHM of the time delay distribution between the start and stop signal. Additionally, the integrated charge of the energy signal was used to obtain the energy spectrum and estimate the light output. This setup closely resembles a classical coincidence time resolution setup, with the laser trigger replacing one detector arm and lower excitation energy.

To maximize the light collection, the samples were directly coupled to the SiPM through Meltmount glue (refractive index $n = 1.582$, transmission cutoff at about 300 nm). Given the low energy of X-rays, the likelihood of X-ray absorption from any material between the tube and the sample is not negligible. Therefore, no reflective material was used. This inevitably affected the light collection and needs to be taken into account for the evaluation of the intrinsic light yield (ILY).

8.3 Method

8.3.1 Scintillation kinetics

The decay time constants were obtained by the fit of the scintillation pulse with the convolution between the IRF of the system and the intrinsic scintillation rate. For the latter, the sum of bi-exponential (Equation 5.1) was used.

Being the IRF of the TCSPC setup of about 160 ps FWHM, for most of the measured samples the rise time was comparable to or below the accuracy of our system. Only for LSO and LYSO the fit was performed letting free all the parameters. In contrast, for all other standard scintillators, during the fit procedure the rise time was constrained to values obtained in previous work [5] (generally between 0-20 ps). This constraint was applied to enhance the stability of the decay part of the pulse, which is of greater interest for this study. Additionally, the two nano-scintillators exhibited rise times that could not be resolved with the IRF of the system, and as it was found not to improve the quality of the fit, it was fixed to 0 ps. Hence, similar to the previous study on scintillation kinetics of heterostructures (see Chapter 6), the analysis primarily focused on the decay kinetics.

All samples exhibited at least two decay time components, and the effective decay time (Equation 5.7) was used as figure of merit for the decay time.

It should be emphasised that the sum of bi-exponential functions is a well-established model for standard bulk scintillators, but it might not be optimal for nanoscintillators [130]. Nevertheless, the primary objective of this study was not to provide a physical interpretation of the individual components but to identify an appropriate figure of merit for describing the impact of decay kinetics on time resolution and allowing the comparison of different samples. Once the pulse is accurately described by a sum of exponential functions, the effective decay time serves as a suitable figure of merit.

The potential number of decay components that can be used is theoretically unlimited, and as the number of components increases, the quality of the fit improves but at the cost of losing physical significance of individual components. The fitting process for the two nanomaterials was therefore performed multiple times, changing the number of decay components from two to five. The optimal choice was determined by selecting the function with the minimum number of

decay components that yielded a good and stable $\tilde{\chi}^2$ value.

A different approach to model the scintillation kinetics of nanoscintillators is discussed in Chapter 9, focused on the characterization of lead halide perovskite.

8.3.2 Mean Collected Charge and Light Output

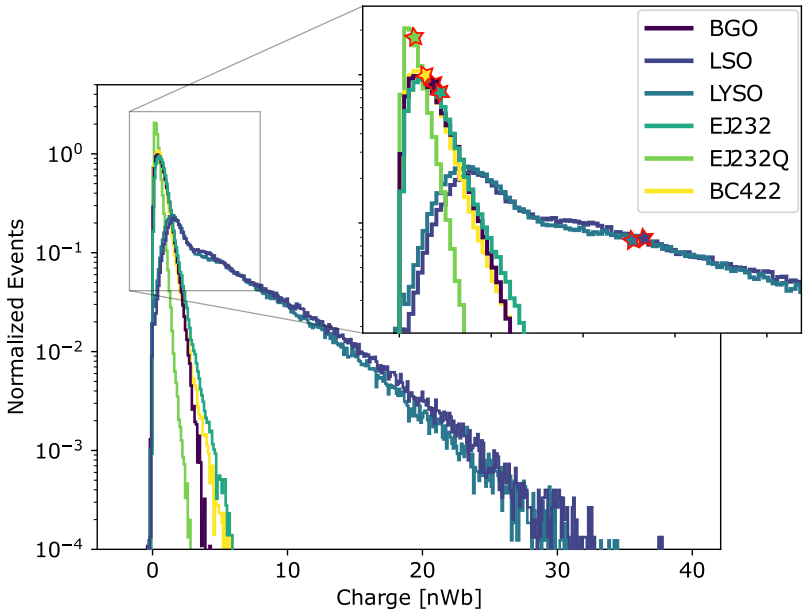

Figure 8.3: Integrated charge distribution of all the measured standard scintillators. The red outlined stars (filled with the colours of the corresponding distribution) represents the mean collected charge. Figure published in [97].

While the energy spectrum of a radioactive γ-ray source is discrete, that of an X-ray tube comprises a continuous spectrum overlaid with discrete lines due to the characteristic X-ray emissions from the target material. The XRT N5084 by Hamamatsu has a tungsten target and operates at 40 kV, therefore only the L characteristic X-ray at 8.4 keV and 9.7 keV are produced [131, 132]. Because of the low energy, the corresponding peak can be identified only for materials with high light output and good energy resolution (i.e., LSO and LYSO). In any case, being the two energies so close, they result in only one peak (see Figure 8.3).

To ensure a consistent approach across all samples and accommodate various materials, the mean collected charge (i.e. the mean of the charge distribution, labelled with red stars in Figure 8.3) was chosen as figure of merit for the light output.

It is worth mentioning that other figures of merit can be equally valid, such as the peak at 9-10 keV if well identifiable, or the end-point of the distribution which for standard scintillators corresponds to the maximum energy of X-rays, i.e. 40 keV. However, these are not as versatile as the mean collected charge because not for all samples the 9-10 keV peak can be identified (due to low stopping power as for nanomaterials or too low photon time density as for BGO). Additionally, for nanomaterials, determining the maximum energy deposited and

subsequently converted into scintillating photons can be non-trivial. While for the characterization of a specific material the most suitable figure of merit for it should be adopted, in this case it was decided to use a common one for all the sample, for a simpler and direct comparison, hence the mean collected charge.

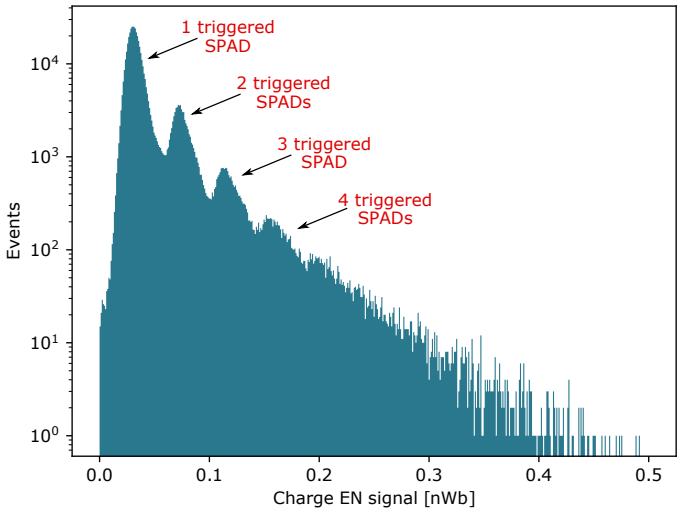

Figure 8.4: Finger plot of the energy (EN) channel obtained from a dark count measurement of S13360-3050CS Hamamatsu SiPM at 61 V bias voltage (53 V breakdown voltage). Figure published in [97].

Once the figure of merit has been chosen, the light output can be extracted. This requires knowledge of the corresponding deposited energy and the charge values attributed to only one triggered SPAD. To determine these values, a single photoelectron measurement was performed by removing the sample from the SiPM and turning off the X-ray tube. In this configuration, only signals from dark counts, i.e., thermal electrons generated within the active volume, initiating an avalanche in a SPAD, were detectable. Each dark count triggers therefore only one SPAD, and it is quite unlikely that two dark counts occur simultaneously. Therefore, signals generated by two or more triggered SPADs result from cross-talk, where one avalanching SPAD triggers another one. If the gain is high enough, the discrete nature of the SiPM output can be observed and the signals generated by a different number of triggered SPAD can be distinguished. In such cases, integrating the signal yields a distribution like the one shown in Figure 8.4. Such distribution is generally referred to as *finger plot*.

To determine the charge corresponding to single photoelectron signals, the average distance between two adjacent peaks was evaluated. This approach is preferable to relying solely on the position of the first peak, particularly when the pedestal is not well-aligned to zero. Additionally, calculating the average reduces systematic errors. A calibration factor of 0.05 ± 0.01 nWb was obtained.

This measurement also allowed to evaluate the cross-talk probability and the corrective factor, following the method explained by [15, 133], needed to evaluate the actual light output or light yield of a given material (Section 8.4.3).

8.3.3 Detector Time Resolution

The DTR was evaluated as the FWHM of the time delay distribution, taking all the events without any energy-based selection. This approach allowed a consistent correlation between the calculated DTR and the estimated light output, which was determined as the mean collected charge.

The time delay between the SiPM signal and the laser trigger was measured via leading edge time pick-off method. Since this method is inherently susceptible to time-walk effects, a correction was implemented using the SiPM signal rise-time [110], as described in Section 6.2.3.

Following this correction, the time delay distribution was analyzed by fitting it with a convolution of Gaussian and exponential functions. This convolution was used to account for the distribution asymmetry. The DTR value was then evaluated as the FWHM of the fitted function. Figure 8.5 shows the time delay distribution with its fit for both a standard bulk scintillator (LSO) and a nanoscintillator sample (InGaN).

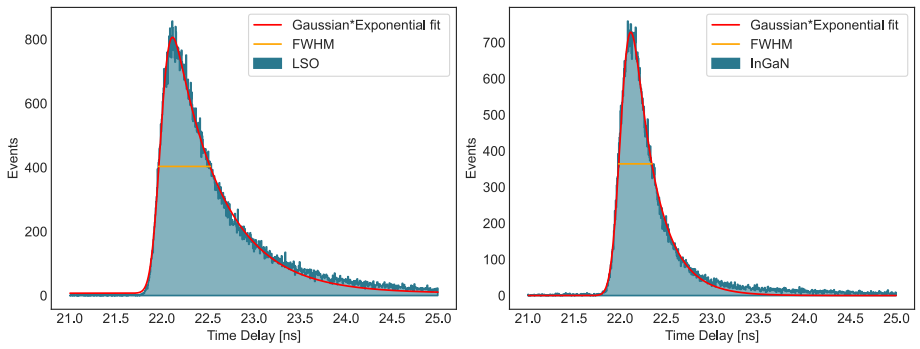

(a) **(b)**

Figure 8.5: Fit of the time delay distribution of LSO (a) and InGaN (b) using the convolution between Gaussian and exponential functions to extrapolate the FWHM. Figure published in [97].

8.4 Results

8.4.1 Decay time, Detector Time Resolution, Light Output

The decay time components resulting from the bi-exponential fit of the scintillation time profiles are summarized in Table 8.2. In the last column also the effective decay time for each sample is reported. It should be noticed that, in the weighted harmonic mean, more importance is given to the fastest component instead of the component with the highest abundance (as opposed to the standard weighted mean). This is intrinsic to its mathematical definition (Equation 5.7) and it explains why, for instance, the effective decay time of BGO is only 129±10 ns though the main component (contributing to 92%) is 318±22 ns. However, when examining the individual components, the results align with those previously published in the literature [5, 107].

In Figure 8.6, the time delay distributions of all standard scintillators measured are shown. The DTR values are summarized in Table 8.3, together with

the effective decay time and light output.

The light output is stated as the mean collected charge to prevent introducing uncertainties associated with imprecise estimations of deposited energy. For the validation of the setup, it was therefore chosen not to evaluate the light output as number of detected photons. An in-depth analysis of LSO is provided in Section 8.4.3, including the evaluation of its light output and intrinsic light yield, to confirm the capabilities of this setup.

A correlation between DTR and effective decay time is evident: in general, the faster the decay time, the better the time resolution. However, this relation is not absolute, as the light output plays a crucial role too. For instance, EJ232Q has an effective decay time in the sub-nanosecond range, almost three times faster than the EJ232 and BC422, but its temporal resolution performance does not surpass that of the latter two scintillators. This discrepancy is due to the lower light output of the EJ232Q compared to the other two plastic scintillators.

Table 8.2: Summary table with decay time components resulting from the bi-exponential fit of scintillation pulses of all measured samples.

Sample	τ_{d1} [ns] (ρ_1 [%])	τ_{d2} [ns] (ρ_2 [%])	τ_{d3} [ns] (ρ_3 [%])	τ_{d4} [ns] (ρ_4 [%])	χ^2	$\tau_{d,\text{eff}}$ [ns]
BGO	0.8 ± 0.3 (0.2 ± 0.1)	37 ± 7 (7.5 ± 0.4)	318 ± 22 (92.3 ± 0.4)	–	1.47	129 ± 10
LSO	7.9 ± 0.8 (6 ± 1)	33 ± 1 (94 ± 1)	–	–	1.08	28 ± 1
LYSO	27 ± 8 (23 ± 7)	44 ± 3 (77 ± 6)	–	–	1.02	38 ± 1
EJ232	1.24 ± 0.02 (82 ± 1)	17 ± 3 (18 ± 1)	–	–	1.23	1.48 ± 0.01
EJ232Q	0.08 ± 0.03 (10 ± 1)	0.82 ± 0.03 (72 ± 1)	11 ± 1 (18± 1)	–	2.08	0.46 ± 0.09
BC422	1.20 ± 0.01 (81 ± 1)	12 ± 1 (19 ± 1)	–	–	1.14	1.44 ± 0.01
InGaN	0.007 ± 0.002 (8 ± 1)	1.9 ± 0.1 (41 ± 1)	92 ± 37 (51 ± 2)	–	1.03	0.08 ± 0.02
CPB	0.010 ± 0.002 (9 ± 1)	0.83 ± 0.03 (20 ± 1)	7.7 ± 0.1 (56 ± 2)	26.7 ± 0.2 (15 ± 1)	1.09	0.11 ± 0.02

Table 8.3: Summary table with effective decay time ($\tau_{d,\text{eff}}$), time resolution at FWHM (DTR) and light output (LO), defined as the mean of the collected charge distribution.

Sample	$\tau_{d,\text{eff}}$ [ns]	DTR [ps]	LO [nWb]
BGO	129 ± 10	3984 ± 148	0.728 ± 0.002
LSO	28 ± 1	527 ± 13	5.33 ± 0.01
LYSO	38 ± 1	714 ± 18	4.84 ± 0.01
EJ232	1.48 ± 0.01	314 ± 5	0.806 ± 0.001
EJ232Q	0.46 ± 0.09	339 ± 6	0.380 ± 0.001
BC422	1.44 ± 0.01	327 ± 5	0.696 ± 0.001
InGaN	0.08 ± 0.02	284 ± 6	0.909 ± 0.004
CPB	0.11 ± 0.02	295 ± 6	0.421 ± 0.001

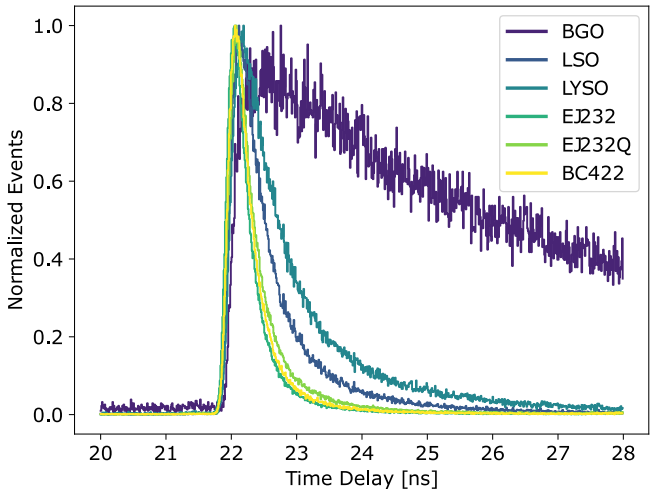

Figure 8.6: Time delay distribution of all the measured standard scintillator. Figure published in [97].

8.4.2 Validation of the experimental setup

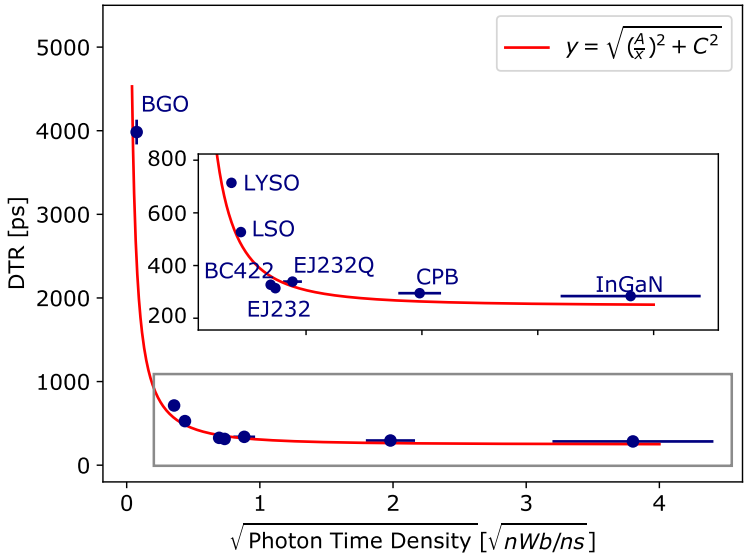

Figure 8.7: For all samples, the measured DTR is shown as a function of the square root of photon time density, defined as the ratio between the mean collected charge and the effective decay time. The data were fitted with the function $y = \sqrt{(A/x)^2 + C^2}$ (red curve) to take into account also the system contribution (C). For all data, the error is represented for both the x-axis and y-axis and when it is not visible, it means it is smaller than the point size. Figure published in [97].

The relation between the (coincidence) time resolution, scintillation kinetics, and light output [5, 77] has been already thoroughly discussed along this thesis

work. Here, we remind that the time resolution is inversely proportional to the photon time density (PTD), defined as the ratio between light output and effective decay time:

$$DTR \propto \sqrt{\frac{\tau_{d,\text{eff}}}{LO}} \propto \sqrt{\frac{1}{PTD}} \tag{8.1}$$

The validation of the newly installed setup, designed to simultaneously evaluate time resolution and light output upon X-ray excitation with SiPM, was based on the verification of this relationship. In Figure 8.7, the measured DTR is represented as a function of the square root of the measured photon time density. The function $y = \sqrt{(A/x)^2 + C^2}$ was used to fit the data, where in addition to the proportionality factor A, a constant C was added in quadrature to take into account also the system contribution.

Indeed, when stating DTR values as FWHM of the time delay peak, we are assuming zero contribution from the system, which is not the case. When having two detectors in coincidence, assuming the contribution from the two to be Gaussian, the coincidence time resolution is given by:

$$CTR = \sqrt{DTR_1^2 + DTR_2^2} \tag{8.2}$$

with DTR_1 and DTR_2 are the DTR of two detectors individually. In this case, the coincidence is made with the trigger of the laser, and by approximating all the contributions to be Gaussian, we get:

$$DTR_{exp} = \sqrt{DTR_{intr}^2 + IRF^2}, \tag{8.3}$$

where DTR_{exp} is the measured FWHM, as reported in Table 8.3, and DTR_{intr} the intrinsic time resolution of the detector which would be obtained after the subtraction of IRF contribution.

A rough estimation of the system contribution can be made from that of the TCSPC setup (Section 8.2.2). The main difference in the detection chain of the two setups is the photodetector: in the *TCSPC bench*, the HPM has an IRF below 20 ps [134], while in the *DTR and LO bench* the SPTR of Hamamatsu S13360 SiPM was measured to be 144 ps [5]. In the approximation of all the contributions to be Gaussian, the system IRF of the X-ray DTR setup is around 215 ps. The parameter C from the fit resulted to be 247±10 ps, compatible with the estimated result within three sigma.

However, because the system IRF is not Gaussian (see Figure 8.2) it was decided not to correct the measured FWHM values for system IRF. Nevertheless, it is worth emphasizing that proper modeling of the system's IRF contribution and its subtraction, or an improved IRF measurement, could lead to even better intrinsic DTR values.

8.4.3 In-depth Analysis of LSO

For a further confirmation of the capabilities of the setup, LSO was investigated more in depth. First, the correlation between the deposited energy (i.e., the integrated charge) and time resolution was studied. Then the intrinsic light yield was extrapolated. The choice fell on LSO as this crystal was extensively studied and consistent light yield values were available in literature as reference [5].

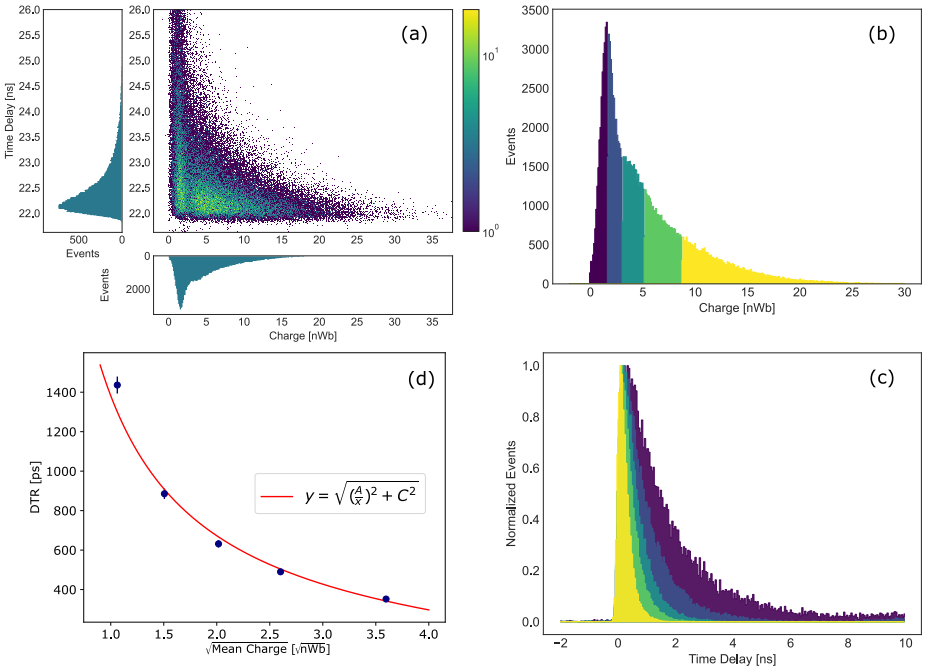

Figure 8.8: Correlation between time resolution (DTR) and deposited energy (mean integrated charge) for LSO. 2D histogram of time delay versus integrated charge (a). The charge distribution of LSO has been divided into five intervals containing about the same number of events (b), for each interval the mean charge was evaluate and the time delay distribution was considered (c) and the DTR was evaluated as FWHM of the distribution. Finally the DTR was plotted as function of the square root of the mean charge, and fitted with $y = \sqrt{(A/x)^2 + C^2}$ (d). Figure published in [97].

To investigate the correlation between deposited energy and time resolution, the charge distribution of LSO was divided into five intervals containing approximately the same amount of events, for each of them the mean charge was evaluated and the time delay distribution of the corresponding events was considered. Figure 8.8 (b) and (c) shows the selected energy interval and the corresponding time delay distribution, respectively. For each time delay distribution obtained, the DTR was evaluated and studied as a function of the mean charge. Since we are considering only one material, and the decay time is independent on the energy, it was factored out and included in the proportionality factor. Once again, the DTR resulted inversely proportional to the square root of the deposited energy Figure 8.8 (d).

To extrapolate the light yield from the measured collected charge, we must consider several correction factors, such as the calibration for single photoelectron pulse (SPe), the photodetection efficiency (PDE), the light transfer efficiency (LTE), the excess charge factor (ECF) coming from SiPM crosstalk, non-proportionality (NP).

All these corrective factors are known with good enough precision for LSO. The weighted PDE of an Hamamatsu S13360 SiPM for co-doped LSO emission is reported to be 0.59±0.03 [5]. The light yield non-proportionality with the deposited energy depends on the exact doping of the crystal, and different values were found in literature, ranging from 0.55 to 0.7 at 15 keV [135, 136]. A NP

value of 0.65±0.1 was chosen, noting that its high relative error contributes significantly to the final uncertainty. The ECF at the operational bias voltage was estimated to be 1.33±0.07. Finally, by considering the LTE value of 0.66 reported by [5] for an identical crystal (same size, doping, surface state, and producer) wrapped in Teflon, a relative light output measurements with and without Teflon wrapping was performed. An LTE of 0.35±0.02 was found for unwrapped co-doped LSO crystal. By taking into account all these corrective factors, we obtain:

$$\begin{aligned} ILY &= \frac{1}{\text{PDE} \cdot \text{NP} \cdot \text{LTE}} \cdot \frac{1}{\text{<En> [keV]}} \cdot \frac{\text{LO[nWb]}}{\text{SPe [nWb]}} \cdot \frac{1}{\text{CT}} \\ &= 39.8 \pm 7.0\,\text{ph/keV}, \end{aligned} \tag{8.4}$$

in good agreement with the value obtained by [5] of 39.2±3.9 ph/keV. This result confirms the validity of the chosen figure of merit for the light output and of the calibration procedure.

With the same procedure, the intrinsic light yield of any samples measured with the described method can be obtained. However, a good knowledge of the corrective factors is needed and, in particular for nanomaterials, this may require complementary measurements.

8.4.4 Application to low-stopping power and low-density scintillators

In Figure 8.9 the charge distribution of low-stopping power samples (the two nanomaterials and EJ232 plastic scintillator) are compared to the one obtained measuring the only SiPM with a drop of Meltmount in the same condition. This measurement was performed to ensure that even in case of direct interaction of X-rays with Meltmount or SiPM (possibly relevant only with low-stopping power samples), the resulting light output is negligible. Therefore, based on previous discussion about the correlation between timing and collected charge, we can conclude that the contribution of SiPM and coupling medium to the measured DTR is negligible, ultimately confirming the effectiveness of this method with low stopping power samples.

Measuring time resolution at low energy while simultaneously obtaining information on light output allows us to estimate time performance at higher energies by considering the relationship between time resolution and deposited energy and scaling accordingly.

Taking again LSO as an example, a DTR of 527±13 ps was measured at 15 keV mean deposited energy. At 511 keV we can therefore expect a CTR of

$$CTR_{@^{22}Na} = \sqrt{2} \cdot DTR_{@Xray} \sqrt{\frac{\text{Energy}_{@Xray} \cdot \text{NP}}{\text{Energy}_{@^{22}Na}}} = 103 \pm 3\,\text{ps}. \tag{8.5}$$

Considering the different LTE for a 3x3x3,mm^3 LSO crystal when wrapped in Teflon (0.66) and unwrapped (0.35), as discussed in Section 8.4.3, a correction factor of $\sqrt{0.66/0.35} = 1.37$ was calculated. This correction leads to a CTR of 75±6,ps, which well matches the value measured by [5] of 75±3,ps.

The possibility to measure time resolution at 10-15 keV and scale it to higher energy is of fundamental importance for those material which cannot

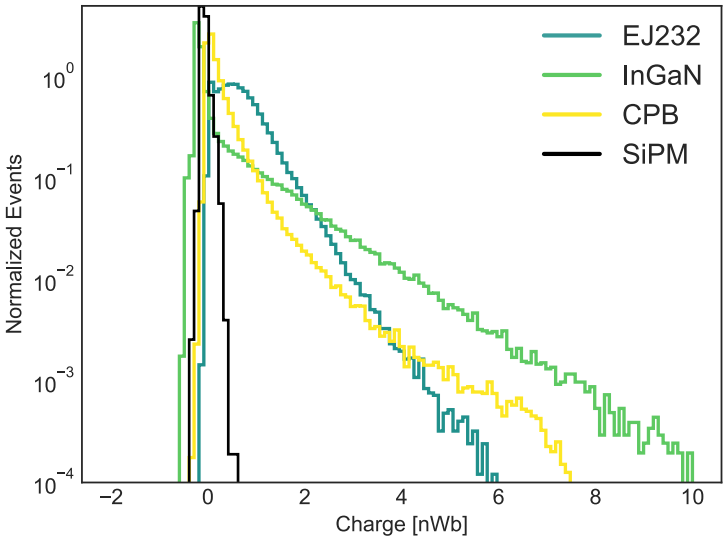

Figure 8.9: Comparison between integrated charge of low stopping power samples (EJ232, InGaN and CPB) and only SiPM. Figure published in [97].

be directly characterized at the desired energy. A CTR of 35±2 ps (25±1 ps DTR) was measured at 340 keV for BC422 plastic scintillator [5]. Under X-ray irradiation, this scintillator showed a DTR of 327±5 ps, while the two nanomaterials measured, InGaN and CPB, 284±6 ps and 295±6 ps respectively. Considering that the mean energy deposited and converted into scintillating photons in the two nanomaterials is likely lower than in pure plastic scintillators, these results suggest that, with increased stopping power, these materials could achieve a coincidence time resolution in the range of 20 ps at 511 keV. This is attributed to their higher photon time density, as illustrated in Figure 8.7.

8.5 TOF X-ray Imaging

This setup has also a direct applicability in the development of detector for TOF X-ray imaging. The possibility to exploit TOF information to reduce the contribution from scattered photons was introduced by [137, 138] and a first proof of concept of TOF CT was provided by [139].

Further studies based on GATE simulations [140] showed that already 200 ps time resolution can remove half of the scattered photons, significantly improving the quality of the reconstructed image compared to non-TOF CT. Considering that for this study an X-ray tube emitting photons with energy up to 40 keV and mean energy about 15 keV has been used, it is worth noting that all the tested plastic scintillators would already achieve sub-200 ps time resolution at typical CT energies (20-150 keV), at least under laboratory conditions and compatibly with the system IRF.

8.6 Summary and Conclusion

In this Chapter, the validation of an experimental setup capable of simultaneously measuring the light output and time resolution following soft (0-40 keV) X-rays excitation was presented.

The validation process focused on confirming the inverse proportionality between time resolution and photon time density. For this scope, standard bulk scintillator were used, with particular emphasis on LSO. These measurements estimated LSO ILY to be 39.8 ± 7.0 ph/keV, in excellent agreement with previously published values [5]. A DTR of 527 ± 13 ps was measured at a mean energy of 15 keV. With appropriate corrections, including energy scaling and considering LTE variation due to different measurement conditions, a CTR of 75 ps was estimated at 511 keV, again in perfect agreement with the value measured by Gundacker et al. [5].

This setup addresses a significant challenge in the characterization of materials with low-stopping power and low-density, which conventional techniques relying on γ-sources struggle to tackle. The capability to work with soft X-rays is promising for guiding the development of nanoscintillators, a new and emerging class of scintillating materials that are often affected by these limitations. These advancements are crucial especially in the context of radiation detectors for fast timing applications like TOF-PET and in High-Energy Physics (HEP).

Another positive implication of this setup is the possibility to characterize and have direct information about the performances of materials for fast X-ray detectors to be used for TOF CT or, more in general, TOF X-ray imaging.

Chapter 9

Nanocrystalline Lead Halide Perovskite

9.1 Introduction

Lead halide perovskite ($CsPbX_3$; X = Cl, Br, I) nanocrystals (NCs) have captured significant attention of the scientific community in the last decade, especially in the field of optoelectronics, due to their very fast and bright luminescence with narrow and easily tunable emission in the visible region [141, 142]. Especially bromides have been extensively studied as scintillators with ongoing research exploring their potential to enhance the timing performances of radiation detectors in a wide range of applications, including both medical imaging and high energy physics experiments [64, 96, 143].

The main drawback is the need for macroscopic (cm^3-scale) large detectors in order to achieve a reasonable stopping power. For convenience and protection from detrimental environmental influence, perovskite NCs are usually embedded in a solid matrix (polymer or glass) [144, 145] which lower the density of the overall nanocomposite. Moreover, semiconductor nanocrystals such as lead halide perovskites, suffer from the small Stokes shift [141, 146]. Therefore, to guarantee good transparency and efficient light transport, such nanocomposites can neither be thick enough to provide sufficient stopping power, nor dense enough in terms of NCs loading, resulting in a detector with poor scintillation efficiency and/or poor light output.

In this Chapter, the scintillation properties of both free $CsPbBr_3$ (CPB) NCs and embedded in polystyrene matrix are investigated. Their time resolution is measured with the experimental setup introduced in the previous Chapter.

Specifically, in Section 9.2.1 and 9.2.2, the synthesis of $CsPbBr_3$ NCs is described and an overview of all the samples investigated is provided. Sections 9.2.3, 9.2.4, 9.2.5 present the method for the characterization of these samples in terms of optical properties, decay kinetics, and time resolution, respectively, under soft X-ray excitation. The corresponding results are presented in Sections 9.3.1, 9.3.2, and 9.3.3. In Section 9.3.4, we also illustrate the potential of thin films of CPB NCs as time enhancing coating layers for bulk, dense crystal in TOF-Xray application. Finally, a proof of concept of heterostructured scintillator using GAGG and thin film of free $CsPbBr_3$ NCs is also discussed (Section 9.2.6 and

9.3.5).

9.2 Material and Methods

9.2.1 Synthesis and Fabrication of $CsPbBr_3$ nanocrystals

Three different sets of $CsPbBr_3$ samples were used for this study: $CsPbBr_3$ embedded in polystyrene using standard combination of oleic acid and oleylamine (OA+OAm) as surface ligands; $CsPbBr_3$ embedded in polystyrene with didodecylammonium bromide (DDAB) ligand as surface ligand; free $CsPbBr_3$ NCs in solution with DDAB surface ligand. The role of the surface ligand is to passivate the surface of the nanoparticles to improve their luminescence properties and prevent aggregation. DDAB was reported to exhibit better surface passivation capability compared to OA+OAm, resulting in higher quantum yields (and stability) [147, 148], and part of this study was aimed to confirm this aspect.

The $CsPbBr_3$ NCs were synthesized at the Czech Technical University (CTU) in Prague by Kateřina Děcká and Jan Král. The hot-injection method as illustrated by Protescu et al. [141] was followed, with some modifications first introduced by Lu et al. [149]. It is based on a reaction of Pb^{2+}, Cs^{+}, and Br^{-} ions in a high boiling solvent (octadecene) in presence of OA+OAm ligands. Two precursor solutions are mixed fast at high temperature leading to controlled arrested precipitation in colloidally stabilized $CsPbBr_3$ nanocrystals.

In case of DDAB samples, the hot-injection synthesis was followed by the ligand exchange reaction replacing original ligands with DDAB [148].

The nanocrystals were then precipitated by ethyl acetate and isolated by centrifugation. The $CsPbBr_3$ nanocrystals were redispersed in toluene and a final solution with concentration of around 35 mg/ml was obtained.

For the polystyrene (PS) nanocomposite samples, approximately 210 mg of polystyrene pellets were dissolved in toluene and the calculated amount of $CsPbBr_3$ solution was pipetted to obtain the desired final NCs concentration of 1 %, 5 % and 10 %. The viscous solution was thoroughly stirred until complete homogenisation and the toluene was left to evaporate in air at room temperature for about two weeks, finally resulting in 5 cm diameter discs with a thickness of 100 μm, as measured by a caliper with 20 μm resolution.

The pictures of the obtained samples are shown in Figure 9.1 (a). One can observe the opacity of the samples increasing with the increasing NCs loading. However, also at 10 % loading (the highest reported in literature at the best of our knowledge), some transparency is preserved. Already by eye, the DDAB samples look more transparent.

More details about the chemicals and the procedure used can be found in the former publications of the group at CTU who took care of the synthesis of the $CsPbBr_3$ and participated to the characterization of the obtained samples [96, 150].

9.2.2 Samples

From here on, for sake of simplicity, $CsPbBr_3$ will be abbreviated into CPB.

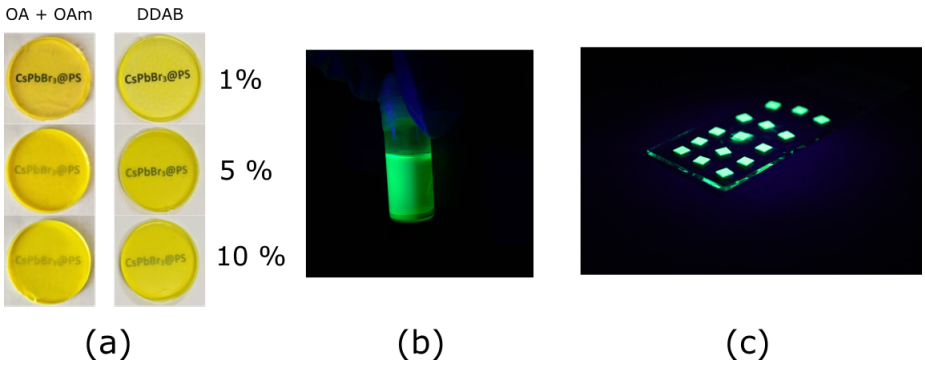

Figure 9.1: Pictures of the produced CPB NCs samples. (a) CPB embedded in polystyrene with different NCs laoding and capped with different ligand surfaces. (b) CPB NCs in solution, illuminated with UV light. (c) Thin film of CPB NCs deposited on GAGG plates, illuminated with UV light.

$CsPbBr_3$ Nanocrystals embedded in Polystyrene

Two sets of CPB embedded in polystyrene (CPB@PS) samples were prepared with three different nanocrystal filling factors – 1, 5, 10 % – for a total of six samples, as shown in Figure 9.1 (a). One set was prepered using the OA+OAm surface ligand (OA+OAm set) and the second one using the DDAB surface ligand after the ligand exchange procedure (DDAB set).

From the 5 cm diameter and 100 μm thick discs, $3\times3\,mm^2$ plates were cut. All the samples embedded in polystyrene had therefore size $3\times3\times0.1\,mm^2$.

Free $CsPbBr_3$ Nanocrystal

The free CPB NCs were studied both as standalone scintillators (by drop-casting the solution on a SiPM or non-scintillating glass, depending on the type of measurement) and in combination with standard single crystal scintillators following a heterostructure approach.

The single crystal scintillators used were BGO, LYSO, and GAGG. BGO was selected due to its extensive use in this thesis work within the framework of heterostructures. L(Y)SO represents the state-of-the-art crystal for TOF-PET applications [9, 115, 126, 151, 152], while GAGG was chosen because its emission falls above the absorption region of CPB [150] and it is therefore, among these three, the most suitable dense scintillator to combine with CPB.

Generally, single crystal plates had size $3\times3\times0.2\,mm^2$, and on top of them a CPB thin film of about 50 μm thickness was deposited.

GAGG was chosen for a more in-depth investigation of the potential of CPB as time enhancing coating. To study the effect of different thickness layers, thicknesses of 1, 8, 20 μm were also tested. A proof-of-concept of GAGG&CPB heterostructured scintillator was also tested by first measuring a single heterostructure unit made of a $6\times6\times0.2\,mm^2$ GAGG plate and a CPB thin film (about 50 μm thick). Then, a $3\times3\times3\,mm^3$ heterostructure made of alternated plates of GAGG and CPB thin films was assembled and measured.

Figure 9.1 shows the picture of the CPB NCs in solution (b) and of the deposited thin film on top of $3\times3\times0.2\,mm^2$ GAGG crystal plates (c).

9.2.3 Optical Characterization

Photoluminesce (PL) and radioluminescence (RL) spectra were measured, before the embedding, for both the CPB nanocrystals solutions, capped with OA+OAm and DDAB surface ligands.

The PL excitation and emission spectra were collected using a FluoroMax spectrofluorometer (Horiba Jobin Yvon), equipped with an Ozone-free Xenon lamp and a R928P photon counting PMT covering a wavelength range as wide as 185-850 nm.

The RL emission spectra were measured with the 5000M spectrofluorometer (Horiba Jobin Yvon), comprising a Seifert X-ray tube (40 kV, 15 mA) as excitation source, a monochromator, and a TBX-04 (IBH Scotland) photodetector.

Following the embedding process, RL spectra were acquired again for all the obtained samples: 1 %, 5 %, and 10 % NCs loading for both the two sets, DDAB and OA+OAm.

Additionally, on all these samples, transmission spectroscopy was also performed using a PerkinElmer LAMBDA 650 UV/VIS spectrometer, equipped with Deuterium and Tungsten halogen light sources, which allow for covering a wavelength range as wide as 190-900 nm.

9.2.4 Decay Kinetics

The scintillation kinetics of all the synthesized perovskite samples – free CPB NCs and the two full sets of CPB@PS was measured with the X-Ray TCSPC setup described in Section 8.2.2. To measure the scintillation kinetics of free CPB NCs, a few layers of the solution were drop-casted on top of a non-scintillating glass plate.

The scintillation time profiles were modeled with the convolution between the instrumental response function of the system IRF and the intrinsic scintillation rate. Because of the ultra-fast (sub-nanosecond) decay kinetics of CPB NCs, the intrinsic scintillation rate was modelled as the sum of three bi-exponential functions and the Dirac-delta function [96]. This model was chosen on the trail of the one used by Gundacker et al. [129] to describe the scintillation time profile of BGO, which comprises both scintillation and prompt Cherenkov photons.

All samples showed an instantaneous rise time that could not be resolved by the IRF of the system. As it was found that it did not improve the quality of the fit, in order to have more stability on the decay part (as in the bi-exponential function the rise and decay components are correlated), it was fixed at 0 ps, as already done for the studies described in Chapter 6 and 9.

9.2.5 Time Resolution and Light Output upon X-ray irradiation

The DTR and LO upon X-ray irradiation were measured with the experimental setup described in Section 8.2.3. As a brief reminder of the core principle of these measurements, the samples were coupled to a SiPM (S13360-3050CS from Hamamatsu, 53V breakdown voltage, 61V bias voltage) collecting the scintillation light produced following X-ray excitation (see Figure 9.2 (a) and (b)). The SiPM signal was read out by a front-end electronics, which separately process the time and energy information. The time signal is processed by a HF circuit [9, 108],

which was introduced in Section 6.2. The time resolution is obtained as the FWHM of the distribution resulting from the measure of the time delay between the SiPM signal and the external trigger of the X-ray tube. By integrating the energy signal, the light output of the sample is also obtained.

The samples object of these measurements were the two full sets of CPB@PS, the free CPB NCs directly drop-casted on the SiPM, and the three inorganic crystals (BGO, LYSO, and GAGG) with the CPB timing enhancing coating. To evaluate the timing improvement achieved by adding the CPB layer, the stand-alone GAGG, BGO, and LYSO were also measured as a reference.

The three inorganic crystals were first coupled to the SiPM and measured in their standalone scintillator state. Subsequently, 12 μL of CPB which, that considering the surface of the plates correspond to a thickness of about 50 μm, were deposited onto each crystal without removing them from the SiPM. This approach ensured a fair comparison between the inorganic bulk crystals with and without the perovskite layer, unaffected by different coupling conditions.

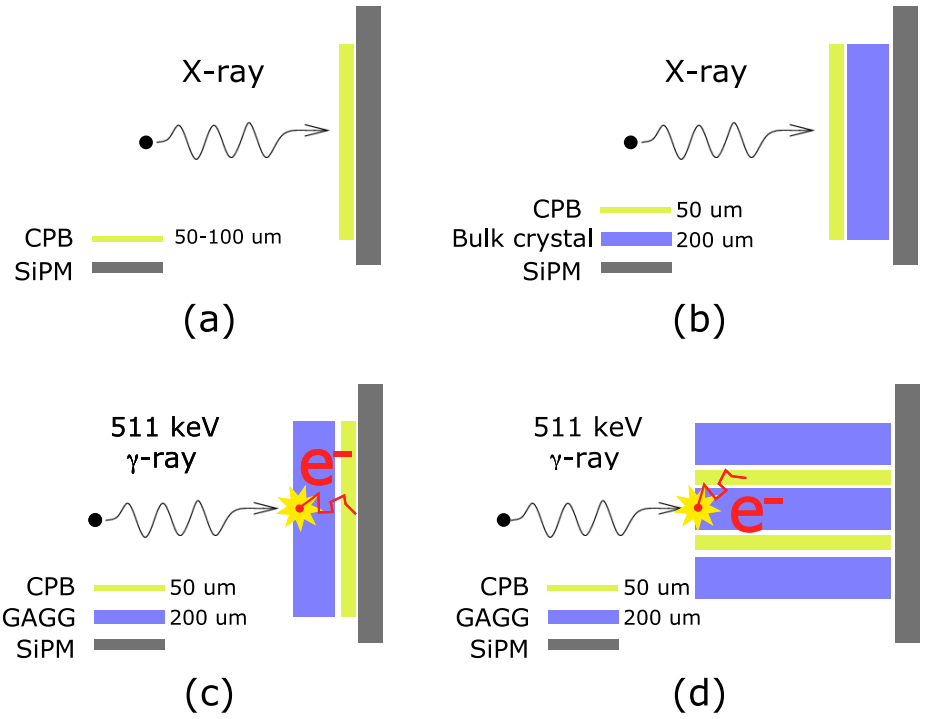

Figure 9.2: Configuration for time resolution measurements of (a) only CPB under X-ray excitation, (b) CPB layer combine with an inorganic bulk crystal under X-ray (c) and under 511 keV γ-ray excitation, and (d) full heterostructure alternated plates of GAGG and CPB thin films under 511 keV γ-ray excitation

It is worth emphasising that it is crucial that the CPB layer faces directly towards the X-ray beam (see Figure 9.2 (b)) since, given the low energy of the radiation, X-rays would otherwise be fully absorbed by the dense scintillator.

To study the influence of different thicknesses of CPB layer, the measurements with GAGG were repeated by first drop-casting on it a single drop of 0.5 μL of CPB solution, and subsequently increasing the amount by depositing up to 2 μL and 5 μL. For the same considerations made above, these three volumes

correspond to about 1, 8, and 20 μm thickness, respectively.

To assess the timing performance of solely CPB nanocrystals, 12 μL of their solution was drop-casted directly on the SiPM.

9.2.6 Coincidence Time Resolution upon 511 keV γ-ray irradiation

For this study, 20 μL of CPB were drop-casted on a $6 \times 6\,\mathrm{mm}^2$ (hence resulting in a layer of about 20 μm thickness) SiPM (S13360-6050PE from Hamamatsu, 53 V breakdown voltage, 61 V bias voltage) and a $6 \times 6 \times 0.2\,\mathrm{mm}^3$ GAGG plate was placed on top of it as depicted in Figure 9.2 (c). This geometric configuration was employed to trigger the energy-sharing mechanism, the principle underlying heterostructured scintillators, as discussed in Chapter 3.

The experimental setup used to measure the coincidence time resolution under 511 keV γ-ray excitation was the same as described in detail in Section 6.2.

In brief, the sample was placed on the opposite sides of a ^{22}Na source and measured in coincidence with a reference crystal ($2 \times 2 \times 3\,\mathrm{mm}^3$ LSO:Ce:Ca0.4%, 61 ps CTR FWHM). The SiPM signal was read out by an HF readout circuit (the same used also for the time resolution under X-ray) and finally digitized by a LeCroy DDA735Zi oscilloscope (3.5 GHz bandwidth, 20 Gs/s sample rate).

Both the amplitude and integrated charge of the energy signal were recorded to enable pulse shape discrimination, allowing for distinguishing the events according to the material where the energy is deposited (Section 4.3).

The rise time of the time signal (i.e., the time difference between the two fixed thresholds through which the signal passes as explained in Section 6.2.3 and depicted in Figure 6.4) also allows for discriminating the events according to the material where the energy is deposited. This quantity depends on the scintillation kinetics of the material, but must not be confused with the scintillation rise time.

Finally, the time delay between the time signals of the test sample and the reference detector was measured and the CTR was obtained as FWHM of this distribution after applying the time walk correction and correcting by the reference contribution.

The same measurement was also repeated with a full $3 \times 3 \times 3\,\mathrm{mm}^3$ heterostructure made of alternated plates of GAGG and CPB thin films.

9.3 Results

9.3.1 Optical properties

The PL and RL measurements of the two sets (OA+OAm and DDAB) of CPB NCs performed before the embedding process, highlighted the larger PL and RL intensities of CPB NCs capped with DDAB, as shown in Figure 9.3. This is in agreement with the expectations and results published in literature [148].

After the embedding process, the RL spectra were measured again for the two full sets of obtained samples. In both cases, we see the RL intensities increasing with the NPs loading (Figure 9.4 (b) and (d)) accompanied by a decrease in transmittance (Figure 9.4 (a) and (c)).

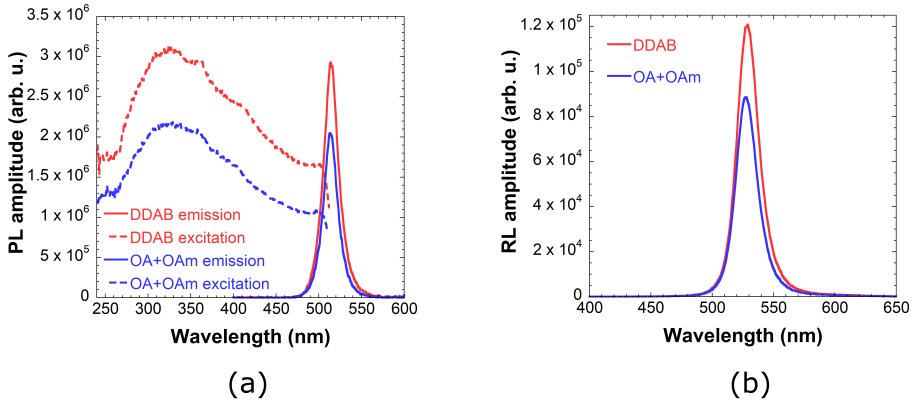

Figure 9.3: (a) PL excitation (dashed line) and emission (solid line) spectra of free $CsPbBr_3$ NCs capped with DDAB (red) and OA + OAm (blue). (b) RL spectra of free $CsPbBr_3$ NCs capped with DDAB (red) and OA+OAm (blue). Figure published in [96].

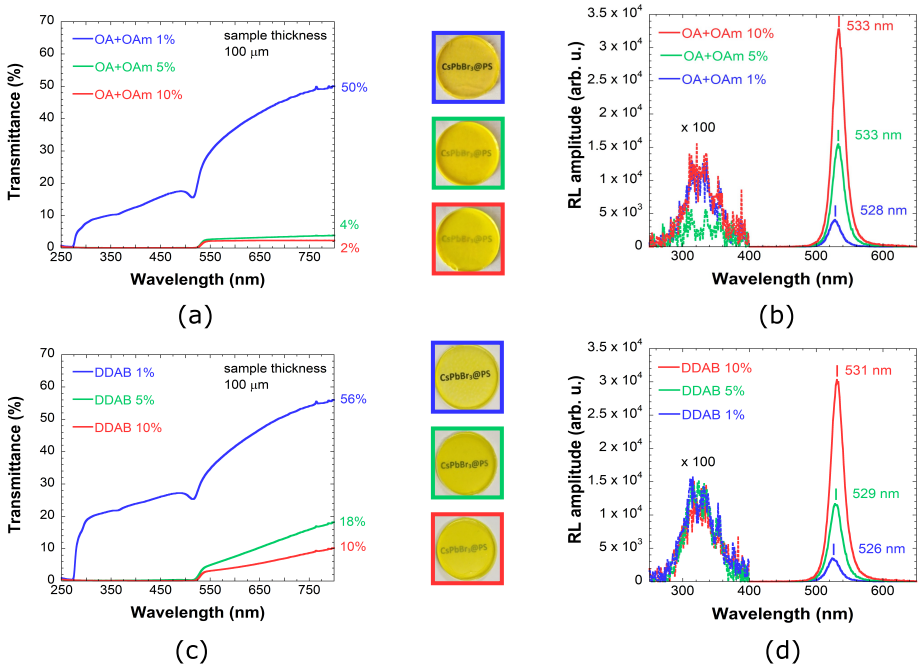

Figure 9.4: (a) Transmission spectra and (b) RL spectra of samples from the OA+OAm set, (c) transmission spectra and (d) RL spectra of samples from the DDAB set, with various filling factors. Blue, green and red lines represent 1 %, 5 % and 10 % filling factors, respectively. The RL spectra were multiplied by the factor of 100 in the interval 250 nm – 400 nm to reveal the weak polystyrene emission. Figure published in [96].

The transmittance of the 1 % CPB samples of the two sets is about the same above 550 nm. However, in the same wavelength range, the 5 % and 10 % samples in the DDAB set exhibited significantly improved transmittance compared to the OA+OAm set, with values reaching as high as 18 % and 10 % (for 5 % and 10 % DDAB, respectively), in contrast to 4 % and 2 % (for 5 % and 10 % OA+OAm,

respectively).

In the wavelength range 300-500 nm, only the 1 % CPB sample demonstrated satisfactory transparency. Notably, the sample capped with DDAB exhibited almost double the transparency compared to the one capped with OA+OAm. Conversely, the 5 % and 10 % samples from both sets proved to be essentially opaque within this range.

The low transmittance above 500 nm is mainly due to scattering, while below this threshold to the nanoparticles absorption, as one can observe from the PL excitation spectra in Figure 9.3 (a). The drop in the transmittance spectra around 510-530 nm (Figure 9.4 (a) and (c)) correspond indeed to the absorption edge.

Both these effects become more pronounced as the nanoparticle loading increases, and it can be attributed to the clustering and/or aggregation of the nanoparticles. *Clustering* is here intended as nanocrystals not homogeneously spread in the nanocomposite but forming larger clusters, however preserving their shape and size. While *aggregation* implies that the nanoparticles interact with their neighbour forming bigger particles. As the scintillation properties depend on the size of the nanoparticles (Chapter 2.3.4), if aggregation occurs changes in the decay kinetics (otherwise not expected) of the CPB nanocomposite depending on the NCs loading should be observed.

Furthermore, from the comparison between DDAB and the OA+OAm set, we can deduce that the former at least partially prevents nanoparticles clustering/aggregation.

9.3.2 Decay kinetics of CPB

Figure 9.5 shows the scintillation time profile of free CPB NCs deposited on non-scintillating glass following X-ray excitation and acquired in TCSPC mode. The intrinsic scintillation rate was modeled as the sum of three exponential decay components ($\tau_{d,1/2/3}$) and the Dirac-delta function (δ) to describe the ultra-fast emission of the sample (Section 9.2.4). This component was found to contribute about 22 %, as well as the fastest and sub-nanosecond (about 600 ps) exponential decay component, resulting in about 45 % of the photons emitted within the first nanosecond.

The results of the decay kinetics of the two sets of CPB embedded in polystyrene are summarized in Table 9.1, and they resulted overall comparable with the values measured for the free CPB NCs. All of them showed a prompt component contributing for the 14-24 %, an exponential sub-nanosecond component between 700 ps and 900 ps contributing for the 17-24 %, again resulting in 30-45 % of photons emitted within the first nanosecond.

Overall, all the CPB samples demonstrate high initial photon time density (i.e. number of photons emitted in the first few nanoseconds), the main parameter affecting the time resolution of a material.

It is interesting to note that samples belonging to the OA+OAm set showed a progressively increase of the slowest decay component (τ_{d3}) and its corresponding weight (ρ_3) together with the NCs concentration, at the expense of the fastest exponential decay component (τ_{d1}). On the contrary, for the DDAB samples, no clear trend is observable.

This finding, together with the results on the transmittance of polystyrene samples, confirms the improved ability of DDAB to passivate the surface of

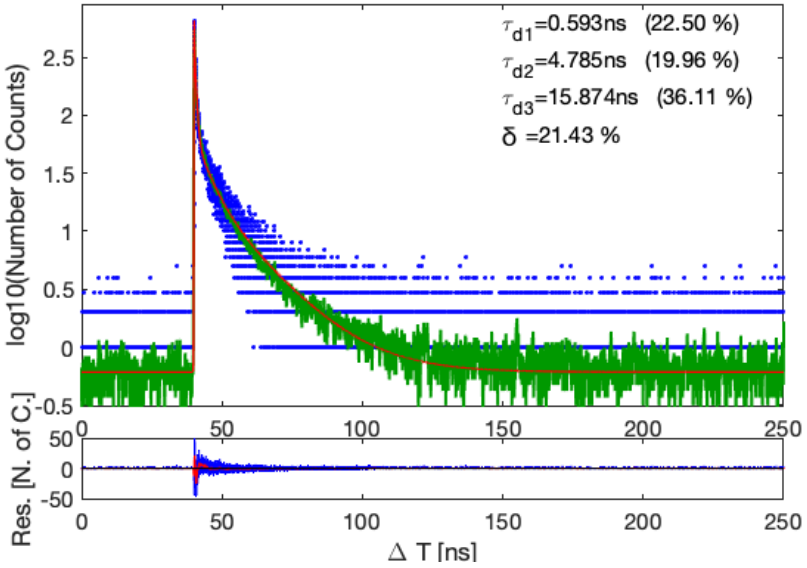

Figure 9.5: Scintillation time profile of solely CPB layer on the non-scintillating glass wafer. Blue dots are the measured data, the green line is their average, the red curve is the fit function. The intrinsic scintillation rate was modeled as the sum of three exponential decay components ($\tau_{d,1/2/3}$) and the Dirac-delta function (δ) to describe the ultra fast emission of the sample.

Table 9.1: Fit results of all scintillation decays. δ is the weight of the delta function used to model the ultra-fast component, τ_{d1}, τ_{d2} and τ_{d3} are the exponential decay components with the respective weights (ρ_1, ρ_2 and ρ_3), and $\tau_{d,\text{eff}}$ is the effective decay time.

Sample		τ_{d1} [ns]	ρ_1 [%]	τ_{d2} [ns]	ρ_2 [%]	τ_{d3} [ns]	ρ_3 [%]	δ [%]	$\tau_{d,\text{eff}}$[1][ns]
OA +OAm	1%	0.76 ± 0.02	24 ± 4	3.0 ± 0.3	27 ± 3	11 ± 1	31 ± 7	18 ± 2	1.9 ± 0.2
	5%	0.68 ± 0.02	18 ± 3	3.4 ± 0.3	30 ± 4	18 ± 2	28 ± 5	24 ± 3	2.0 ± 0.2
	10%	0.69 ± 0.02	14 ± 2	4.1 ± 0.4	28 ± 4	26 ± 3	42 ± 7	16 ± 2	2.9 ± 0.3
DDAB	1%	0.92 ± 0.03	18 ± 3	3.9 ± 0.4	29 ± 4	21 ± 3	37 ± 7	16 ± 2	2.9 ± 0.3
	5%	0.79 ± 0.02	17 ± 3	3.5 ± 0.3	35 ± 4	18 ± 2	28 ± 5	20 ± 2	2.4 ± 0.2
	10%	0.79 ± 0.02	17 ± 3	3.9 ± 0.4	27 ± 3	15 ± 2	36 ± 6	20 ± 2	2.6 ± 0.2

[1] The fit function was normalized so that the weights of the four components add up to one ($\sum_{i=1}^{3}\rho_i + \delta = 1$), but the effective decay time was calculated with re-normalized ratio: $\rho_{n,i} = \frac{\rho_i}{\sum_i \rho_i}$ and $\frac{1}{\tau_{d,\text{eff}}} = \sum_i \frac{\tau_{di}}{R_{n,i}}$.

nanoparticles, preventing them from clustering or aggregating.

9.3.3 Time resolution of CPB upon X-ray excitation

Table 9.2 summarizes the detector time resolution measured for the only CPB samples, free or embedded in polystyrene.

In the previous Chapter 9, the time resolution of standard bulk scintillators was measured under the same irradiation conditions. A 3×3×3 mm^3 LSO:Ce:0.4%Ca crystal performing 75 ps CTR at 511 keV [5], showed a DTR at about 15 keV of 527 ps. The plastic scintillator BC422 of size 3×3×3 mm^3, was measured with a CTR of 40 ps under 511 keV irradiation by selecting on the

Table 9.2: Measured DTR values of all six samples embedded in polystyrene and free CPB.

	DTR (FWHM) [ps]	
	OA+OAm	DDAB
CPB@PS 1 %	305 ± 9	308 ± 9
CPB@PS 5 %	330 ± 10	309 ± 9
CPB@PS 10 %	319 ± 9	295 ± 8
Free CPB	//	196 ± 6

Compton edge at 340 keV [5] and 327 ps DTR at about 10 keV (mean energy deposited in plastic from the X-ray beam, according to Monte Carlo simulations). The DTR down to 196 ps measured for CPB is therefore remarkable.

In Chapter 9, we also showed how the time resolution at 15 keV correlates well with the time resolution measured at 511 keV by simply scaling for the different energy and possibly correcting for the non-proportionality. Assuming that the CPB is not affected by the non-proportionality and has the stopping power necessary to absorb 511 keV γ-rays, we can estimate a CTR of

$$CTR_{@^{22}Na} = \sqrt{2} \cdot DTR_{@Xray} \sqrt{\frac{\text{Energy}_{@Xray}}{\text{Energy}_{@^{22}Na}}} = 47 \pm 3\,\text{ps}. \tag{9.1}$$

for free nanocrystals. It should be mentioned that in this calculation we are not accounting for the system IRF (see Section 8.4.2) and that we are considering as mean deposited energy the same value used for bulk inorganic crystal. However, because of the lower density and scintillation efficiency, the average amount of energy deposited and then converted in scintillating photons is likely lower.

From the ICDD PDF-2 database (version 2013), card number 01-072-9729 (the crystallographic phase identified in the CPB nanocrystals synthesized from the CTU group [150]), the density of CPB orthorhombic bulk crystal resulted 4.83 g/cm^3, a factor 1.5 lower than the one of LSO. It should be further emphasised that this value refer to bulk crystal. Nanocrystals generally have lower density due to the significant proportion of surface atoms in their structure. Moreover, they are surrounded by organic ligands, further reducing the overall stopping power of such layers. Another factor to take into account is the non-uniformity in thicknesses of the layers due to the drop-casting process. The density, and by consequence the stopping power of CPB embedded in polystyrene is even lower.

Furthermore, in nanocrystal samples, the deposited energy must be transferred directly from the incoming radiation (or photoelectron in case of X-ray/γ excitation) to the nanoparticle. Not all of the energy deposited in the thin film (which also includes surface atoms and organic ligands) or in the polymer matrix when it comes to nanocomposites (where the NC concentration is significantly lower) is efficiently converted into scintillating light. Therefore, we expect even better intrinsic time performance from this material, if all relative limitations were addressed. This phenomenon can also explain why the CPB samples embeeded in polysterene showed a worse DTR compared to free CPB (300 ps against 200 ps, respectively): lower deposited energy, lower light output and thus worse time resolution.

Due to the difficulty in determining the actual energy deposited and efficiently converted into scintillating light, it was not possible to correctly estimate the

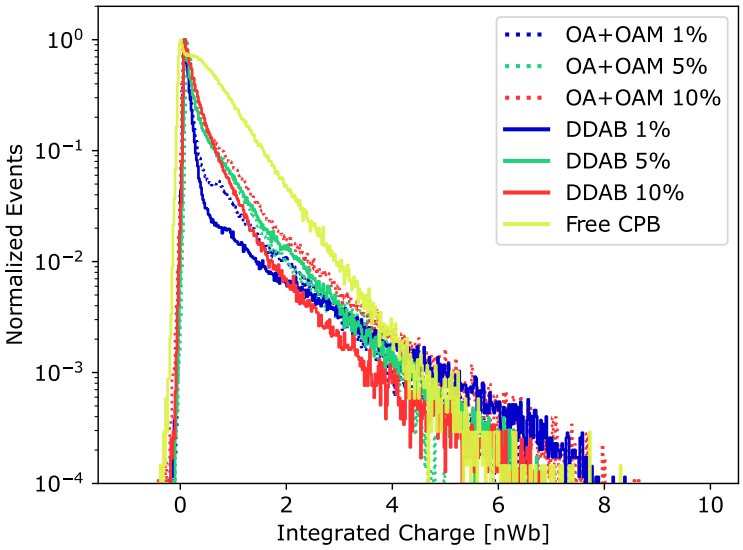

Figure 9.6: Integrated charge distribution of all CPB samples measured: CPB@PS with 1, 5, 10,% filling factor (blue, green read) of OA+OAm set (dashed lines) and DDAB set (solid lines), and free CPB (yellow solid line).

light emission in units of photons/keV. Moreover different shapes of integrate charge distribution were obtained (Figure 9.6), also making a relative comparison difficult. What is clear from Figure 9.6, is the larger amount of light collected from free CPB compared to the CPB@PS samples. This can be attributed to the much higher concentration of NCs, increasing the likelihood of energy being directly released to the nanoparticles and resulting in higher average deposited energy then converted in scintillating photons.

By comparing the time resolution of all synthesized samples, no significant difference was observed with increasing filling factor, for either of the two sets.

When considering the previous results collectively, we can gain insight into the light emission of these samples as the fill factor increases. From optical measurements, we have seen that samples with a higher fill factor show higher PL and RL, but also significantly lower transmittance. The absence of a clear trend of DTR with fill factor suggests that these two effects balance each other out.

9.3.4 CPB as Time Enhancing Coating Layer for TOF application

CPB demonstrated to have great potential in term of time resolution. However, the main limitations related to nanomaterials highlighted at the beginning of this Chapter and in Chapter 2.3.4, prevent them to be used as standalone detectors for X/γ-radiation. Also in CT, as it usually employs higher energies (60-120 keV) than the one available in our laboratory.

On the trail of the heterostructure concept, the time resolution under X-ray irradiation of CPB combined to bulk, dense scintillator was tested. The latter was coupled with the SiPM and a layer of free CPB NCs (about 50 μm thick) was deposited on top of it, resulting in a single heterostructure unit. The CPB

directly faces the incoming X-rays as depicted in Figure 9.2 (b). Therefore, with this approach, the energy sharing mechanism is not exploited: the incoming radiation encounters first the fast material, and in any case its energy would be too low for the recoil photoelectron to escape from the dense scintillator.

The basic principle is that the layer of free CPB has the sufficient stopping power to produce enough ultra-fast photons which will boost the overall time resolution of the sample. The dense, bulk scintillators serves to give the detector the necessary stopping power to stop also higher energy X-rays.

The measured time delay distributions are shown in Figure 9.7 and the FWHM values of all samples summarized in Table 9.3. The effect of the CPB layer on timing was significant in all cases, achieving a detector time resolution (DTR) of about 240 ps regardless of the type of bulk scintillator. That is more than a 10-fold improvement in timing capabilities compared to solely GAGG and BGO crystals (2.4 and 2.9 ns, respectively) and more than a 2-fold improvement compared to the state-of-the-art TOF-PET scintillator LYSO (590 ps).

It is worth recalling that the time resolution of the stand-alone CPB solution drop-casted directly on the SiPM was 196 ps FWHM, suggesting that the CPB layer dominates the time resolution of the overall heterostructure unit.

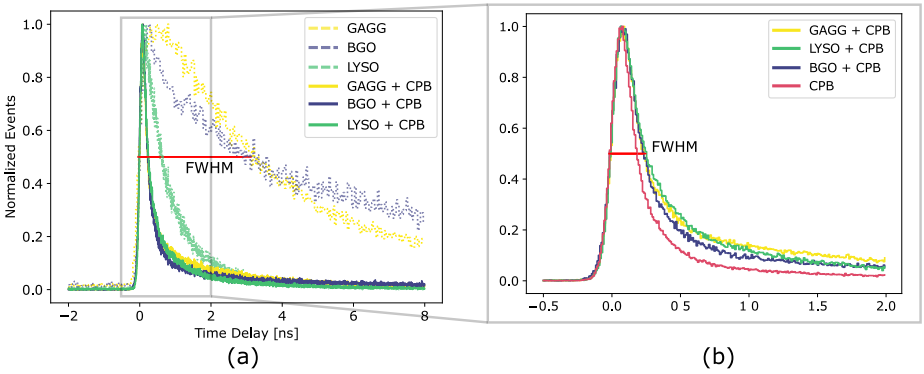

Figure 9.7: (a) Time delay distribution of the different samples measured: GAGG, LYSO, and BGO (yellow, green, and blue, respectively) without and with CPB layer (dotted and solid lines, respectively) and (b) Zoom in the first two nanosecond of the time delay distribution of the GAGG, LYSO, and BGO with CPB layer and compared to the only CPB layer.

Table 9.3: Measured DTR of GAGG, LYSO, and BGO without and with CPB layer evaluated in FWHM.

	DTR (FWHM) [ps]	
	w/o CPB	w/ CPB
GAGG	2365 ± 70	229 ± 7
BGO	2875 ± 86	236 ± 7
LYSO	590 ± 18	250 ± 8
Free CPB	//	196 ± 6

To investigate the influence of the CPB layer in detail, different volumes of the nanocrystals solution (namely 0.5, 2, and 5 μL corresponding to approximately 1, 8, and 20 μm thick layer) were drop-casted on a GAGG plate. It was decided to focus on GAGG to study this effect because, together with BGO, it showed the

greatest improvement in timing while having comparable light output and energy resolution to those of LYSO. These features make GAGG the best candidate to observe any variation due to the different CPB layer thickness. The results are shown in Figure 9.8 and summarized in Table 9.4.

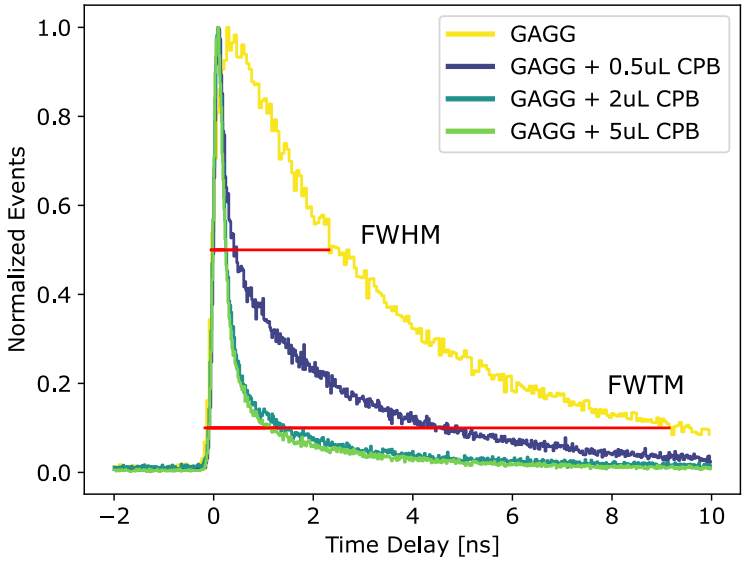

Figure 9.8: Time delay distribution of GAGG without and with CPB layer deposited in different thicknesses.

Table 9.4: Measured DTR of GAGG without and with CPB layer in different thicknesses evaluated both in FWHM and FWTM.

	CPB thickness	DTR [ps] FWHM	DTR [ps] FWTM
GAGG	-	2365 ± 70	9,3 ± 0.4
+ 0.5 μL CPB	1 μm	414 ± 17	4.5 ± 0.2
+ 2 μL CPB	8 μm	273 ± 11	1.4 ± 0.1
+ 5 μL CPB	20 μm	258 ± 10	1.1 ± 0.1

We can observe that a very thin film (about 1 μm thick) is sufficient to lead to a sizeable improvement in time resolution, from 2.4 ns to 414 ps (FWHM). By increasing the thickness of the CPB layer the time resolution saturates quickly: 273 ps with 8 μm and 258 ps with 20 μm, and considering the aforementioned results, 229 ps with 50 μm.

The initial improvement of time resolution with increasing thickness is due to the increasing stopping power of the CPB layer, thereby due to more fast photons contributing to the time response. A rough estimate allowed us to determine that layer thickness of 1, 8, 20, and 50 μm of CPB can stop about 5, 33, 64, and 92 % of X-rays, respectively. These values were obtained considering the density of CPB bulk crystal (Section 9.3.3) and the mass attenuation coefficient at 10 keV (the peak energy of the X-ray spectrum), obtained from the NIST XCOM database [153] $\mu_m = 104.9\,\mathrm{cm}^2/\mathrm{g}$. It should be emphasized that these

values are overestimates since, as mentioned before, the considered density refers to bulk CPB crystal, while the density of nanocrystals is lower. Moreover, the X-ray energy distribution has a tail extending up to 40 keV due to bremsstrahlung radiation. Despite these values are just rough estimates, they give an idea of the variation in stopping power with the increasing thickness.

The difference between the DTR of heterostructure units and that of solely CPB ($\approx$ 240 vs 196 ps) is due to the fraction of X-ray interacting in the bulk crystal and still contributing to the overall time resolution. We can see this effect in the experiment with different thicknesses: with only 1 μm thick CPB, stopping less than 5 % of the incoming X-rays, the time delay distribution shows a long tail due to GAGG contribution. To quantify this effect we evaluated the full-width-at-tenth-maximum (FWTM), which strongly decreases with increasing CPB thickness and also saturates with a layer thicker than about 10 μm.

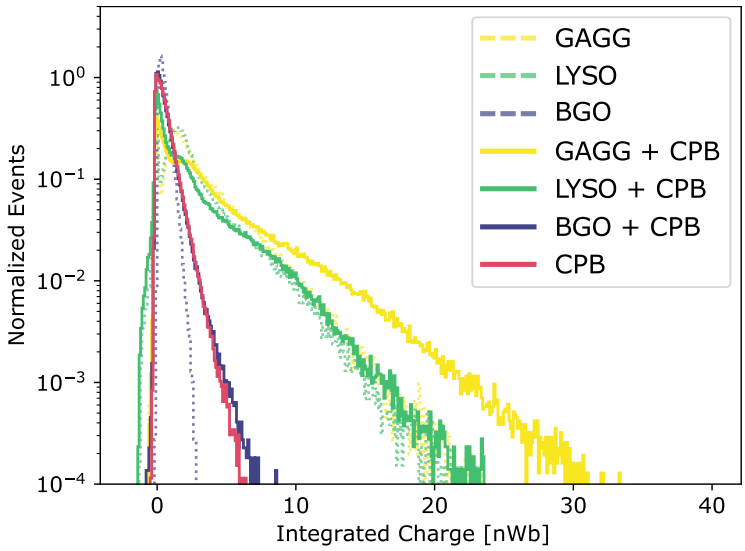

Figure 9.9: Integrated charge distribution under X-ray irradiation of the different samples measured: GAGG, LYSO, and BGO (yellow, green, and blue, respectively) without and with CPB layer (dotted and solid lines, respectively) and only CPB (red).

Figure 9.9 shows the energy spectrum of GAGG, LYSO, and BGO without and with the CPB layer and that of stand-alone CPB nanocrystals. It is interesting to note that in the heterostructure units, where a fraction of X-ray is interacting with the CPB layer, we do not observe a loss in the collected light. Stand-alone CPB has higher light output than solely BGO, but lower than solely GAGG and LYSO, and the heterostructure units showed comparable (LYSO) or higher (BGO and GAGG) light output compared to the corresponding solely single crystal plates. This effect was already observed by Děcká et al [150]. While it cannot be explained by the simple sum of the two contributing materials, it can be due to surface effects. The scintillation light produced by the bulk crystal and emitted in the opposite direction to the photodetector is probably scattered back from the nanocrystals. The effect could be less visible for LYSO as most of its emission spectrum (peaked at 420 nm) is positioned below the absorption edge of CPB nanocrystals (see the absorption spectra of CPB nanocrystals in Figure 9.3).

9.3.5 Proof of concept of Heterostructure with CPB and GAGG

The coincidence time resolution (CTR) of CPB deposited on a GAGG plate was also measured under 511 keV γ-ray excitation. GAGG was chosen over BGO and LYSO for this study as CPB is mostly transparent to its emission wavelengths, while this is not the case for the other two crystals. In X-ray measurements, this was not a problem, as the CPB was not in between the crystal and the photodetector unlike in the case of 511 keV γ-ray excitation (compare Figure 9.2 (b) and (c)). The reason of this configuration is to exploit the energy sharing mechanism and maximize the energy deposited in CPB, thereby the number of fast photons produced.

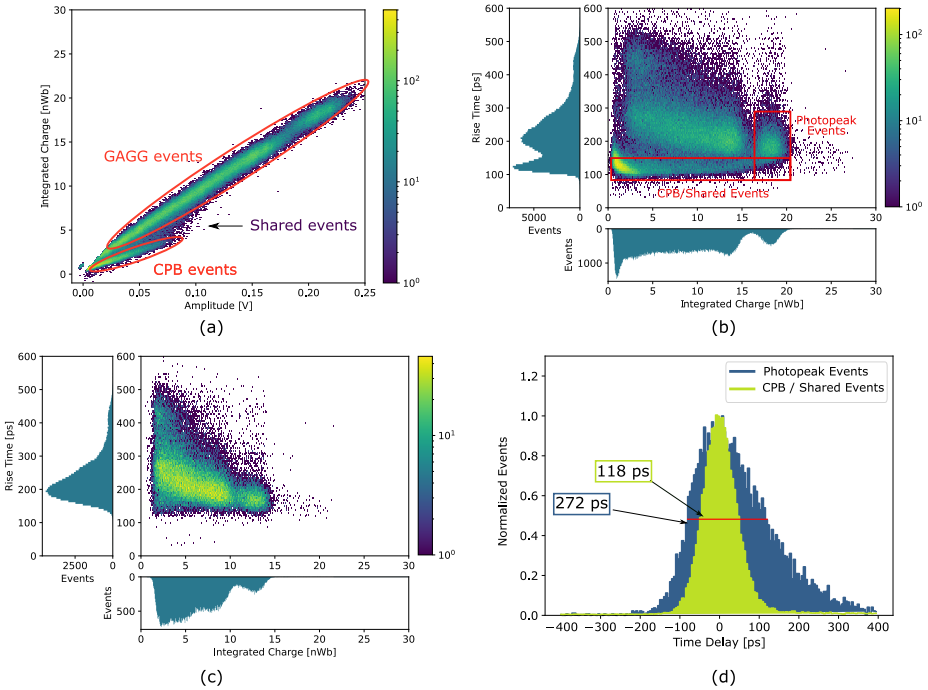

Figure 9.10: Energy sharing between GAGG and CPB under 511 keV. (a) 2D histogram showing the correlation between the integrated charge and amplitude of the signal. (b) 2D histogram showing the correlation between the signal rise time and the integrated charge, together with the projection of the individual distribution. (c) 2D histogram showing the correlation between the signal rise time and the integrated charge for only GAGG plate. (d) Time delay distibution of the photopeak and CPB/shared events and their associated FWHM values.

GAGG and CPB have different light output and decay kinetics. This is reflected by a different pulse shape, and the amplitude and the integrated charge of the pulse allow us to distinguish the events depending on the material where the energy is deposited (Figure 9.10 (a)), as it illustrated for BGO and EJ232 in Section 4.3. However, unlikely from BGO and EJ232 the separation is not so well defined. Moreover, not being able to estimate the energy deposited in CPB, the coordinates transformation and energy calibration described in Section 4.3 could not be applied.

Another possibility to classify the events consists of looking at the signal rise time, defined as the time interval between when the signal crosses two fixed thresholds (Figure 6.4). In Figure 9.10 (b), the correlation between the signal rise time and the integrated charge is shown. We can observe two peaks in the signal rise time distribution: one centered around 200 ps which also corresponds to the majority of photopeak events (peak at about 18 nWb in the integrated charge distribution). The second and sharper peak is centered around 120 ps. Most of these events have a low integrated charge (see the sharp peak at about 1 nWb), but we observe a long tail extending along all the charge distribution. These are events shared or depositing energy only in CPB. A similar feature was also observed for BGO and EJ232 (see Section 6.2.3). As confirmation of this deduction, GAGG only was measured as a comparison by coupling it directly to the SiPM. Figure 9.10 (c) shows the same correlation between signal rise time and integrated charge for GAGG only and we can see how, without CPB, only the peak centered around 200 ps is present.

The selection was therefore performed on the signal rise time and integrated charge, distinguishing between photopeak events and CPB/shared events, as shown by the red boxes in Figure 9.10 (b). A CTR of 272 ps and 118 ps was obtained for the two categories respectively. It is important to note that the twofold improvement would be even greater if we were selecting only shared photopeak events. However, their identification is not straightforward for this specific case and it was decided to select events depositing at least part of the energy in CPB according to the signal rise time, without imposing any constraint on the amount of total energy deposited.

This measurement constitutes a successful proof of concept of how CPB can be coupled to bulk scintillators to enhance their timing performance also at high (511 keV) energy. However, further optimization from the material standpoint is needed to incorporate CPB in a full (multi-layer) heterostructure.

An attempt of full $3\times3\times3$ [3] heterostructure was assembled by stacking GAGG plates with a CPB layer deposited on top, but only the GAGG signal was observable in this case. The explanation relies on the different measurement conditions (see Figure 9.2) and the high self-absorption from CPB. When measuring the single heterostructure unit, the light produced in the CPB layer needs to cross only a few tens of micrometers, while in the full heterostructure it needs to travel up to 3 mm.

Moreover, it is not feasible to obtain such a structure on a large scale with CPB in solution, and its embedding in a host matrix is the most reasonable solution. However, the present embedding techniques do not allow for reaching high concentrations of CPB nanocrystals while keeping the sample transparent. Some tests were also performed using the CPB sample embedded in polystyrene with 10 % NCs concentration (both in the configuration of a single unit or full heterostructure) but also, in this case, the signal of CPB was not detectable. To pursue this R&D line, new candidates as host matrix (e.g. glass instead of polystyrene because of its higher density and better radiation hardness) and embedding techniques will be considered.

9.4 Summary and Conclusion

In this chapter, the timing capabilities of $CsPbBr_3$ (CPB) nanocrystals (NCs) were explored. The CPB samples were synthesized at the Czech Technical University (CTU) in Prague and tested at CERN, both in the form of thin films (solution of free nanocrystals drop-casted on top of glass, bulk scintillator, or SiPM according to the application) and embedded in polystyrene.

Part of the study was focused on comparing two different surface ligands, oleic acid and oleylamine (OA+OAm) and didodecylammonium bromide (DDAB). Photoluminescence, radioluminescence, and decay kinetics measurements allowed us to confirm that, as expected, the DDAB ligand better prevents nanoparticles from aggregation.

The decay kinetics and time resolution under soft X-ray excitation with the experimental setups described in Chapter 9 were measured for all the synthesized CPB samples: the two sets (DDAB and OA+OAm) of CPB embedded in polystyrene (CPB@PS) with different NCs concentration (1, 5, 10 %) and free CPB NCs. All samples showed ultra-fast decay kinetics with a percentage of photons produced in the first nanosecond ranging between 30 and 50 %. This fast decay kinetics reflected into a time resolution at 10-15 keV ranging from 200 ps (free CPB) to 330 ps (CPB@PS), showing therefore better timing capabilities than fast plastic scintillators like EJ232 and BC422 (Chapter 9).

Nevertheless, due to the low stopping power, CPB cannot be used as a stand-alone detector for either γ or X-ray radiation. Proof of concepts of heterostructures using bulk, dense scintillators were tested both under X-ray and 511 keV irradiation.

For time resolution measurements under X-ray excitation, CPB thin films were fabricated on top of BGO, LYSO, and GAGG bulk scintillator plates. The CPB thin film significantly improved the performance of respective bulk scintillators, reaching values around 240 ps regardless of the type of the bulk scintillator. This improvement scaled with the amount of deposited nanocrystals negligibly above a certain layer thickness, suggesting that an economic-friendly optimum between the detector cost and performance can be reached. Already the thinnest tested layer, about 1 μm thick, resulted in acceleration of time resolution from 2.4 ns of solely GAGG to about 400 ps. The effect saturated after reaching about 10 μm thick layer and achieving 270-230 ps.

These results show the potential of CPB as a time-enhancing coating layer to be applied to bulk dense scintillators in the framework of TOF X-ray imaging, where more than half of the energies used should already be covered by these proof-of-concept samples. The energy range of TOF X-ray technique is 20–120 keV and, by extrapolation of the obtained results at about 10 keV, the required sub-100 ps time resolution should already be reached at 60 keV ($240\,\text{ps} \cdot \sqrt{10\,\text{keV}/60\,\text{keV}}$).

The test under 511 keV γ-ray excitation was performed using a heterostructure unit comprising of GAGG and CPB. It revealed that the identification of shared events led to more than twofold improvement in time resolution compared to that of solely GAGG, almost reaching 100 ps. This result paves the way for the investigation of this material for a wide range of applications, also using energies above a few hundred keV, from TOF-PET to HEP.

In conclusion, these results suggest the high application potential of CPB to significantly increase the temporal resolution performance of the detector at

different energy ranges. Future work will focus on finding the most suitable matrix and embedding technique to achieve high NC concentration while preserving the transparency of the sample. This step will allow for a large-scale multilayer heterostructure, as more elements will be required to efficiently stop high-energy radiation.

Part V

Conclusion and Outlook

Conclusion and Outlook

Summary

This thesis work investigates a new detector technology for TOF-PET, proposed to overcome the dichotomy between high sensitivity and ultra-fast timing. Heterostructured scintillators consist of combining two materials having complementary properties (i.e., high stopping power for 511 keV γ-ray and high photon time density) and benefit from both through the mechanism of energy sharing. The annihilation γ-ray interacts via photoelectric absorption in the heavy material and, with appropriate arrangements on the geometry, the recoil photoelectron is likely to escape and deposit part of its energy in the fast material. The events resulting from energy deposition in both materials, the so-called *shared events*, boost the overall timing performance of the detector.

The first part of this study aims to gain a thorough understanding of this technology, with its fundamental properties and limitations. To this end, a simple configuration made of alternating layers of Bismuth Germanate (BGO, effective atomic number $Z_{\text{eff}} = 73$) and EJ232 plastic scintillator (effective decay time $\tau_{\text{eff}} = 1.5\,\text{ns}$) was considered. BGO and EJ232 are a good combination because they have similar light yield but the decay kinetics of EJ232 is a factor 100 faster than BGO. This simplifies the identification of shared events and limits the degradation of energy resolution inherent in these layered structures.

The optimization of BGO and plastic heterostructures started with the investigation of the energy sharing mechanism. Monte Carlo simulations were performed with the Geant4 toolkit, and the photofraction and energy sharing probability were studied as a function of the thickness of plastic. The thickness of BGO was fixed at 100 μm – approximately the average distance traveled in BGO by a 511 keV electron – to maximize the probability for the photoelectron escaping from it to the fast scintillator. Two configurations were chosen: layers of 100 μm thickness for both BGO and EJ232 (1:1) and layers of 100 μm thickness for BGO and 200 μm thickness for EJ232 (1:2). The former resulted in a photofraction comparable to lutetium-yttrium orthosilicate (LYSO), the current state-of-the-art in TOF-PET detectors. The latter, with its larger energy sharing probability and average energy deposited in plastic, allowed to investigate the best achievable timing.

A method to developed events classification based on pulse shape discrimination was performed, allowing for distinguishing the events based on the amount of energy deposited in each material. This made it possible to study the decay kinetics of heterostructures as a function of the energy deposited in EJ232, and to experimentally verify that the scintillation kinetics of heterostructure is given

by the linear combination of the scintillation kinetics of its constituent materials.

The coincidence time resolution (CTR) was measured for both the two configurations chosen and compared to pure BGO, using Broadcom NUV-HD SiPMs and high-frequency electronic readout. A CTR of 271±14 ps and 303±15 ps were measured for a 3×3×15 mm^3 bulk BGO and layered BGO, respectively. The layered BGO, a stack of 100 μm thick BGO layers, was studied to disentangle the effects due to the layering of the pixel and the combination of different materials. Both layered BGO and the heterostructures were hand-assembled in the laboratory at CERN. The 1:1 and 1:2 heterostructures resulted in a CTR of 239±12 ps and 197±10 ps, respectively, showing an improvement of 12% and 28% compared to bulk BGO. Even larger improvement was observed when selecting only photopeak events with at least 50 keV deposited in EJ232, achieving up to 173±9 ps with the 1:2 configuration.

For both configurations, 3×3×3 mm^3 pixels were also measured, allowing for the investigation of the impact of depth-of-interaction (DOI) uncertainties and the experimental verification of a simplified analytic model describing it.

The CTR measurements together with those on the scintillation kinetics enabled us to verify that the CTR analytical model developed for bulk scintillators also applies to heterostructured scintillators. As this model accounts for the scintillation kinetics of the materials, their light yield, the photon time spread, and the light transfer efficiency to the photodetector, its applicability to heterostructures can accelerate the search for materials that can further push the timing performance of heterostructures.

Finally, the investigation of BGO and EJ232 concluded with the evaluation of CTR performance in double-sided readout with high-frequency front-end electronics. Two industrially produced heterostructures purchased from the CPI company were used for this study. To achieve higher sensitivity and simplify the assembly, a different configuration was chosen: a length of 20 mm and layer thickness of 250 μm for both BGO and EJ232. Compared to single-sided readout (SSR), the DSR allows for larger light collection and intrinsically compensates for DOI uncertainties. It was shown that the simple average of the timestamps of back and front SiPMs is enough to minimize the DOI blurring, without the need to apply off-line corrections. Two different SiPM technology from Broadcom were tested, NUV-HD and NUV-MT. The latter is the most recently developed and, being characterized by low internal cross-talk probability, enables the use of high overvoltage to reach an unprecedented gain. Measuring the two heterostructures coupled to NUV-MT SiPM in symmetrical configuration, the CTR was improved from 270±8 ps (SSR) to 239±8 ps (DSR) when considering all photopeak events, and from 181±6 ps (SSR) to 136±5 ps (DSR) when considering only photopeak events with at least 50 keV deposited in plastic.

The second part of this dissertation takes the first steps toward the next generation of heterostructures, in which plastic aims to be replaced by materials that exhibit even higher photon time density. To date, the best candidates for this purpose are nanocrystal scintillators, since, benefiting from quantum confinement effects, they can exhibit high intrinsic light output and sub-nanosecond decay kinetics. The main disadvantages of these materials are their lack of volume to effectively block incoming radiation and their small Stokes shift, which prevents efficient light extraction.

The first challenge in their use consists therefore in a proper characterization of their properties as radiation detectors for timing applications, namely the light

output and time resolution. To address this limitation, an experimental setup was developed to simultaneously measure the light output and time resolution under pulsed X-ray excitation. This setup with its associated method was first verified using standard bulk inorganic and organic materials, and then successfully tested on nanoscintillators.

The full characterization and first proof of concept of heterostructure using lead halide perovskite ($CsPbBr_3$) nanocrystals was presented. They were studied both in the form of free nanocrystals in solution and embedded in polystyrene. The former gave the best performances, because enables the use of almost 100 % concentration of nanocrystal in very thin layers (about 50 μm). Free $CsPbBr_3$ nanocrystals show a time resolution of 196±6 ps under X-ray (mean energy 15 keV) excitation which, by scaling for the energy and with proper assumptions, translates into a potential CTR of 43 ps at 511 keV.

A thin layer of $CsPbBr_3$ was deposited on inorganic bulk crystal plates (BGO, GAGG, and LYSO) and they were proved to significantly boost (up to a factor 10) their timing performances. These results under X-ray excitation also highlighted the potential of both $CsPbBr_3$ and the heterostructure concept in other medical imaging techniques, such as TOF-CT.

Finally, the heterostructure proof-of-concept with GAGG and $CsPbBr_3$ was also tested under 511 keV irradiation. The signals coming from events depositing at least part of the energy in $CsPbBr_3$ were clearly identifiable and led to a twofold improvement compared to only GAGG.

The principal conclusion of this dissertation is the deep understanding of the heterostructure concept, with the development and experimental verification of simple analytic models describing the scintillation kinetics, CTR, and DOI contribution of this technology. Using the state-of-the-art SiPM and readout electronics technology a sub-200 ps CTR was achieved for 20 mm long BGO-EJ232 heterostructures. In parallel, an experimental setup was developed to guide the progress of nanoscintillators that could replace plastic and further enhance the performance of heterostructures, and the first promising results with $CsPbBr_3$ were shown.

Outlook

Complementary to the optimizations of the performances at the level of a single pixel, for heterostructures to become a competitive alternative to the current state of the art, the feasibility of their implementation at the system level needs to be explored.

The method based on pulse shape discrimination developed for events classification works particularly well with BGO and EJ232 because of their similar light yield but different decay kinetics. It was further enabled by the front-end electronics used which gives analog signal for both the energy and timing channel, allowing for pulse shape discrimination and the time walk correction based on the time signal rise time. The performance of heterostructures with readout electronics more suitable for system-level scalability [10, 154] needs to be tested, and different features for the events classification, instead of amplitude and integral of the energy analog signal, should be investigated.

To date, only heterostructured single pixels were measured. A TOF-PET DOI module of heterostructures, i.e. a matrix of 4×4 heterostructures coupled to an array of SiPM on one side and to a light guide on the opposite one to enable light sharing and DOI information retrieval [126], is foreseen to be tested soon. Because this method allows for correcting for the DOI uncertainty contribution, we expect similar results to those obtained for the single pixel measured in DSR configuration.

Moreover, simulation works are being performed evaluating the impact of heterostructures directly on the reconstructed image [91]. The most promising approach is the multi-kernel one, as in heterostructures events with different energy sharing between the two materials result in different TOF-kernel.

To conclude, although there is still a long way to go, the heterostructure approach seems to be a viable solution for the trade-off between high sensitivity and fast time in TOF-PET, and there is a very active line of research in this direction.

Bibliography

[1] M. Conti, "State of the art and challenges of time-of-flight PET," *Physica Medica*, vol. 25, no. 1, pp. 1–11, 2009.

[2] "The 10 ps challenge website." https://the10ps-challenge.org, Last update 2020.

[3] "Biograph vision.x pet/ct scanner." https://www.siemens-healthineers.com/en-us/press-room/press-releases/biograph-vison-x-pet-ct-scanner-debut, 2023.

[4] S. Gundacker, E. Auffray, K. Pauwels, and P. Lecoq, "Measurement of intrinsic rise times for various L(Y)SO and LuAG scintillators with a general study of prompt photons to achieve 10 ps in TOF-PET," *Physics in Medicine & Biology*, vol. 61, no. 7, p. 2802, 2016.

[5] S. Gundacker, R. M. Turtos, N. Kratochwil, R.-H. Pots, M. Paganoni, P. Lecoq, and E. Auffray, "Experimental time resolution limits of modern sipms and TOF-PET detectors exploring different scintillators and Cherenkov emission," *Physics in Medicine & Biology*, vol. 65, no. 2, p. 025001, 2020.

[6] F. Nolet, F. Dubois, N. Roy, S. Parent, W. Lemaire, A. Massie-Godon, S. A. Charlebois, R. Fontaine, and J.-F. Pratte, "Digital sipm channel integrated in cmos 65 nm with 17.5 ps fwhm single photon timing resolution," *Nuclear Instruments and Methods in Physics Research Section A: Accelerators, Spectrometers, Detectors and Associated Equipment*, vol. 912, pp. 29–32, 2018.

[7] A. Gola, F. Acerbi, M. Capasso, M. Marcante, A. Mazzi, G. Paternoster, C. Piemonte, V. Regazzoni, and N. Zorzi, "Nuv-sensitive silicon photomultiplier technologies developed at fondazione bruno kessler," *Sensors*, vol. 19, no. 2, p. 308, 2019.

[8] S. Merzi, S. E. Brunner, A. Gola, A. Inglese, A. Mazzi, G. Paternoster, M. Penna, C. Piemonte, and M. Ruzzarin, "Nuv-hd sipms with metal-filled trenches," *Journal of Instrumentation*, vol. 18, no. 05, p. P05040, 2023.

[9] S. Gundacker, R. M. Turtos, E. Auffray, M. Paganoni, and P. Lecoq, "High-frequency sipm readout advances measured coincidence time resolution limits in TOF-PET," *Physics in Medicine & Biology*, vol. 64, no. 5, p. 055012, 2019.

[10] S. Gómez, J. Fernández-Tenllado, J. Alozy, M. Campbell, R. Manera, J. Mauricio, A. Mariscal, C. Pujol, D. Sánchez, A. Sanmukh, *et al.*, "Fastic: A highly configurable asic for fast timing applications," pp. 1–4, 2021.

[11] S. Pourashraf, A. Gonzalez-Montoro, J. Y. Won, M. S. Lee, J. W. Cates, Z. Zhao, J. S. Lee, and C. S. Levin, "Scalable electronic readout design for a 100 ps coincidence time resolution TOF-PET system," *Physics in Medicine & Biology*, vol. 66, no. 8, p. 085005, 2021.

[12] S. Enoch, A. Gola, P. Lecoq, and A. Rivetti, "Design considerations for a new generation of sipms with unprecedented timing resolution," *Journal of Instrumentation*, vol. 16, no. 02, p. P02019, 2021.

[13] S. Brunner and D. Schaart, "BGO as a hybrid scintillator/Cherenkov radiator for cost-effective time-of-flight PET," *Physics in Medicine & Biology*, vol. 62, no. 11, p. 4421, 2017.

[14] G. Ariño-Estrada, E. Roncali, A. R. Selfridge, J. Du, J. Glodo, K. S. Shah, and S. R. Cherry, "Study of čerenkov light emission in the semiconductors tlbr and tlcl for TOF-PET," *IEEE Transactions on Radiation and Plasma Medical Sciences*, 2020.

[15] N. Kratochwil, S. Gundacker, and E. Auffray, "A roadmap for sole Cherenkov radiators with sipms in TOF-PET," *Physics in Medicine & Biology*, vol. 66, no. 19, p. 195001, 2021.

[16] G. Terragni, M. Pizzichemi, E. Roncali, S. R. Cherry, J. Glodo, K. Shah, G. Ariño-Estrada, E. Auffray, A. Ghezzi, and N. Kratochwil, "Time resolution studies of thallium based cherenkov semiconductors," *Frontiers in Physics*, vol. 10, p. 93, 2022.

[17] R. Pots, E. Auffray, and S. Gundacker, "Exploiting cross-luminescence in BaF2 for ultrafast timing in radiation detection using hpk-vuv sipms," *Frontiers in Physics*, vol. 8, p. 482, 2020.

[18] S. Gundacker, R. Pots, A. Nepomnyashchikh, E. Radzhabov, R. Shendrik, S. Omelkov, M. Kirm, F. Acerbi, M. Capasso, G. Paternoster, *et al.*, "Vacuum ultraviolet silicon photomultipliers applied to BaF2 cross-luminescence detection for high-rate ultrafast timing applications," *Physics in Medicine & Biology*, vol. 66, no. 11, p. 114002, 2021.

[19] V. Vaněček, J. Páterek, R. Král, R. Kučerková, V. Babin, J. Rohlíček, R. Cala, N. Kratochwil, E. Auffray, and M. Nikl, "Ultraviolet cross-luminescence in ternary chlorides of alkali and alkaline-earth metals," *Optical Materials: X*, vol. 12, p. 100103, 2021.

[20] S. Omelkov, V. Nagirnyi, A. Vasil, M. Kirm, *et al.*, "New features of hot intraband luminescence for fast timing," *Journal of Luminescence*, vol. 176, pp. 309–317, 2016.

[21] R. Turtos *et al.*, "On the use of cdse scintillating nanoplatelets as time taggers for high-energy gamma detection," *npj 2D Materials and Applications*, vol. 3, no. 1, pp. 1–10, 2019.

[22] K. Tomanová, V. Čuba, M. G. Brik, E. Mihóková, R. Martinez Turtos, P. Lecoq, E. Auffray, and M. Nikl, "On the structure, synthesis, and characterization of ultrafast blue-emitting cspbbr3 nanoplatelets," *APL Materials*, vol. 7, no. 1, p. 011104, 2019.

[23] K. Děcká, J. Král, F. Hájek, P. Průša, V. Babin, E. Mihóková, and V. Čuba, "Scintillation response enhancement in nanocrystalline lead halide perovskite thin films on scintillating wafers," *Nanomaterials*, vol. 12, no. 1, p. 14, 2022.

[24] G. Toci, L. A. Gizzi, P. Koester, F. Baffigi, L. Fulgentini, L. Labate, A. Hospodkova, V. Jary, M. Nikl, and M. Vannini, "InGaN/GaN multiple quantum well for superfast scintillation application: Photoluminescence measurements of the picosecond rise time and excitation density effect," *Journal of Luminescence*, vol. 208, pp. 119–124, 2019.

[25] J. Perego, I. Villa, A. Pedrini, E. Padovani, R. Crapanzano, A. Vedda, C. Dujardin, C. X. Bezuidenhout, S. Bracco, P. Sozzani, *et al.*, "Composite fast scintillators based on high-z fluorescent metal–organic framework nanocrystals," *Nature Photonics*, vol. 15, no. 5, pp. 393–400, 2021.

[26] "ERC advanced grant TICAL GA:338953, PI: P. lecoq,"

[27] R. M. Turtos, S. Gundacker, E. Auffray, and P. Lecoq, "Towards a metamaterial approach for fast timing in PET: experimental proof-of-concept," *Physics in Medicine & Biology*, vol. 64, no. 18, p. 185018, 2019.

[28] G. de Hevesy, "Some applications of isotopic indicators," *Nobel Lecture*, vol. 12, 1944.

[29] A. Del Guerra, N. Belcari, and M. Bisogni, "Positron emission tomography: its 65 years," *La Rivista del Nuovo Cimento*, vol. 39, pp. 155–223, 2016.

[30] J. Radon, "On the determination of functions from their integral values along certain manifolds," *IEEE transactions on medical imaging*, vol. 5, no. 4, pp. 170–176, 1986.

[31] S. Gundacker, *Time resolution in scintillator based detectors for positron emission tomography*. PhD thesis, 2014.

[32] M. Lubberink, R. Boellaard, A. P. Van Der Weerdt, F. C. Visser, and A. A. Lammertsma, "Quantitative comparison of analytic and iterative reconstruction methods in 2-and 3-dimensional dynamic cardiac 18f-fdg pet," *Journal of Nuclear Medicine*, vol. 45, no. 12, pp. 2008–2015, 2004.

[33] Y. Vardi, L. A. Shepp, and L. Kaufman, "A statistical model for positron emission tomography," *Journal of the American statistical Association*, vol. 80, no. 389, pp. 8–20, 1985.

[34] C. D. Anderson and S. H. Neddermeyer, *The Production and Properties of Positrons...*, vol. 46. PA Norstedt & söner, 1937.

[35] E. O. Lawrence, "The evolution of the cyclotron," *Nobel Lecture*, 1951.

[36] B. K. Lubsandorzhiev, "On the history of photomultiplier tube invention," *Nuclear Instruments and Methods in Physics Research Section A: Accelerators, Spectrometers, Detectors and Associated Equipment*, vol. 567, no. 1, pp. 236–238, 2006.

[37] R. Hofstadter, "The detection of gamma-rays with thallium-activated sodium iodide crystals," *Physical Review*, vol. 75, no. 5, p. 796, 1949.

[38] W. Sweet, "Localization of brain tumors with positron emitters," *Nucleonics*, vol. 11, pp. 40–45, 1953.

[39] M. E. Phelps, E. J. Hoffman, N. A. Mullani, and M. M. Ter-Pogossian, "Application of annihilation coincidence detection to transaxial reconstruction tomography," *Journal of nuclear medicine*, vol. 16, no. 3, pp. 210–224, 1975.

[40] E. J. Hoffman, M. E. Phelps, N. A. Mullani, C. S. Higgins, and M. M. Ter-Pogossian, "Design and performance characteristics of a whole-body positron transaxial tomograph," *Journal of Nuclear Medicine*, vol. 17, no. 6, pp. 493–502, 1976.

[41] Y. L. Yamamoto, C. J. Thompson, E. Meyer, J. S. Robertson, and W. Feindel, "Dynamic positron emission tomography for study of cerebral hemodynamics in a cross section of the head using positron-emitting 68ga-edta and 77kr," *Journal of computer assisted tomography*, vol. 1, no. 1, pp. 43–56, 1977.

[42] C. Melcher and J. Schweitzer, "A promising new scintillator: cerium-doped lutetium oxyorthosilicate," *Nuclear Instruments and Methods in Physics Research Section A: Accelerators, Spectrometers, Detectors and Associated Equipment*, vol. 314, no. 1, pp. 212–214, 1992.

[43] M. Casey and R. Nutt, "A multicrystal two dimensional bgo detector system for positron emission tomography," *Ieee transactions on nuclear science*, vol. 33, no. 1, pp. 460–463, 1986.

[44] J. Van Sluis, J. De Jong, J. Schaar, W. Noordzij, P. Van Snick, R. Dierckx, R. Borra, A. Willemsen, and R. Boellaard, "Performance characteristics of the digital biograph vision PET/CT system," *Journal of Nuclear Medicine*, vol. 60, no. 7, pp. 1031–1036, 2019.

[45] "Crystal clear collaboration." https://crystalclearcollaboration.web.cern.ch, 1990.

[46] T. C. Collaboration, "The cms electromagnetic calorimeter project: Technical design report," *Geneva: CERN*, 1997.

[47] G. Bayatian, "Cms technical design report, volume ii: Physics performance," *J. Phys. G*, vol. 34, no. CERN-LHCC-2006-021; CMS-TDR-008-2; FERMILAB-CONF-07-831-CMS, 2007.

[48] A. Fremout, S. Tavernier, and P. Bruyndonckx, "The clear pet project: development of a second generation small animal pet scanner," in *submitted to Hires 2001, Washington USA*, 2001.

[49] M. Abreu, P. Almeida, F. Balau, N. Ferreira, F. Fraga, M. Martins, N. Matela, R. Moura, C. Ortigao, L. Peralta, *et al.*, "Clear-pem: a dedicated pet camera for improved breast cancer detection," *Radiation protection dosimetry*, vol. 116, no. 1-4, pp. 208–210, 2005.

[50] G. Cucciati, E. Auffray, R. Bugalho, L. Cao, N. Di Vara, F. Farina, N. Felix, B. Frisch, A. Ghezzi, V. Juhan, *et al.*, "Development of clearpem-sonic, a multimodal mammography system for pet and ultrasound," *Journal of Instrumentation*, vol. 9, no. 03, p. C03008, 2014.

[51] N. Aubry, E. Auffray, F. Mimoun, N. Brillouet, R. Bugalho, E. Charbon, O. Charles, D. Cortinovis, P. Courday, A. Cserkaszky, *et al.*, "Endotofpet-us: a novel multimodal tool for endoscopy and positron emission tomography," *Journal of Instrumentation*, vol. 8, no. 04, p. C04002, 2013.

[52] M. Conti, "Focus on time-of-flight PET: the benefits of improved time resolution," *European journal of nuclear medicine and molecular imaging*, vol. 38, no. 6, pp. 1147–1157, 2011.

[53] D. L. Snyder, L. J. Thomas, and M. M. Ter-Pogossian, "A matheematical model for positron-emission tomography systems having time-of-flight measurements," *IEEE Transactions on Nuclear Science*, vol. 28, no. 3, pp. 3575–3583, 1981.

[54] M. Conti, "State of the art and challenges of time-of-flight PET," *Physica Medica*, vol. 25, no. 1, pp. 1–11, 2009.

[55] S. Strother, M. Casey, and E. Hoffman, "Measuring pet scanner sensitivity: relating countrates to image signal-to-noise ratios using noise equivalents counts," *Ieee transactions on nuclear science*, vol. 37, no. 2, pp. 783–788, 1990.

[56] R. D. Badawi, H. Shi, P. Hu, S. Chen, T. Xu, P. M. Price, Y. Ding, B. A. Spencer, L. Nardo, W. Liu, *et al.*, "First human imaging studies with the explorer total-body pet scanner," *Journal of Nuclear Medicine*, vol. 60, no. 3, pp. 299–303, 2019.

[57] W. W. Moses, "Fundamental limits of spatial resolution in pet," *Nuclear Instruments and Methods in Physics Research Section A: Accelerators, Spectrometers, Detectors and Associated Equipment*, vol. 648, pp. S236–S240, 2011.

[58] R. D. Evans and R. Evans, "The atomic nucleus," 1955.

[59] W. G. Kreyling, M. Semmler-Behnke, and Q. Chaudhry, "A complementary definition of nanomaterial," *Nano today*, vol. 5, no. 3, pp. 165–168, 2010.

[60] A. P. Alivisatos, "Semiconductor clusters, nanocrystals, and quantum dots," *science*, vol. 271, no. 5251, pp. 933–937, 1996.

[61] C. Dujardin, D. Amans, A. Belsky, F. Chaput, G. Ledoux, and A. Pillonnet, "Luminescence and scintillation properties at the nanoscale," *IEEE Transactions on Nuclear Science*, vol. 57, no. 3, pp. 1348–1354, 2010.

[62] V. Vaněček, K. Děcká, E. Mihóková, V. Čuba, R. Král, and M. Nikl, "Advanced halide scintillators: From the bulk to nano," *Advanced Photonics Research*, vol. 3, no. 8, p. 2200011, 2022.

[63] A. Credi, *Photoactive Semiconductor Nanocrystal Quantum Dots: Fundamentals and Applications*. Springer, 2017.

[64] K. Děcká, *Synthesis of scintillating metamaterials based on cesium lead halide nanoparticles*. PhD thesis, 2022.

[65] D. Vaisburd and S. Kharitonova, "Two types of fundamental luminescence of ionization-passive electrons and holes in optical dielectrics—intraband-electron and interband-hole luminescence (theoretical calculation and comparison with experiment)," *Russian physics journal*, vol. 40, no. 11, pp. 1037–1060, 1997.

[66] C. Van Eijk, "Cross-luminescence," *Journal of luminescence*, vol. 60, pp. 936–941, 1994.

[67] I. Frank and I. Tamm, "Coherent visible radiation of fast electrons passing through matter," pp. 29–35, 1991.

[68] S. Brunner, L. Gruber, J. Marton, K. Suzuki, and A. Hirtl, "Studies on the cherenkov effect for improved time resolution of tof-pet," *IEEE Transactions on Nuclear Science*, vol. 61, no. 1, pp. 443–447, 2013.

[69] P. Lecoq, "Metascintillators: New results for TOF-PET applications," 2021.

[70] G. F. Knoll, *Radiation detection and measurement*. John Wiley & Sons, 2010.

[71] D. Renker and E. Lorenz, "Advances in solid state photon detectors," *Journal of Instrumentation*, vol. 4, no. 04, p. P04004, 2009.

[72] "Introduction to the silicon photomultiplier – application notes." https://www.onsemi.com/pub/Collateral/AND9770-D.PDF.

[73] S. Gundacker, A. Knapitsch, E. Auffray, P. Jarron, T. Meyer, and P. Lecoq, "Time resolution deterioration with increasing crystal length in a tof-pet system," *Nuclear Instruments and Methods in Physics Research Section A: Accelerators, Spectrometers, Detectors and Associated Equipment*, vol. 737, pp. 92–100, 2014.

[74] R. F. Post and L. I. Schiff, "Statistical limitations on the resolving time of a scintillation counter," *Phys. Rev.*, vol. 80, pp. 1113–1113, Dec 1950.

[75] B. Sigfridsson, "Theoretical analysis of time resolution in scintillation detectors," *Nuclear Instruments and Methods*, vol. 54, no. 1, pp. 13–28, 1967.

[76] F. Loignon-Houle, *Étude des limites de résolution temporelle de détecteurs pour la tomographie d'émission par positrons avec temps de vol*. PhD thesis, 2023.

[77] S. Vinogradov, "Approximations of coincidence time resolution models of scintillator detectors with leading edge discriminator," *Nuclear Instruments and Methods in Physics Research Section A: Accelerators, Spectrometers, Detectors and Associated Equipment*, vol. 912, pp. 149–153, 2018.

[78] R. Bock, T. Hansl-Kozanecka, and T. Shah, "Parametrization of the longitudinal development of hadronic showers in sampling calorimeters," *Nuclear Instruments and Methods in Physics Research*, vol. 186, no. 3, pp. 533–539, 1981.

[79] G. Grindhammer and S. Peters, "The parameterized simulation of electromagnetic showers in homogeneous and sampling calorimeters," *arXiv preprint hep-ex/0001020*, 2000.

[80] P. Krause, E. Rogers, M. D. Birowosuto, Q. Pei, E. Auffray, A. Vasil'ev, and G. Bizarri, "Design rules for time of flight positron emission tomography (ToF-PET) heterostructure radiation detectors," *Available at SSRN 3966915*, 2021.

[81] F. Pagano, N. Kratochwil, M. Salomoni, M. Pizzichemi, M. Paganoni, and E. Auffray, "Advances in heterostructured scintillators: Toward a new generation of detectors for tof-pet," *Physics in Medicine & Biology*, vol. 67, no. 13, p. 135010, 2022.

[82] Saint-Gobain, "Bc422 data-sheet," 2022.

[83] P. Lecoq, G. Konstantinou, R. Latella, L. Moliner, J. Nuyts, L. Zhang, J. Barrio, J. Benlloch, and A. Gonzalez, "Metascintillators: New results for tof-pet applications," *IEEE Transactions on Radiation and Plasma Medical Sciences*, vol. 6, no. 5, pp. 510–516, 2022.

[84] R. Latella, A. J. Gonzalez, D. A. Bonifacio, M. Kovylina, A. Griol, J. M. Benlloch, P. Lecoq, and G. Konstantinou, "Exploiting cherenkov radiation with bgo-based metascintillators," *IEEE Transactions on Radiation and Plasma Medical Sciences*, 2023.

[85] F. Pagano, N. Kratochwil, L. Martinazzoli, M. Paganoni, M. Pizzichemi, and E. Auffray, "Modeling scintillation kinetics and coincidence time resolution in heterostructured scintillators," *Accepted for publication in IEEE Transaction on Nuclear Science*.

[86] "Eljen technology ej232 datasheet." https://eljentechnology.com/products/plastic-scintillators/ej-232-ej-232q, 2021.

[87] G. Konstantinou, R. Latella, L. Moliner, L. Zhang, J. Benlloch, A. Gonzalez, and P. Lecoq, "A proof-of-concept of cross-luminescent metascintillators: testing results on a bgo: Baf2 metapixel," *Physics in Medicine & Biology*, vol. 68, no. 2, p. 025018, 2023.

[88] E. G. Rogers, M. D. Birowosuto, F. Maddalena, C. Dujardin, F. Pagano, N. Kratochwil, E. Auffray, P. Krause, and G. Bizarri, "Two-dimensional perovskite functionalized fiber-type heterostructured scintillators," *Applied Physics Letters*, vol. 122, no. 8, 2023.

[89] F. Pagano, J. Král, K. Děcká, N. Kratochwil, M. Pizzichemi, E. Mihóková, V. Čuba, and E. Auffray, "Nanocrystalline lead halide perovskites for high-performance time-of-flight medical imaging detectors," *Under review in Advanced Materials Interfaces*.

[90] M. Orfano, F. Pagano, I. Mattei, F. Cova, V. Secchi, S. Bracco, E. Rogers, L. Barbieri, R. Lorenzi, G. Bizarri, *et al.*, "Fast emitting nanocomposites for high-resolution tof-pet imaging based on multicomponent scintillators," *arXiv preprint arXiv:2309.14968*, 2023.

[91] P. Mohr, N. Efthimiou, F. Pagano, N. Kratochwil, M. Pizzichemi, C. Tsoumpas, E. Auffray, and K. Ziemons, "Image reconstruction analysis for positron emission tomography with heterostructured scintillators," *IEEE Transactions on Radiation and Plasma Medical Sciences*, vol. 7, no. 1, pp. 41–51, 2022.

[92] N. Efthimiou, N. Kratochwil, S. Gundacker, A. Polesel, M. Salomoni, E. Auffray, and M. Pizzichemi, "TOF-PET image reconstruction with multiple timing kernels applied on Cherenkov radiation in BGO," *IEEE Transactions on Radiation and Plasma Medical Sciences*, 2020.

[93] J. Nuyts, M. Defrise, S. Gundacker, E. Roncali, and P. Lecoq, "The snr of positron emission data with gaussian and non-gaussian time-of-flight kernels, with application to prompt photon coincidence," *IEEE Transactions on Medical Imaging*, 2022.

[94] J. Barrio, N. Cucarella, M. Freire, E. Lamprou, S. Aguilar, C. Valladares, V. Ilisie, J. M. Benlloch, and A. J. Gonzalez, "Pet detector based on a semi-monolithic crystal with doi and tof capabilities," in *2020 IEEE Nuclear Science Symposium and Medical Imaging Conference (NSS/MIC)*, pp. 1–3, IEEE, 2020.

[95] G. Konstantinou, L. Zhang, D. Bonifacio, R. Latella, and J. Maria, "Semi-monolithic meta-scintillator simulation proof-of-concept, combining accurate doi and tof," 2023.

[96] K. Děcká, F. Pagano, I. Frank, N. Kratochwil, E. Mihóková, V. Čuba, and E. Auffray, "Timing performance of lead halide perovskite nanoscintillators embedded in polystyrene matrix," *accepted in Journal of Material Chemistry C*, 2022.

[97] F. Pagano, N. Kratochwil, I. Frank, S. Gundacker, M. Paganoni, M. Pizzichemi, M. Salomoni, and E. Auffray, "A new method to characterize low stopping power and ultra-fast scintillators using pulsed x-rays," *Frontiers in Physics*, p. 1085, 2022.

[98] G. Collaboration, S. Agostinelli, *et al.*, "Geant4–a simulation toolkit," *Nucl. Instrum. Meth. A*, vol. 506, no. 25, p. 0, 2003.

[99] M. Berger, J. Coursey, M. Zucker, and J. Chang, "Nist standard reference database 124 - stopping-power & range tables for electrons, protons, and helium ions," tech. rep., National Institute of Standards and Technology, Last update July 2017.

[100] F. Loignon-Houle, S. A. Charlebois, R. Fontaine, and R. Lecomte, "Monte carlo simulations of energy, time and spatial evolution of primary electrons generated by 511 kev photons in various scintillators," *Nuclear Instruments and Methods in Physics Research Section A: Accelerators, Spectrometers, Detectors and Associated Equipment*, vol. 1030, p. 166449, 2022.

[101] Y. Shao, "A new timing model for calculating the intrinsic timing resolution of a scintillator detector," *Physics in Medicine & Biology*, vol. 52, no. 4, p. 1103, 2007.

[102] L. Bollinger and G. E. Thomas, "Measurement of the time dependence of scintillation intensity by a delayed-coincidence method," *Review of Scientific Instruments*, vol. 32, no. 9, pp. 1044–1050, 1961.

[103] F. Anghinolfi, P. Jarron, A. Martemiyanov, E. Usenko, H. Wenninger, M. Williams, and A. Zichichi, "Nino: an ultra-fast and low-power front-end amplifier/discriminator asic designed for the multigap resistive plate chamber," *Nuclear Instruments and Methods in Physics Research Section A: Accelerators, Spectrometers, Detectors and Associated Equipment*, vol. 533, no. 1-2, pp. 183–187, 2004.

[104] "Id100 visible single-photon detector brochure." https://www.idquantique.com/quantum-sensing/products/id100/.

[105] L. Martinazzoli, N. Kratochwil, S. Gundacker, and E. Auffray, "Scintillation properties and timing performance of state-of-the-art gd3al2ga3o12 single crystals," *Nuclear Instruments and Methods in Physics Research Section A: Accelerators, Spectrometers, Detectors and Associated Equipment*, vol. 1000, p. 165231, 2021.

[106] M. Ishii, K. Harada, Y. Hirose, N. Senguttuvan, M. Kobayashi, I. Yamaga, H. Ueno, K. Miwa, F. Shiji, F. Yiting, *et al.*, "Development of bso (bi4si3o12) crystal for radiation detector," *Optical Materials*, vol. 19, no. 1, pp. 201–212, 2002.

[107] R. Cala, N. Kratochwil, L. Martinazzoli, M. Lucchini, S. Gundacker, E. Galenin, I. Gerasymov, O. Sidletskiy, M. Nikl, and E. Auffray, "Characterization of mixed bi4 (gexsi1- x) 3o12 for crystal calorimetry at future colliders," *Nuclear Instruments and Methods in Physics Research Section A: Accelerators, Spectrometers, Detectors and Associated Equipment*, vol. 1032, p. 166527, 2022.

[108] J. W. Cates, S. Gundacker, E. Auffray, P. Lecoq, and C. S. Levin, "Improved single photon time resolution for analog sipms with front end readout that reduces influence of electronic noise," *Physics in Medicine & Biology*, vol. 63, no. 18, p. 185022, 2018.

[109] "Broadcom nuv-hd silicon photomultiplier 3.72x3.72 active area." https://www.broadcom.com/products/optical-sensors/silicon-photomultiplier-sipm/afbr-s4n44c013.

[110] N. Kratochwil, S. Gundacker, P. Lecoq, and E. Auffray, "Pushing Cherenkov PET with BGO via coincidence time resolution classification and correction," *Physics in Medicine & Biology*, vol. 65, no. 11, p. 115004, 2020.

[111] F. Loignon-Houle, S. Gundacker, M. Toussaint, F. C. Lemyre, E. Auffray, R. Fontaine, S. A. Charlebois, P. Lecoq, and R. Lecomte, "Doi estimation through signal arrival time distribution: a theoretical description including proof of concept measurements," *Physics in Medicine & Biology*, vol. 66, no. 9, p. 095015, 2021.

[112] S. Gundacker, E. Auffray, B. Frisch, P. Jarron, A. Knapitsch, T. Meyer, M. Pizzichemi, and P. Lecoq, "Time of flight positron emission tomography towards 100ps resolution with l (y) so: an experimental and theoretical analysis," *Journal of Instrumentation*, vol. 8, no. 07, p. P07014, 2013.

[113] J. W. Cates, R. Vinke, and C. S. Levin, "Analytical calculation of the lower bound on timing resolution for pet scintillation detectors comprising high-aspect-ratio crystal elements," *Physics in Medicine & Biology*, vol. 60, no. 13, p. 5141, 2015.

[114] S. Seifert and D. R. Schaart, "Improving the time resolution of tof-pet detectors by double-sided readout," *IEEE Transactions on Nuclear Science*, vol. 62, no. 1, pp. 3–11, 2014.

[115] K. Weindel, V. Nadig, K. Herweg, V. Schulz, and S. Gundacker, "A time-based double-sided readout concept of 100 mm lyso: Ce, ca fibres for future axial tof-pet," *EJNMMI physics*, vol. 10, no. 1, p. 43, 2023.

[116] M. Sun, C. Zhang, and B. Zhao, "Coincidence time resolution measurements for dual-ended readout pet detectors," *Journal of Instrumentation*, vol. 18, no. 07, p. P07003, 2023.

[117] "Crystal photonics, inc.." http://www.jccsoc.com/EN/.

[118] "Multiwave metacrystal." https://metacrystal.ch.

[119] S. Surti, A. Kuhn, M. E. Werner, A. E. Perkins, J. Kolthammer, and J. S. Karp, "Performance of philips gemini tf PET/CT scanner with special consideration for its time-of-flight imaging capabilities," *Journal of Nuclear Medicine*, vol. 48, no. 3, pp. 471–480, 2007.

[120] "Broadcom nuv-hd silicon photomultiplier 3.14x3.14 active area." https://www.broadcom.com/products/optical-sensors/silicon-photomultiplier-sipm/afbr-s4n33c013.

[121] C. Piemonte, F. Acerbi, A. Ferri, A. Gola, G. Paternoster, V. Regazzoni, G. Zappala, and N. Zorzi, "Performance of nuv-hd silicon photomultiplier technology," *IEEE Transactions on Electron Devices*, vol. 63, no. 3, pp. 1111–1116, 2016.

[122] "Broadcom nuv-hd silicon photomultiplier 3.14x3.14 active area." https://www.broadcom.com/products/optical-sensors/silicon-photomultiplier-sipm/high-performance-sipm-nuv-mt/afbr-s4n44p014m.

[123] M. Pizzichemi, G. Stringhini, T. Niknejad, Z. Liu, P. Lecoq, S. Tavernier, J. Varela, M. Paganoni, and E. Auffray, "A new method for depth of interaction determination in pet detectors," *Physics in Medicine & Biology*, vol. 61, no. 12, p. 4679, 2016.

[124] S. Salvador, J. Wurtz, and D. Brasse, "Optimizing pet doi resolution with crystal coating and length," *IEEE Transactions on Nuclear Science*, vol. 57, no. 5, pp. 2468–2474, 2010.

[125] J. Trummer, E. Auffray, and P. Lecoq, "Depth of interaction resolution of luap and lyso crystals," *Nuclear Instruments and Methods in Physics Research Section A: Accelerators, Spectrometers, Detectors and Associated Equipment*, vol. 599, no. 2-3, pp. 264–269, 2009.

[126] M. Pizzichemi, A. Polesel, G. Stringhini, S. Gundacker, P. Lecoq, S. Tavernier, M. Paganoni, and E. Auffray, "On light sharing tof-pet modules with depth of interaction and 157 ps fwhm coincidence time resolution," *Physics in Medicine & Biology*, vol. 64, no. 15, p. 155008, 2019.

[127] N. Kratochwil, E. Auffray, and S. Gundacker, "Exploring Cherenkov emission of BGO for TOF-PET," *IEEE Transactions on Radiation and PlasmaMedical Sciences (under consideration)*, 2020.

[128] A. Hospodková, M. Nikl, O. Pacherová, J. Oswald, P. Brůža, D. Pánek, B. Foltynski, E. Hulicius, A. Beitlerová, and M. Heuken, "InGaN/GaN multiple quantum well for fast scintillation application: radioluminescence and photoluminescence study," *Nanotechnology*, vol. 25, no. 45, p. 455501, 2014.

[129] S. Gundacker, R. Turtos, E. Auffray, and P. Lecoq, "Precise rise and decay time measurements of inorganic scintillators by means of x-ray and 511 kev excitation," *Nuclear Instruments and Methods in Physics Research Section A: Accelerators, Spectrometers, Detectors and Associated Equipment*, vol. 891, pp. 42–52, 2018.

[130] Y. Wang, S. Xu, D. Zhao, J. Zhu, H. Yang, X. Shan, and D. Yu, "Non-exponential photoluminescence decay dynamics of localized carriers in disordered ingan/gan quantum wells: the role of localization length," *Optics Express*, vol. 14, no. 26, pp. 13151–13157, 2006.

[131] F. Zhang *et al.*, "Simulation of x-ray shielding effect of different materials based on mcnp5," *Open Access Library Journal*, vol. 7, no. 09, p. 1, 2020.

[132] M. M. Nasseri, "Determination of tungsten target parameters for transmission x-ray tube: A simulation study using geant4," *Nuclear Engineering and Technology*, vol. 48, no. 3, pp. 795–798, 2016.

[133] S. Vinogradov, "Analytical models of probability distribution and excess noise factor of solid state photomultiplier signals with crosstalk," *Nuclear Instruments and Methods in Physics Research Section A: Accelerators, Spectrometers, Detectors and Associated Equipment*, vol. 695, pp. 247–251, 2012.

[134] Becker&Hickl, "Hpm 100-07 data-sheet," 2022.

[135] W. Moses, G. Bizarri, R. T. Williams, S. Payne, A. Vasil'Ev, J. Singh, Q. Li, J. Grim, and W.-S. Choong, "The origins of scintillator non-proportionality," *IEEE Transactions on Nuclear Science*, vol. 59, no. 5, pp. 2038–2044, 2012.

[136] C. Wanarak, W. Chewpraditkul, and A. Phunpueok, "Light yield non-proportionality and energy resolution of lu1. 95y0. 05sio5: Ce and lu2sio5: Ce scintillation crystals," *Procedia Engineering*, vol. 32, pp. 765–771, 2012.

[137] J. Pichette, J. B. Domínguez, and Y. Bérubé-Lauzière, "Time-domain geometrical localization of point-like fluorescence inclusions in turbid media with early photon arrival times," *Applied Optics*, vol. 52, no. 24, pp. 5985–5999, 2013.

[138] Y. Bérubé-Lauzière, M. Crotti, S. Boucher, S. Ettehadi, J. Pichette, and I. Rech, "Prospects on time-domain diffuse optical tomography based on time-correlated single photon counting for small animal imaging," *Journal of Spectroscopy*, vol. 2016, 2016.

[139] J. Rossignol, R. M. Turtos, S. Gundacker, D. Gaudreault, E. Auffray, P. Lecoq, Y. Bérubé-Lauzière, and R. Fontaine, "Time-of-flight computed tomography-proof of principle," *Physics in Medicine & Biology*, vol. 65, no. 8, p. 085013, 2020.

[140] J. Rossignol, P. Marcoux, G. Bélanger, F. Gagnon, P. Dufour, A. Corbeil Therrien, Y. Bérubé-Lauzière, and R. Fontaine, "Toward a first prototype time-of-flight ct scanner," 2022. Workshop on fast time for medical imaging.

[141] L. Protesescu, S. Yakunin, M. I. Bodnarchuk, F. Krieg, R. Caputo, C. H. Hendon, R. X. Yang, A. Walsh, and M. V. Kovalenko, "Nanocrystals of Cesium Lead Halide Perovskites (CsPbX 3 , X = Cl, Br, and I): Novel Optoelectronic Materials Showing Bright Emission with Wide Color Gamut," *Nano Letters*, vol. 15, pp. 3692–3696, jun 2015.

[142] Y. Wang, J. Ren, X. Zhou, and G. Zhang, "Stability improvements of metal halide perovskite nanocrystals and their optoelectrical applications," *Materials Chemistry Frontiers*, 2023.

[143] M. Gandini, I. Villa, M. Beretta, C. Gotti, M. Imran, F. Carulli, E. Fantuzzi, M. Sassi, M. Zaffalon, C. Brofferio, L. Manna, L. Beverina, A. Vedda, M. Fasoli, L. Gironi, and S. Brovelli, "Efficient, fast and reabsorption-free perovskite nanocrystal-based sensitized plastic scintillators," *Nature Nanotechnology*, vol. 15, no. 6, pp. 462–468, 2020.

[144] J. Nie, C. Li, S. Zhou, J. Huang, X. Ouyang, and Q. Xu, "High Photoluminescence Quantum Yield Perovskite/Polymer Nanocomposites for High Contrast X-ray Imaging," *ACS Applied Materials & Interfaces*, vol. 13, pp. 54348–54353, nov 2021.

[145] W. Ma, T. Jiang, Z. Yang, H. Zhang, Y. Su, Z. Chen, X. Chen, Y. Ma, W. Zhu, X. Yu, H. Zhu, J. Qiu, X. Liu, X. Xu, and Y. M. Yang, "Highly Resolved and Robust Dynamic X-Ray Imaging Using Perovskite Glass-Ceramic Scintillator with Reduced Light Scattering," *Advanced Science*, vol. 8, p. 2003728, aug 2021.

[146] M. D. Tessier, C. Javaux, I. Maksimovic, V. Loriette, and B. Dubertret, "Spectroscopy of single CdSe nanoplatelets," *ACS Nano*, vol. 6, no. 8, pp. 6751–6758, 2012.

[147] L. Zhang, W. Liang, L. Xu, M. Zhu, X. Wang, J. Su, L. Li, N. Liu, Z. Zhang, and Y. Gao, "Room-temperature quaternary alkylammonium passivation toward morphology-controllable cspbbr3 nanocrystals with excellent luminescence and stability for white leds," *Chemical Engineering Journal*, vol. 417, p. 129349, 2021.

[148] M. Imran, P. Ijaz, L. Goldoni, D. Maggioni, U. Petralanda, M. Prato, G. Almeida, I. Infante, and L. Manna, "Simultaneous cationic and anionic ligand exchange for colloidally stable cspbbr3 nanocrystals," *ACS Energy Letters*, vol. 4, no. 4, pp. 819–824, 2019.

[149] C. Lu, M. Wright, X. Ma, H. Li, D. Itanze, J. A. Carter, C. Hewitt, G. Donati, D. Carroll, P. Lundin, and S. Geyer, "Cs Oleate Precursor Preparation for Lead Halide Perovskite Nanocrystal Synthesis: The Influence of Excess Oleic Acid on Achieving Solubility, Conversion, and Reproducibility.," *Chemistry of Materials*, vol. 31, 12 2018.

[150] K. Děcká, J. Král, F. Hájek, P. Průša, V. Babin, E. Mihóková, and V. Čuba, "Scintillation Response Enhancement in Nanocrystalline Lead Halide Perovskite Thin Films on Scintillating Wafers," *Nanomaterials*, vol. 12, p. 14, dec 2021.

[151] W. W. Moses and S. Derenzo, "Prospects for time-of-flight pet using lso scintillator," *IEEE Transactions on Nuclear Science*, vol. 46, no. 3, pp. 474–478, 1999.

[152] M. S. Lee, J. W. Cates, A. Gonzalez-Montoro, and C. S. Levin, "High-resolution time-of-flight pet detector with 100 ps coincidence time resolution using a side-coupled phoswich configuration," *Physics in Medicine & Biology*, vol. 66, no. 12, p. 125007, 2021.

[153] M. Berger, J. Hubbell, S. Seltzer, J. Coursey, and D. Zucker, "Xcom: Photon cross section database (version 1.5)," 2010.

[154] V. Nadig, M. Yusopova, H. Radermacher, D. Schug, B. Weissler, V. Schulz, and S. Gundacker, "A comprehensive study on the timing limits of the tofpet2 asic and on approaches for improvements," *IEEE Transactions on Radiation and Plasma Medical Sciences*, vol. 6, no. 8, pp. 893–903, 2022.